MODELLING SOLAR IRRADIANCE ON A SLOPE UNDER A LEAFLESS DECIDUOUS FOREST

James D. Rowland
Department of Geography
McGill University, Montréal
August 1989

A Thesis submitted to the Faculty of Graduate Studies and Research in partial fulfillment of the requirements for the degree of Master of Science

ABSTRACT

This thesis investigates variations in solar irradiance incident upon sloping surfaces under deciduous forest in winter. A model is presented for prediction of solar irradiance at the surface which accounts for slope inclination and orientation, surrounding topography, isotropic absorption of solar radiation by the crown space, and shadows cast by the stem space.

Field data from two sites of different slope and aspect attest to the validity of the model; errors, based on 20-minute averages of instantaneous values, are 15.5% (RMSE) and -1.9% (MBE). Error is partially due to reliance upon global radiation measurements above canopy at a different site (partially cloudy conditions) and sampling error (sunny sky conditions). The variability of solar irradiance at the surface, and in the error of predicted values, is found to vary with sky condition, solar zenith and incidence angles, and slope orientation. However, integration to hourly and/or daily time periods improves model performance significantly.

RESUME

La présente thèse examine les variations du rayonnement solaire reçu sur des surfaces en pente sous une forêt à feuillage caduc en hiver. On y présente un modèle qui a pour but de prédire la quantité de rayonnement solaire reçu au sol, et qui tient compte de l'inclinaison et l'orientation de la surface, de la topographie environnante, de l'absorption isotrope du rayonnement solaire par les couronnes d'arbres, et des ombrages projetés par les troncs d'arbres.

Les valeurs du rayonnement pour deux sites de pente et d'exposition différentes attestent de la validité du modèle; les erreurs, calculées à partir de moyennes d'observations instantanées sur vingt minutes, sont 15.5% (erreur quadratique moyenne) et -1.9% (erreur systématique moyenne). Les erreurs sont en partie redevables (temps partiellement nuageux) à l'utilisation de valeurs de rayonnement global mesurées au-dessus de la forêt à un site unique et (temps ensoleillé) à l'erreur d'échantillonnage. Il est démontré que la variabilité de rayonnement solaire au sol, ainsi que la variabilité de l'erreur dans les valeurs estimées, varie selon l'état du ciel, la distance zenithale, l'angle d'incidence du rayonnement et l'orientation de la pente. Par contre, l'intégration aux périodes de temps plus longues, i.e., d'heure en heure et/ou diurnes, améliore le rendement du modèle d'une manière significative.

ACKNOWLEDGMENTS

I would like to thank my supervisor, Dr. R.D. Moore, Department of Geography, Simon Fraser University, for his guidance and assistance throughout the field work session and the writing of the thesis. I would also like to acknowledge the assistance and advice (and provision for field equipment) given by Dr. J.E. Lewis, and useful comments provided by Dr. B.J. Garnier, both of McGill University, Department of Geography.

This project was supported in part by the Natural Sciences and Engineering Research Council of Canada. Thanks are due to the Université de Montréal Biological Research Station at St. Hippolyte, Québec, for the use of the tower and field sites, as well as to Dr. T.R. Oke (Department of Geography, University of British Columbia) and Dr. M. Lechowicz (Department of Biology, McGill University) for the use of field instruments.

Finally, I wish to thank C.A. Nadeau for assistance in preparation of field instrumentation, as well as for many enlightening discussions. Also, thanks to M. Paquet for encouragement to undertake such a project, and to D.T. House and L.A. Cabane for encouragement along the way.

TABLE OF CONTENTS

LIST OF TABLES

LIST OF FIGURES

LIST OF SYMBOLS

a	slope azimuth, east zero, north positive (rad)
A	slope azimuth, north zero, east positive (rad)
A_s	area of shadow cast by a single stem or cylinder (m^2)
B	basal area fraction
B_m	bound on the difference between the sample mean and the population mean, for a given level of significance
CV	coefficient of variation
d_n	day number of the year, from 1 to 365
dG	fraction of area shaded by a stem or cylinder
dS	additional fraction of area shaded by adding a stem or cylinder
D	arithmetic mean diameter (stem or cylinder) (m)
D_H	diffuse radiation above canopy from entire hemisphere (Wm^{-2})
D_q	quadratic mean diameter (stem or cylinder) (m)
D_s	diffuse radiation above canopy, sloping surface (Wm^{-2})
F	ratio of direct to global radiation above canopy
F_1	diffuse radiation from the portion of hemisphere blocked by a shadow band (Wm^{-2})
G	fraction of total area shaded
h	tree or cylinder height (m)
h_c	crown space thickness, in direction normal to the horizontal (m)
h_s	stem space thickness, or height of cylinder (m)
H	hour angle, solar noon zero, west positive (rad)
H_s	sensible heat flux to a snowpack (Wm^{-2})
i	solar incidence angle, the angle between the normal to a slope and the solar ray (rad)
I_H	direct solar irradiance incident upon a horizontal surface (Wm^{-2})
I_m	direct solar irradiance incident upon a surface normal to the sun's rays (Wm^{-2})
I_s	direct solar irradiance incident upon a sloping surface (Wm^{-2})
k	extinction or absorption coefficient (m^{-1})
K_b	correction factor applied to diffuse radiation data measured using a shadow band
K_D	global or incoming shortwave radiation (Wm^{-2})
K_s	reduction factor due to slope and topographical obstacles for diffuse radiation
K_U	reflected or outgoing shortwave radiation (Wm^{-2})
K_{ao}	incoming global radiation above canopy (Wm^{-2})
K_{bo}	incoming global radiation below canopy (Wm^{-2})
l_c	path length through the crown space (m)
L_D	incoming longwave radiation (Wm^{-2})
LE	latent heat flux to a snowpack (Wm^{-2})
L_f	latent heat of fusion (Jkg^{-1})
L_U	outgoing longwave radiation (Wm^{-2})

M rate of snowmelt (ms^{-1})
MBE Mean bias error
n stand density, number of stems or cylinders over 1.25 cm diameter (ha^{-1})
n_u number of stems or cylinders per unit area
N number of observations
O observed or measured value
P predicted or computed value
P_s heat flux to a snowpack from liquid precipitation (Wm^{-2})
Q_m total heat exchange across snowpack surface (Wm^{-2})
Q^* net radiant flux to a snowpack (Wm^{-2})
r_w density of water (kgm^{-3})
RMSE root mean square error, based upon predicted and observed values
RMSE(mod) model error, based upon predicted and true values
RMSE(obs) observed error, based upon observed and true values
S unit vector expressing height and position of the sun
SD sample standard deviation
SE standard error of the mean
S_H actual fraction of area shaded
t_c transmissivity of the crown space to beam radiation
t_d transmissivity of the canopy (crown and stem space) to diffuse radiation
t_o hour angle of the sun at sunset (rad)
t_s transmissivity of the stem space to beam radiation
$t(\alpha_t/2)$ t-statistic at the α_t level of significance
T total transmissivity of the canopy to direct and diffuse radiation
U unit area (ha = 10 000 m^2)
w width of shadow band (m)
x path length through an absorbing (translucent) medium (m)
X unit vector normal to (and pointing away from) a slope
z solar azimuth, south zero, east positive (rad)
z_1 solar azimuth, east zero, north positive (rad)
Zx zenith angle of the vector X, or slope inclination (rad)
α crown space absorption coefficient (m^{-1})
α_s shortwave surface albedo
α_t level of significance (statistical)
β slope degree or inclination (rad)
τ radius of shadow band (m)
Γ day angle (rad)
δ solar declination (rad)
θ solar zenith angle (rad)
$\theta(z)$ maximum solar zenith angle as a function of solar azimuth angle (rad)
σ slope azimuth, south zero, east positive (rad)
ϕ site latitude (rad)
Ω hour angle, solar noon zero, east positive (rad)
$\cap$ symbol denoting the angle between two vectors

Symbols used only in Appendix A

C	cos(i), where i is solar incidence angle
L	vector on a plane which corresponds to the length of a shadow between top and bottom of the center of a stem
p	vector representing all points on a plane
p*	point on the plane representing the slope which satisfies equation A5, Appendix A
p*	vector from the origin to the point p*
p′,p″	vectors from the origin to the points where the two edges of the shadow meet the base of the stem
r	distance from origin to point in spherical coordinate system
v	length of the vector which connects the center of the top of a stem to the point p* (m)
$\mathbf{w}_s$	vector spanning the width of stem shadow

CHAPTER 1

INTRODUCTION

1.1. SNOWMELT AND SOLAR RADIATION

The seasonal melting of snowpacks is a major hydrological event, and snowmelt prediction models are useful with respect to short-term events such as flood forecasting and/or reservoir operations, and long-term consequences such as groundwater recharge and soil moisture regimes. More recently, short-term snowmelt estimates have become important for understanding the role of the snowpack in the chemistry of watersheds, in particular the hydrochemical processes involved in acid loading to surface waters (e.g., Christopherson et al., 1984; Roberge et al., 1985).

Net radiation is the major input to the surface energy budget in snow-covered, forested environments and, therefore, an important contribution to the energy available for snowmelt. In such environments both latent and sensible heat fluxes are suppressed due to low wind speeds and the typically stable atmosphere found over snowpacks (Price, 1988). Determination of net radiation, however, requires accurate measurements or estimates of solar irradiance incident upon the surface.

Solar irradiance incident upon a surface varies greatly, both spatially and temporally, depending upon climatic, topographic and vegetative conditions, particularly in mountainous or hilly regions at mid- and high-latitudes. Slope inclination and orientation will enhance the variation in solar radiation income between slope facets, whereas the variability within such facets is due to the vegetative cover (e.g., shadows of individual trees). The surrounding topography also affects the solar irradiance incident upon a given slope through horizon effects (obstacles) and radiation reflected from surrounding terrain. Since incoming solar radiation is both spatially and temporally the most variable of the radiative components of the surface energy balance, both the topographic and vegetative characteristics of a site must be considered in order to obtain representative values for instantaneous or short time interval estimates.

Deciduous and mixed deciduous/coniferous forests cover a significant proportion of North America and, at mid-latitudes, are generally snow-covered at the surface for some winter period. For a leafless deciduous forest, the transmission of solar radiation has an important effect upon the energy available for either snowmelt or early spring vegetative growth (Federer, 1971). Understanding the solar radiation regime of such forests on sloping terrain could be of assistance in elaborating upon the microclimates present within topographically diverse areas (e.g., watersheds), and is necessary for a realistic approach to the study of snowmelt in hardwood forests (Federer, 1971).

Estimates of solar irradiance incident upon slopes could be used in a simple melt model with empirical coefficients (adjusted to melt calculated from snow surveys) to predict snowmelt, or used in conjunction with a digital terrain model to provide estimates of the spatial variations of melt. Coupling of solar irradiance estimates with other radiative exchanges would allow determination of net radiation; further application in an energy balance would allow prediction of snowmelt rates for entire catchment basins.

1.2. OBJECTIVES OF THE CURRENT RESEARCH

A model of radiative exchange in leafless deciduous canopies which accounts for variations in slope and aspect could be useful for predicting snowmelt in watersheds, at least for research applications. An important component is the description of the transmission, absorption and reflection of solar radiation. The goal of this research, therefore, is to develop a model for predicting the solar irradiance incident upon a slope of any inclination and orientation under a leafless, deciduous forest, and to test the model against field data. Although model testing focuses on solar irradiance at the forest floor, this extended model (based on Federer, 1971) can also be used to predict the absorption of solar radiation by the canopy. A secondary goal is to quantify the spatial and temporal variability of solar irradiance within a given site. From this an indication can be obtained of the number of radiometers which might be required at experimental test sites for different time-averaging intervals (and the necessary time-averaging period required) in order to limit error to a predetermined level. Figure 1.1 shows briefly the steps to be followed for the model verification process. The right-hand column indicates the model which is to be applied to the field data (left-hand column), resulting in intermediate data (middle column), which subsequently become input data for the following process.

1.3. PRESENTATION FORMAT

The present thesis discusses general perspectives on snowmelt estimation, and snowmelt processes and prediction under deciduous forest. Radiative exchange in forest canopies is reviewed in terms of topographical and forest canopy considerations, in particular leafless deciduous canopies.

In Chapter 3, Federer's model (1971) for describing the solar radiation regime within a leafless deciduous forest is presented in detail, as the basis for the present research. The extensions and adjustments required to allow for slopes of any inclination and orientation are then developed. Study sites, data collection methods, and procedures for instrument

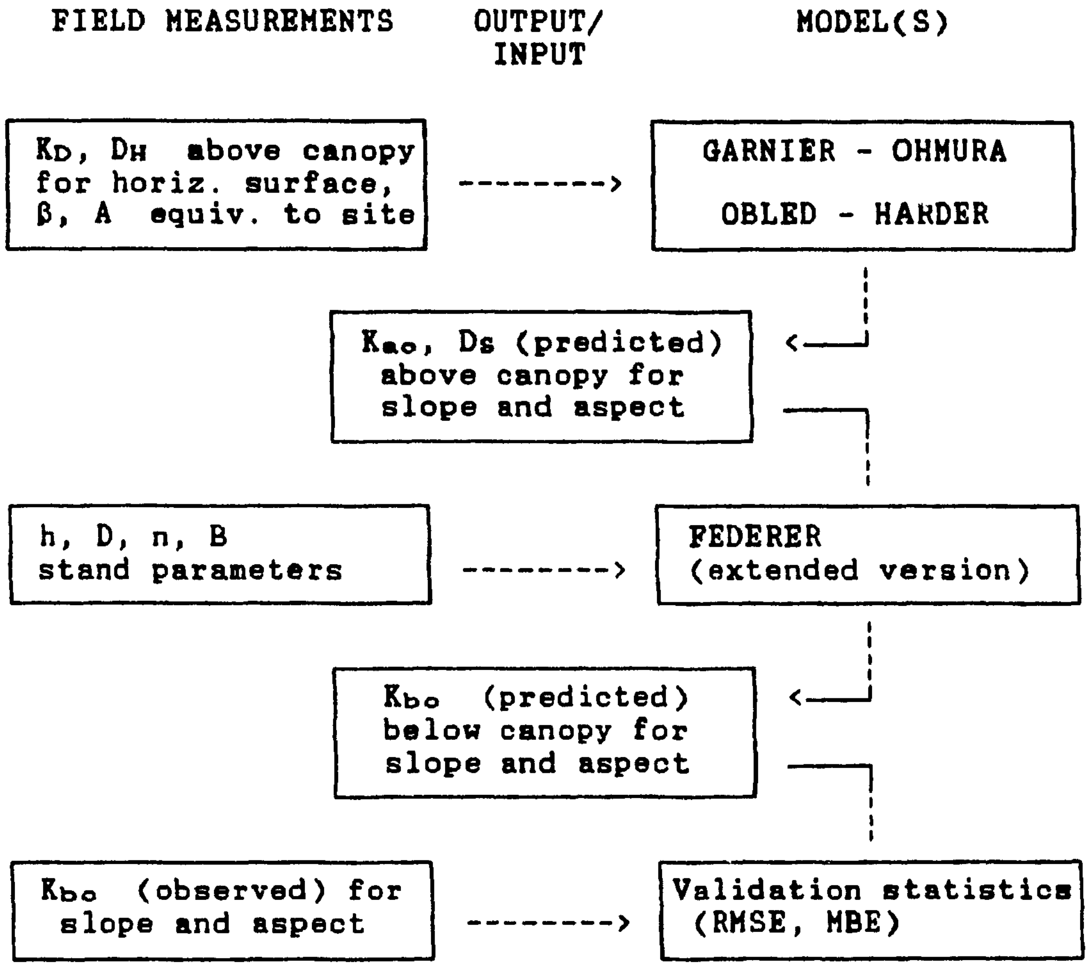

K_D global radiation on horizontal surface (Wm^{-2})
D_H diffuse radiation on horizontal surface (Wm^{-2})
β slope degree (rad)
A slope azimuth (rad)
K_{ao} global radiation above canopy on sloping surface (Wm^{-2})
D_S diffuse radiation above canopy on sloping surface (Wm^{-2})
h tree height (m)
D mean tree diameter (m)
n stand density (ha^{-1})
B basal area fraction
K_{bo} global radiation below canopy on sloping surface (Wm^{-2})
RMSE root mean square error
MBE mean bias error

FIGURE 1.1. Model verification process. The right-hand column indicates the model to be applied to measured field data (left-hand column), resulting in intermediate data (middle column), which subsequently become input for the following process.

calibration and shadow band correction are described in Chapter 4. A short discussion on the spatial and temporal variability of the solar irradiance data, as it pertains to precision of the observed data, is also included here.

Model calibration and verification are presented in Chapter 5. Validation statistics (root mean square and mean bias errors) are generated from predicted and observed values, using an extensive data set of values of solar irradiance incident upon two slopes of different inclination and orientation under a leafless deciduous forest. Error analysis results are discussed with respect to data sets stratified by sky condition, solar zenith and incidence angles, and the ratio of direct to global solar irradiance. Results concerning both the sensitivity of the adapted model to stand and site variables, and the improvement in model performance with integration from 20-minute averaging periods to hourly and daily time periods, are also discussed. Finally, Chapter 6 presents some problems inherent in the model, summarizes the main findings of the study, and suggests dirctions for future work in the development and verification of physically-based models which may aid in the understanding of the solar radiation regime at the forest floor, under leafless deciduous canopies.

CHAPTER 2

LITERATURE REVIEW

2.1. GENERAL PERSPECTIVES ON SNOWMELT ESTIMATION

The most direct methods of determining snowmelt utilize a water balance approach to relate melt volumes to changes in snowpack storage or to outflow from a control volume. Fitzgibbon and Dunne (1980) used snow surveys to calculate change in snowpack storage, while Anderson (1976) and U.S.A.C.E. (1956) measured lysimeter outflow, and Price and Dunne (1976) measured hillslope runoff for use in melt calculations. However, water balance methods are labor- and/or instrument-intensive, and many studies have been undertaken to relate snowmelt rates to energy flux considerations.

For a melting snowpack melt is driven primarily by the energy exchange across its upper surface, since these exchanges are usually much greater than the heat flux between the soil and the snowpack (Male and Granger, 1981). Most methods for predicting snowmelt attempt either to derive empirical relationships between melt rates and some index of energy exchange, or to evaluate explicitly the energy exchanges. The first method attempts to derive empirical relationships between snowmelt (determined by a water balance method) and one or more of the meteorological variables such as air temperature and net or solar radiation (e.g., Zuzel and Cox, 1975). The second method calculates melt as:

$$M = Q_m/r_w L_f \tag{2.1}$$

where M is the melt rate (ms^{-1})

Q_m is total heat exchange across the snowpack surface (Wm^{-2})

r_w is the density of water (kgm^{-3})

L_f is the latent heat of fusion (Jkg^{-1}).

The total heat exchange can be calculated from measurements of net radiation, air temperature, humidity and wind speed (Anderson, 1976; Price and Dunne, 1976), and is given by:

$$Q_m = Q^* + LE + H_s + P_s \qquad (2.2)$$

where Q^* is the net radiant flux to the snowpack (Wm^{-2})
LE is the latent heat flux to the snowpack (Wm^{-2})
H_s is the sensible heat flux to the snowpack (Wm^{-2})
P_s is the heat flux to the snowpack from liquid precipitation (Wm^{-2}).

The meteorological variables driving snow surface energy exchange, and hence melt, vary with topographic factors such as slope inclination and orientation, as well as with vegetation characteristics (Male and Granger, 1981). Hendrick et al. (1971) showed through simulation that streamflow response to snowmelt depends greatly on the degree of topographic and vegetative diversity in a watershed, and Lawrence et al. (1988) showed empirically that the temporal variations in streamwater chemistry are related to the spatial and temporal variations in hydrologic processes. Hence, realistic models for snowmelt prediction should be capable of describing the spatial variations in melt rates, in order to help understand variations in both quantity and quality of streamwater. Models which account for the spatial variations in melt should be useful for extrapolating water-balance derived melt estimates made at one or more sites (e.g., a lysimeter on a particular slope facet) to the rest of the watershed, especially when used in conjunction with digital terrain models, which appear to be increasingly used in watershed modelling (e.g., Burch et al., 1987).

2.2. SNOWMELT PROCESSES AND PREDICTION UNDER DECIDUOUS FOREST

Net radiation is the major energy source driving snowmelt in snow-covered forested environments, both deciduous and coniferous (e.g. Hendrie and Price, 1979; Hendrick et al., 1971; Price, 1988). Uniformly low windspeeds in forests and highly stable atmospheric conditions over melting snowpacks result in highly damped turbulent exchanges, such that ignoring the turbulent exchanges of sensible and latent heat in calculating melt would result in errors of at most ten percent (Price, 1988). Price showed that a simple linear model relating net radiation at the snow surface to air temperature and above-canopy global radiation explained 75% of the variance of net radiation. This model performed much better than a model based only on air temperature, the most commonly used approach in operational snowmelt prediction. A simple regression of net radiation on above-canopy global radiation was also deemed not appropriate in a deciduous forest during snowmelt (Price, 1988). Price's work concentrated on measurements at one site, and extrapolating such measurements to sites of different slope inclination and/or orientation would require a better understanding of the effects of topography on radiative exchange at the surface and within leafless deciduous canopies. The next sections review these exchanges and models which have been developed to describe them.

2.3. RADIATIVE EXCHANGE IN FOREST CANOPIES

Net radiation (Q^*) in vegetated environments is difficult to estimate accurately or measure representatively (Impens et al., 1970; Nadeau and Granberg, 1986; Petzold, 1981). Variations in net radiation and, thus, energy available for snowmelt due to topographical and vegetative diversity, combined with the sparseness of routine measurements, produce a need for operational models of net radiation at the surface. The necessary components for modelling the radiative exchanges at the earth's surface are given by:

$$
\begin{aligned}
Q^* &= K_D - K_U + L_D - L_U \\
&= K_D(1 - \alpha_s) + L_D - L_U \qquad (2.3)
\end{aligned}
$$

where K_D is the global or incoming shortwave radiation (Wm^{-2})
K_U is the reflected or outgoing shortwave radiation (Wm^{-2})
L_D is the incoming longwave radiation (Wm^{-2})
L_U is the outgoing longwave radiation (Wm^{-2})
α_s is the shortwave surface reflectivity.

Modelling approaches for determining net radiation at the surface may either (1) model the short- and longwave exchanges separately, or (2) deal implicitly with the longwave exchanges through derivation of empirical relationships between global and net radiation.

Incoming solar radiation, in a forested environment, is the major input to the surface radiation budget (Price, 1988; Reifsnyder and Lull, 1966). Furthermore, in such an environment, incoming shortwave radiation is the most spatially and temporally variable of the radiative components due to interference of direct beam radiation by the forest canopy, resulting in quickly changing sunflecks at the forest floor (Hendrie and Price, 1979; Pech, 1986; Takenaka, 1987). Direct beam radiation is also the component of the surface radiation budget most affected by topography. Consequently, global solar radiation must be accurately modelled in order to obtain instantaneous or short term estimates of solar irradiance at the surface, considering both the topographic and vegetative characteristics of a site as independent variables.

2.3.1. TOPOGRAPHICAL CONSIDERATIONS

Potential solar irradiance incident upon a slope (assuming no vegetation cover) is dependent upon earth-sun geometry, solar beam attenuation due to the atmosphere, and ratio of direct to diffuse solar radiation. Variables related to earth-sun geometry include solar declination, solar zenith and azimuth angles, site latitude, slope inclination and orientation, and local topography. Direct solar radiation on a slope may be completely blocked by either the slope itself or topographical obstacles on the horizon. Diffuse radiation on a slope is affected by topographical variations through decreased radiation due to the slope, decreased sky hemisphere due to surrounding topography, and/or reflected radiation from surrounding surfaces. Estimation of the solar irradiance incident upon a slope requires a "geometrically based transformation of the direct (beam) radiation and an integration of the diffuse radiance... over the field of view of the surface" (Hay, 1986, p. 17).

Kondrat'yev (1965) presented formulae for the direct and diffuse components of solar radiation incident upon a slope, dependent upon surface geometry and solar position for calculation of the solar incidence angle. Considering diffuse radiation isotropic, an equation was developed which eliminates the portion of the hemisphere blocked by the slope. Garnier and Ohmura (1968, 1970) and Ohmura (1977) also developed formulae which determine shortwave radiation incident upon surfaces of any slope and aspect from data recorded with respect to a horizontal surface. These formulae (Garnier and Ohmura, 1970) are incorporated into the present model and are further detailed in Chapter 3, Section 3.2.2.

A great variety of mathematical models has since been developed to predict solar irradiance incident upon inclined surfaces or mountain slopes (e.g., Flint and Childs, 1987; Peterson et al., 1985; Swift, 1976). Some of these have considered theoretically based techniques, incorporating atmospheric attenuation due to scattering and absorption by aerosols, water vapor, air molecules and ozone; this procedure becomes necessary if representative radiation observations are not available. Other models have used empirically based methods to divide global radiation into direct and diffuse components, generally accomplished by relating the ratio of direct to global radiation to the ratio of global to extra-terrestrial radiation (Hay and Davies, 1980). Hay and McKay (1985) and Skartveit and Olseth (1986), among others, have reviewed and/or assessed the performance of some of these models. Most of these studies, however, have dealt with daily or monthly averages and none of them has dealt realistically with forested environments. In fact, often the point of interest in studying solar radiation incident upon inclined surfaces is to maximize solar irradiance upon a surface in order to increase solar energy cell efficiency.

2.3.2. FOREST CANOPY CONSIDERATIONS

The radiation regime of sloping forested environments is a function of the previously mentioned slope factors, but is further complicated by its dependence upon the canopy architecture and the optical properties of the vegetation (Baldocchi, Matt et al., 1984). The presence of a forest canopy, whether coniferous or deciduous, acts as an absorber of shortwave radiation, reducing [illegible] radiation at the forest floor. Solar radiation incident on a forest canopy may be reflected upwards, absorbed by the canopy, or transmitted through the canopy either directly or by forward scattering. The highly reflective properties of a snow cover result in a significant proportion of the solar irradiance incident upon the surface being reflected. The reflected portion, from 30 to 95 percent depending upon solar elevation, age of snow, water content and accumulation of organic matter (McKay, 1970), is again liable to either absorption, reflection or transmission by the canopy. Solar radiation absorbed by the canopy is eventually re-radiated as longwave radiation, both upward toward space and downward toward the surface. Thus, at the snow surface under a forest canopy, the effect of the incident radiation is "governed largely by the interactions of the reflective and radiative properties of snow with the forest foliage overhead" (Reifsnyder and Lull, 1966, p. 84). Furthermore, reflectivity, transmissivity and absorption will differ for the direct and diffuse components of solar radiation due to both the complex and variable three-dimensional geometry of the canopy, and cloud cover (Male and Granger, 1981; Vales and Bunnell, 1988). Modelling of solar irradiance under forest canopies may be purely empirical, or may attempt to represent the physical processes of reflection, transmission and absorption by the canopy.

Attenuation of solar irradiance through a forest canopy is often described by Bouguer's law:

$$K_{bc} = K_{ac} \cdot e^{-kx} \tag{2.4}$$

where K_{bc} is incoming global radiation below canopy (Wm^{-2})
K_{ac} is incoming global radiation above canopy (Wm^{-2})
k is the extinction or absorption coefficient (m^{-1})
x is the path length through the canopy (m).

Baldocchi, Hutchison et al. (1984) found that, for a deciduous canopy, the decrease in insolation is approximately exponential throughout most of the canopy during all seasons. For a winter leafless forest, measurements of radiation at several levels within the canopy correspond well to an exponential relationship (Baldocchi, Matt et al., 1984). This is to be expected since a random distribution of plant elements, assumed as a first approximation, leads to the Poisson distribution for description of the probability of interception of sunlight through the canopy (Cohen and Fuchs, 1987; Lemeur and Blad, 1974).

The majority of studies dedicated to the radiation regime under forest canopies have dealt with coniferous forests (e.g., Gay et al., 1971; Mukammal, 1971; Wilson and Petzold, 1973), and have generally dealt with horizontal surfaces. Studies dealing with deciduous canopies have generally considered fully leafed situations (e.g., Myneni et al., 1989; Norman and Welles, 1983; Nunez, 1985), and are often primarily interested in photosynthetically active radiation (PAR) for biological growth studies. Results from studies dealing with the transmission of visible light, or PAR, however, do function as indices of the total solar energy transmitted (Jeffrey, 1968).

Lemeur and Blad (1974) critically reviewed studies concerned with modelling the light and radiation regimes of plant canopies. The review distinguishes between geometrical and statistical approaches for physically based models. Geometrical models may consider either single shapes or arrangements of shapes, assuming that shapes are regularly arranged and retain characteristic geometrical dimensions. In statistical models, vegetation is not considered as a composition of individual plants or shapes of physical dimension; instead, "the concept of individual plants is disintegrated to a display of leaves and stems which are not assigned to a certain (and identified) plant" (Lemeur and Blad, 1974, p. 257). In this case, it is the statistical distribution describing the display of plants (or plant elements) which becomes the important input parameter of the model. The authors deal primarily with theoretical statistics and the evaluation of microclimates of specific leaf or crop canopies through the description of type of leaf dispersion.

Recently, several geometrical approaches have been developed for determining the area and spatial distribution of shadows. Kuuluvainen and Pukkala (1987) considered cone-shaped bodies of several different height/radius ratios, analyzing the effect of crown shape on the total shaded area, and the effect of the spatial distribution of the trees on the total amount of shading. Sattler et al. (1987) presented a computer algorithm to determine the area and position of shadows cast by a tree or group of trees upon a surface of any slope and aspect. The program allows any combination of three basic shapes: sphere, cylinder or cone (upright or reversed). Granberg (1988) simulated conically shaped 'spruce trees' with 50-sided polygons of linearly decreasing radius, cast the shadow onto a (computer) memory plane, then counted the number of pixels that were shaded to determine the fraction of ground surface shaded. This method also allows determination of multiple shadow overlap. The author suggested that different tree types may be numerically simulated with a relatively high degree of similarity to existing trees, resulting in shadows which would behave more realistically than shadows resulting from basic geometric shapes.

2.3.3. LEAFLESS DECIDUOUS CANOPIES

Attenuation of solar radiation within a deciduous canopy is least during the leafless season, with approximately 50% or less of the light incident upon the canopy transmitted to the surface (Federer, 1971, Reifsnyder and Lull, 1966; Zavitkovski, 1982), although the range may vary significantly (Geiger, 1965). Hutchison and Matt (1977) report least attenuation during the spring leafless and spring leafing periods, values as low as 11% transmission of above-canopy irradiance during the winter leafless period, and approximately 15% transmission throughout the photosynthetically dormant period. Deciduous forests in the leafless stage show greater variation in solar irradiance at the surface than fully leafed canopies (Ovington and Madgwick, 1955, cited in Reifsnyder and Lull, 1966), due primarily to the extreme variability of the direct beam radiation. The importance of solar radiation to snowmelt, and the variability of the same in leafless deciduous forests, attest to the desirability of a model which considers the interaction of solar radiation with the forest canopy in terms of its physical characteristics.

Relatively few studies have dealt with the solar radiation regime under leafless deciduous canopies, and all of these have dealt with horizontal surfaces, or simply ignored the effects of slope and aspect (e.g., Baldocchi, Matt et al., 1984; Federer, 1971; Wang and Baldocchi, 1989). Hendrie and Price (1979) worked within a leafless deciduous forest during the snowmelt period, but were primarily concerned with defining empirical relationships between snowmelt and net radiation. They indicated that the net radiative flux above the canopy may be successfully used to estimate net radiation above the snowpack, and that global radiation above the canopy may be employed, with only slight loss of precision, if used with established relationships between global and net radiation above the canopy. Use of global radiation may be advantageous because it is both easily measured and routinely measured at meteorological stations. However, Price (1988), working in the same deciduous forest, determined that a simple regression of net radiation on global radiation is not appropriate in a deciduous forest during snowmelt, although a multivariate model combining both global radiation and air temperature is shown to explain 77% of the variance in net radiation above the snowpack.

Federer (1971) modelled the transmission of both the direct and diffuse components of solar radiation through a leafless canopy. This model combines elements of both the geometrical and statistical approaches. The crown space of the canopy, although not specifically described by a statistical distribution of tree branches, is assumed to be a homogeneous absorber of solar radiation, and relies upon Bouguer's Law to describe the extinction or absorption of solar radiation within the crown space of the canopy. Transmissivity through the crown space, then, is a function of the absorption coefficient and the path length. The stem space (Federer, 1971), however, is fully described by the physical characteristics of the forest stand, including tree height, basal area, stems per hectare and quadratic mean diameter. Parameterization of the stem space as shadow-casting cylinders allows an accurate portrayal of canopy transmissivity, ground reflection, and albedo of the forest stand, using a minimum of input data consisting of stand characteristics, surface albedo and beam radiation fraction of the above canopy irradiance. It was shown that solar irradiance at the surface varies according to the ratio of direct to diffuse radiation, solar zenith angle, surface albedo and canopy characteristics. This model is the basis for the present work, and is described in further detail in Chapter 3, sections 3.1, 3.1.1 and 3.1.2.

Two further studies require mention because of their attention to both slopes and forest canopies simultaneously. Hendrick et al. (1971) considered topographic and vegetative diversity over a large area (111 km^2) to analyze watershed snowmelt. 'Snowmelt environments' were determined according to elevation, slope degree and aspect, and forest cover. Solar radiation on slopes relative to that on an open horizontal surface was calculated as a function of slope degree and aspect, and topographic shading. However, all deciduous canopy was estimated to have crown closure of 0.3, regardless of differences in vegetative characteristics or diversity due to elevation or slope degree and aspect; this assumption seems low and needs to be tested.

Dozier (1979, 1980) developed a wavelength specific, solar radiation model for clear sky conditions which considers direct, diffuse and reflected radiation, and includes topographic calculations for slope, aspect and horizon, the latter incorporated into a horizon view factor. Although this model incorporates a beam shading function due to a forest canopy, the hemispheric-shading portion (diffuse) and beam-shading function (direct) are to be derived from skyward photographs, and are not based on the actual physical characteristics of the canopy (recent approaches to the photographic method are presented by Becker et al., 1989, and Herbert, 1987). Furthermore, the model does not seem to have been tested within a forested environment, and certainly not within a deciduous forest.

With the exception of the two previous models (Hendrick et al., 1971; Dozier, 1980), almost all the models have been limited to horizontal surfaces. None of the studies has dealt with the role of the physical characteristics of the forest canopy in interfering with the transmission of global radiation, and with realistic topographic environments, simultaneously. Furthermore, most of the studies have been limited to either clear sky data, or complete cloud cover conditions, and have often been analyzed on the basis of only several days' data, These studies, though, attest to the difficulty in either measuring or modelling the spatial and temporal distribution of solar radiation beneath forests in general, and deciduous canopies in particular, showing the need for a physically-based model adaptable to any cloud cover condition.

CHAPTER 3

DESCRIPTION OF THE MODEL

3.1. FEDERER'S MODEL

Federer (1971) analyzed the variations in the solar radiation regime of a deciduous forest in winter, modelling the transmissivity of both the direct and diffuse components of solar radiation through the leafless canopy for a horizontal surface. His theoretical model is based upon a two-layer canopy in which the upper layer (or crown space) is assumed to be a homogeneous and isotropic absorber, and the lower layer (or stem space) is assumed to comprise a random array of uniform right circular cylinders; both layers are assumed horizontally uniform and infinite.

3.1.1. BEAM RADIATION TRANSMISSION

The transmission of beam radiation through the crown space (t_o) follows from Bouguer's Law, and is given by:

$$t_o = \exp(-\alpha h_o \sec\theta) = \exp(-\alpha \cdot l_o) \tag{3.1}$$

where α is the crown space absorption coefficient (m^{-1})

h_o is thickness of the crown space, in direction normal to the horizontal, (m)

l_o is path length through the crown space, equal to $h_o \sec\theta$ for a horizontal surface, (m)

θ is solar zenith angle (rad), defined by:

$$\cos\theta = \sin\delta\sin\phi + \cos\delta\cos\phi\cos\Omega \tag{3.2}$$

where δ is solar declination (rad)

ϕ is site latitude (rad)

Ω is hour angle, solar noon zero, east positive (rad)

The following equation (Iqbal, 1983) is used to determine solar declination, in radians:

$$\begin{aligned}\delta = {} & 0.006918 - 0.399912\cos(\Gamma) + 0.07257\sin(\Gamma) \\ & - 0.006758\cos(2\Gamma) + 0.000907\sin(2\Gamma) \\ & - 0.002697\cos(3\Gamma) + 0.001480\sin(3\Gamma) \qquad (3.3)\end{aligned}$$

where Γ is day angle (rad) given by:

$$\Gamma = 2\pi(d_n-1)/365 \qquad (3.4)$$

where d_n is day number of the year, ranging from 1 to 365; it is assumed that February always has 28 days (Iqbal, 1983). Equation 3.3, used to calculate the values in Table 1.3.1 given in Iqbal (1983, pp. 8,9), gives more accurate values than the equation given in the text (Iqbal, 1983, p. 7), also given in Davies (1981, p. A14), when compared with selected values given by Bourges (1985) for the years 1969, 1979 and 1984.

The transmission of direct radiation through the stem space is a function of measurable stand characteristics, and is theoretically developed on the probability of clear lines of sight through a random array of vertical cylinders, uniform in height and diameter, and assumed to be nonreflecting. Federer's development of this theory is based upon a similar development by Kauth and Penquite (1967) which determines the probability of clear lines of sight through a bank of ellipsoidal cumulus clouds.

The surface shaded by a single cylinder may be described as a rectangle with a semicircle added at each end. The fraction (G) of a large unit area which is shaded by any number of cylinders will then be given by:

$$G = n_u \cdot dG = B[1+(4h_m/(\pi D))\tan\theta] \qquad (3.5)$$

where n_u is the number of cylinders or stems per unit area

dG is the fraction of unit area shaded by a cylinder or stem, given by:

$$dG = [(\pi D^2/4) + Dh_m\tan\theta]/U \qquad (3.6)$$

where D is cylinder or stem diameter (m)

h_s is cylinder height or stem space thickness (m)

U is unit area (ha)

B is basal area fraction, given by:

$$B = n_u \pi D^2/(4U) = n\pi D^2/4 \quad (3.7)$$

where n is the number of cylinders or stems (ha^{-1}), used to replace n_u/U.

The first term (B) in the right hand expression of equation 3.5 is negligible compared to the second term since zenith angle is usually greater than 45° for leafless canopies in winter, and the value of h_s/D is very large compared to basal area fraction. At the two experimental sites minimum zenith angles are 35° on 18 April at site 1 (immediately prior to first leafing) and 51° on 8 March at site 2. Therefore, equation 3.5 becomes

$$G = 4Bh_s \tan\theta/(\pi D) \quad (3.8)$$

when expressed in terms of basal area fraction (Federer, 1971), or

$$G = nDh_s \tan\theta \quad (3.9)$$

when expressed more directly in terms of area (length, width).

Calculation by equation 3.8 of the fractional area shaded, however, is an overestimate of the actual area shaded since some shadows will overlap. The random addition of another cylinder (or tree) to the random array results in the portion of the new shadow that overlaps another being equal, on the average, to the fraction of the total area already shaded (Federer, 1971). This may be expressed mathematically as:

$$(dG - dS)/dG = S_H \quad (3.10)$$

where dS is the additional fraction of area shaded by adding a cylinder or stem

S_H is the actual fraction of area shaded.

Rearrangement of equation 3.10 by solving for dG, along with integration from an initial condition of $S_H = G = 0$ for the addition of new shadows, results in the following:

$$G = -\ln(1-S_H) = -\ln(t_s) \tag{3.11}$$

where t_s is the stem space transmissivity, equal to the fraction of area not shaded $(1-S_H)$ since only beam radiation is being considered. Combining equations 3.11 and 3.8 results in the following expression for the stem space transmissivity:

$$t_s = \exp[(-4Bh_s\tan\theta)/(\pi D)] \tag{3.12}$$

This may be rewritten in terms of shadow area by combining equations 3.11 and 3.9:

$$t_s = \exp(-nDh_s\tan\theta) = \exp(-nA_s) \tag{3.13}$$

where A_s is the area of the shadow of a single cylinder or stem (m^2), equal to $Dh_s\tan\theta$ on a horizontal surface. The length of the shadow on a horizontal surface is $h_s\tan\theta$.

Direct beam transmissivity through crown and stem space is given by the product of equations 3.1 and 3.13:

$$t_o t_s = \exp[-\alpha h_o\sec\theta - (nDh_s\tan\theta)] \tag{3.14}$$

For this model, both h_o and h_s are considered to be equal to one-half the total tree height (h).

3.1.2. DIFFUSE RADIATION TRANSMISSION

The transmission of diffuse radiation through the canopy is modelled under the assumption of an isotropic hemisphere (Federer, 1971). The intensity of radiation from any particular direction on the horizontal ground surface, when integrated over the hemisphere, and divided by the diffuse radiation above the canopy, gives the diffuse transmissivity (t_d):

$$t_d = 2\int_0^{\pi/2} \exp[-\alpha h_o\sec\theta - (nDh_s\tan\theta)]\cdot\cos\theta\sin\theta\, d\theta \tag{3.15}$$

Total transmissivity (T) of the canopy to both direct beam and diffuse radiation is given by the sum:

$$T = t_o t_s F + t_d(1-F) \qquad (3.16)$$

where F is the ratio of direct to global radiation above the canopy.

3.2. MODEL EXTENSIONS AND ADJUSTMENTS

Two specific extensions have been adapted to Federer's model to allow application of the model to slopes of any degree and aspect. First, a generalized surface-canopy-sun geometry for slopes with vertical cylinders (as opposed to cylinders normal to the slope) requires generalized formulae for both the path length through the crown space and the area of shadows cast upon the surface, both of which are dependent upon solar zenith and azimuth angles, slope azimuth and slope degree. Secondly, derivation of the crown space absorption coefficient requires calculation of incident solar irradiance (both direct and diffuse) above the canopy for a slope equivalent to the site slope.

The extended model has also incorporated measurements of the fraction of global radiation which is direct beam (as suggested by the author) rather than rely upon empirical relationships to determine this ratio. This is especially important for large zenith angles on clear days (Federer, 1971). Furthermore, the inclusion of a large data set of successive values allows integration over time for hourly and daily time periods.

3.2.1. ALLOWANCE FOR SLOPES OF ANY DEGREE AND ASPECT

For this research project, R.D. Moore (personal communication, see Appendix A) developed the following formulae for a generalized surface-canopy-sun geometry, thereby allowing the model to be extended to slopes of any degree and aspect (or azimuth). Path length and shadow area are now given by:

$$l_o = h_o\cos\beta/[\sin\beta\sin\theta\cos(z_1-a) + \cos\beta\cos\theta] \qquad (3.17)$$

$$A_s = Dh_s\sin\theta/[\sin\beta\sin\theta\cos(z_1-a) + \cos\beta\cos\theta] \qquad (3.18)$$

where β is slope inclination (rad)
z_1 is solar azimuth, east zero, north positive (rad)
a is slope azimuth, east zero, north positive (rad).
The beam radiation transmissivities which are not restricted to horizontal surfaces but which allow for slopes of any degree and aspect may now be developed:

$$t_o = \exp(-\alpha \cdot l_o) = \exp[-\alpha h_o\cos\beta/\cos(i)] \qquad (3.19)$$

$$t_s = \exp[-nA_s] = \exp[-nDh_s\sin\theta/\cos(i)] \qquad (3.20)$$

where i is solar incidence angle (rad), the angle between the normal to a slope and the solar ray, defined by:

$$\cos(i) = \sin\beta\sin\theta\cos(z-\sigma) + \cos\beta\cos\theta \qquad (3.21)$$

where σ is slope azimuth, south zero, east positive (rad)
z is solar azimuth, south zero, east positive (rad), defined by:

$$\cos(z) = (\cos\theta\sin\phi - \sin\delta)/(\sin\theta\cos\phi) \qquad (3.22)$$

(Solar azimuth is defined conventionally for south zero, east positive (Iqbal, 1983; Kondrat'yev, 1977; Walraven, 1978). For this study, terminology has been kept as much as possible in the original terms; hence, several different symbols have been used for solar azimuth angle, hour angle, etc., depending upon its definition. In all cases, simple transformations may be applied to reconcile the different conventions.)
Direct beam transmissivity through both crown and stem space for the general case of sloping surfaces is then given by:

$$t_o t_s = \exp[(-\alpha h_o\cos\beta - nDh_s\sin\theta)/\cos(i)] \qquad (3.23)$$

Obled and Harder (1979) presented a formula for calculating diffuse irradiance on a slope which accounts for the effects of surrounding topography. Equation 3.24 may be similarly derived for the transmissivity of the canopy to diffuse radiation for a sloping surface:

$$t_d = [1/(\pi K_s)] \int_0^{2\pi}\int_0^{\theta(z)} t_o t_m \cos(i)\sin\theta \, d\theta dz \qquad (3.24)$$

where $\theta(z)$ is maximum solar zenith angle as a function of solar azimuth angle (rad)

K_s is the reduction factor for slope and topographical obstacles on the 360° horizon, and is given by:

$$K_s = (1/\pi) \int_0^{2\pi}\int_0^{\theta(z)} \cos(i)\sin\theta \, d\theta dz \qquad (3.25)$$

Total transmissivity of the canopy for a sloping surface is then given by equation 3.16, where $t_o t_m$ and t_d have the new values assigned by equations 3.23 and 3.24. Beam radiation transmissivities for sloping surfaces, however, must respect the limits on zenith angle for a given solar azimuth angle dependent upon slope degree and aspect; i.e., both t_o and t_m equal zero if either the slope itself or topographical obstacles obstruct the direct solar beam. Diffuse radiation transmissivity remains a constant for a given site.

3.2.2. CALCULATION OF DIRECT AND DIFFUSE RADIATION ON SLOPES

Garnier and Ohmura (1968) developed an expression which relates direct shortwave radiation received on a surface normal to the sun's rays (I_m) to that received upon a surface of any slope and aspect (I_s):

$$I_s = I_m \cos(\mathbf{X} \cap \mathbf{S}) \qquad (3.26)$$

where $\mathbf{X}$ is a unit vector normal to (and pointing away from) the slope

$\mathbf{S}$ is a unit vector expressing height and position of the sun

$\cap$ denotes the angle between $\mathbf{X}$ and $\mathbf{S}$.

$\cos(X \cap S)$ is defined by:

$$\cos(X \cap S) = \{[\sin\phi\cos(H)][-\cos(A)\sin(Zx)] - \sin(H)[\sin(A)\sin(Zx)] + [\cos\phi\cos(H)\cos(Zx)]\}\cos\delta + \{\cos\phi[\cos(A)\sin(Zx)] + \sin\phi\cos(Zx)\}\sin\delta \quad (3.27)$$

where H is hour angle, solar noon zero, west positive (rad)
A is slope azimuth, north zero, east positive (rad)
Zx is zenith angle of the vector **X**, or slope inclination (rad).

Note that equation 3.27 also defines the solar incidence angle and is equivalent to equation 3.21, but does not require calculations concerning solar zenith and solar azimuth angles (Iqbal, 1983; Kondrat'yev, 1969). The beam radiation on a surface normal to the sun's rays is related to the beam radiation on the horizontal (I_H) by the following:

$$I_m = I_H/\cos\theta \quad (3.28)$$

Diffuse radiation on a horizontal surface (D_H) must also be related to the diffuse radiation received upon a slope of any degree and aspect (D_S). Obled and Harder (1979) develop the necessary equation, assuming isotropic distribution:

$$D_S = (D_H/\pi) \int_0^{2\pi}\int_0^{\theta(z)} \cos(i)\sin\theta \, d\theta dz \quad (3.29)$$

The value cos(i) in equation 3.29 reduces the diffuse radiation incident upon the slope due to the slope itself (degree and aspect), while the upper limits on the inner integral reduce the diffuse radiation due to the surrounding topographical obstacles. The reduction factor for the given slopes at sites 1 and 2 must be evaluated numerically, but once the integration has been performed this reduction becomes a constant, such that equation 3.28 may now be written as:

$$D_S = K_S D_H \quad (3.30)$$

where K_S is the reduction factor for slope and topographical obstacles on the 360° horizon, defined in section 3.2.1, equation 3.25.

3.3. NUMERICAL METHODS

TURBO Pascal computer programs are used for data preparation, model calculations, and assessment of model performance through validation statistics. Repeated one-dimensional integration (using Simpson's rule for each of the integrals) is used to approximate the values of the double integrals found in equations 3.24, 3.25 and 3.29 concerning diffuse radiation on slopes. The inner integral is evaluated using intervals of 0.5° zenith angle; upper limits are determined by horizon topography (including the slope itself) in the direction of the azimuth angle (outer integral). Integration over azimuth angle is accomplished using 15° intervals. The larger degree interval is used for two reasons: first, horizon topography was measured every 30° over the 360° horizon and, secondly, the additional computer time required for solution of the equations cannot be justified by an increase in accuracy. Equation 3.24, evaluated using 1° azimuth angle intervals (with interpolation for maximum zenith angles at intervening azimuth angles), resulted in the same values to three decimal places as when using 15° azimuth angle intervals. Arnfield (1987) has studied in detail the problem involved with generalizing topographical obstacles on the horizon.

CHAPTER 4

DATA COLLECTION AND PROCESSING

4.1. STUDY SITES

Data collection was carried out at the Université de Montréal biological research station (45°59'N, 74°01'W) at St. Hippolyte, Québec, approximately 70 km NNW of Montréal, Québec. The station is at an elevation of 350-400 masl, and is surrounded by a mixed deciduous forest comprising primarily maple, birch and beech trees. The availability of a tower reaching above the canopy (at 20 m) and daily weather observations influenced the choice of this site. Figure 4.1 shows the location of the research station and the field sites.

Two field sites of different slope inclination and orientation were selected, each rectangular in shape with an area of approximately 300 m^2 (15 m X 20 m) and about 1 km from the tower site. Site 1 faces almost directly south (178° from true north, east positive) and has a slope of 13°. Site 2 faces approximately NNW (339°) and has a slope of 12°. Horizon topography due to obstacles other than the slope itself was measured from the center of the experimental site at 15° intervals (from 0-360°) in order to ensure correct calculations for incoming direct solar irradiance, and to lower the diffuse solar irradiance values due to the diminished hemisphere. At site 1, horizon topography ranges from -1.5° to 5.5° from the horizontal (at 105° and 225° from true north, respectively), and at site 2 horizon topography ranges from -1.5° to 1.0° (at 0° and 60°). Horizon topography was taken into account when determining hours of sunrise and sunset for a given site, and for determination of the decreased hemisphere for diffuse radiation. Both sites were chosen with the intention of minimizing the effects of direct and diffuse

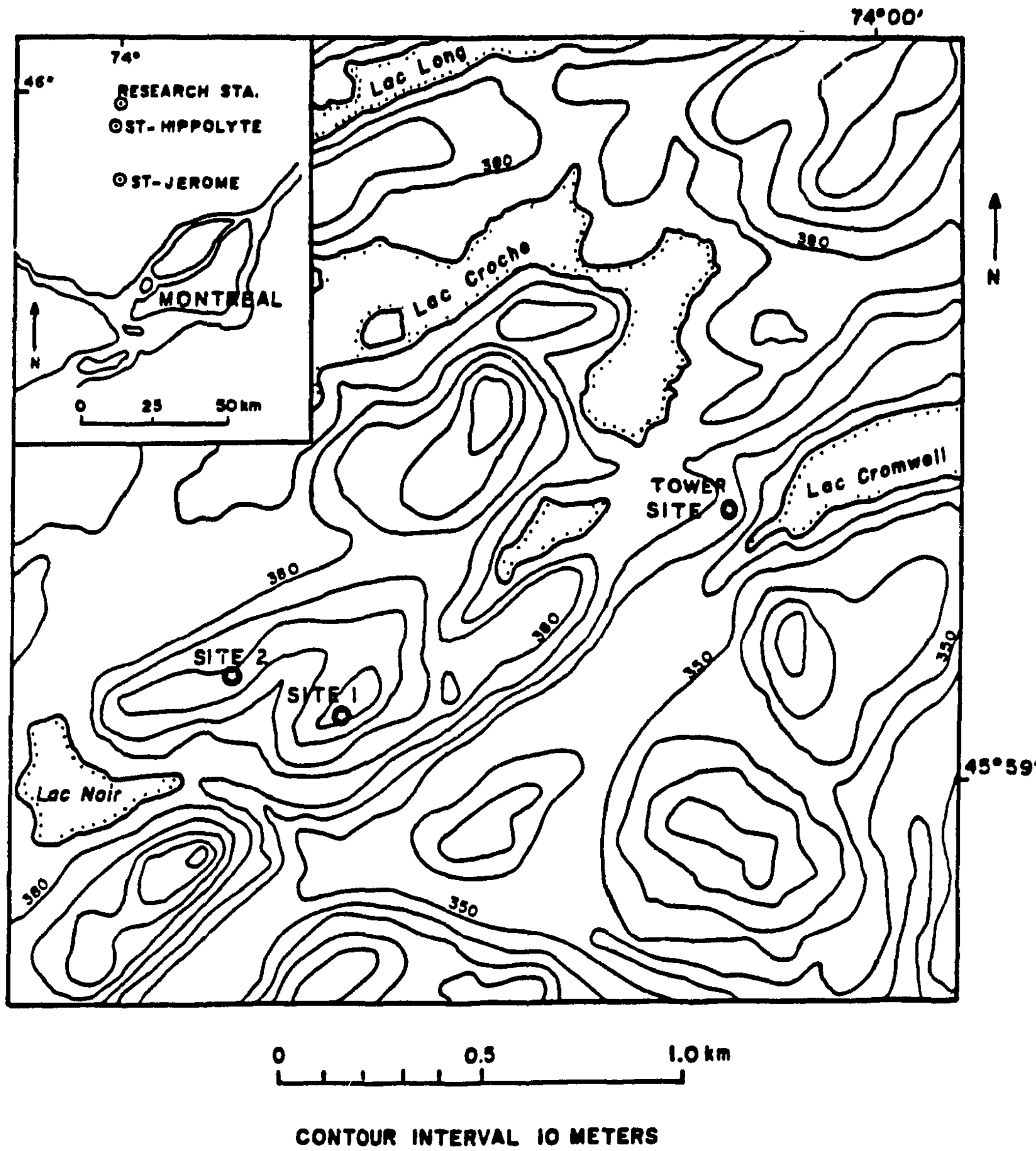

FIGURE 4.1. Location of field sites and tower site at the biological research station (Université de Montréal), St-Hippolyte, Québec. Sources: Ministère de l'Energie et des Ressources, 31G-16-200-0202 Ste-Adèle, 1984; (inset) Transports Québec, 1988.

radiation reflected from surrounding terrain, as well as edge effects due to abrupt or major changes in the forest stand characteristics.

Site and stand characteristics for the two sites are summarized in the first two sections of Table 4.1; model parameters are included in this table for comparison with values given by Federer (1971, p.8). Slope degree and aspect were determined with the aid of an abney level and a compass. Slope degree was taken as the average slope between the top of the site and the bottom of the site, along a line parallel to the site azimuth. Stand parameters were measured or calculated for each entire site independently. Tree height refers to the average height of the top of the canopy and, as such, is subject to significant error because of the difficulty in determining which tree tops are representative of the top of the canopy. Both arithmetic mean diameter and basal area fraction are calculated from measurements of tree circumference at breast height (1.4 m). Although both mean diameter and stems per hectare are greater at site 1 than at site 2, basal area fraction is the same for both sites; this apparent incongruity results from the use of arithmetic mean diameter rather than quadratic mean diameter, as discussed in chapter 5, section 5.2.2. Table 4.1 does not evidence the fact that more undergrowth (from 1.25-1.75 cm diameters) was apparent at site 2 during the greater portion of the data collection period than at site 1.

Dates of spring melt vary slightly from year to year, but peak snowmelt usually occurs during the last week of March and the first week of April, and all snow usually disappears by late April. For 1987 the spring melt ran from approximately 25 March to 10 April. First leafing begins during the last two weeks of April (20 April in 1987), and the leafing period usually lasts through the first two weeks of May. Leaf fall occurs during the last two weeks of October.

Table 4.1: Site and stand characteristics, model parameters and sampling dates.

	site 1	site 2
Site characteristics:		
slope, β (deg)	13	12
aspect, A (deg)	178	339
Stand characteristics:		
tree height, h (m)	15.2	16.0
arithmetic mean diameter, D (m)	0.100	0.096
stems per hectare (over 1.25 cm), n_u	3190	3128
basal area fraction, B	0.00359	0.00359
Model parameters:		
crown & stem height, h_c, h_s (m)	7.6	8.0
absorption coefficient, α (m^{-1})	0.011	0.018
Data collection dates (1987):	6/3-21/3 13/4-19/4	21/3-13/4

4.2. DATA COLLECTION

Instrumentation in the field consisted of eleven Kipp & Zonen (Moll-Gorczynski type) solarimeters, including nine CM-5 and two CM-2 types, and one Mark I-G Sol-A-Meter (temperature-compensated, silicon photovoltaic cell type) pyranometer. Instrument error for Kipp & Zonen solarimeters is estimated to be 3.6% (RMSE), with a cosine response of +5 percent at 10° solar elevation (Latimer, 1972). Ten pyranometers were set up at a given site at one time, each parallel to the gradient of slope and oriented to the same aspect as the site itself. Instruments were transferred between sites (from site 1 to site 2 and back to site 1) so that each site was monitored during different types of weather and snow cover conditions. Data were collected at site 1 during 19 days (8-20 March and 13-18 April 1987, inclusive), and at site 2 during 21 days (22 March - 11 April 1987).

Instrument locations within each site were determined by random number generation to specify distance along two coordinate axes from a grid origin point at one corner of each plot. It was decided beforehand that if a pair of random coordinates fell on a spot occupied by a tree then 0.5 m would be added to the second coordinate. The same random locations generated for site 1 were retained for site 2, and again when the instruments were returned to site 1, using the same instrument stands for the same instruments as during the earlier data collection period. Instrument gradient and azimuth settings were verified twice weekly. Gradient settings generally remained constant and never exceeded ±2 degrees. Azimuth settings, however, varied more due to warping of the wood posts used for the instrument stands; maximum variations in azimuth settings were approximately ±5 degrees. Instruments were kept at a constant height relative to the forest canopy above them rather than the snow surface below them.

Readings of global radiation at the field sites were initiated every minute and averaged (for each solarimeter) over twenty-minute intervals by a Campbell Scientific 21X Micrologger. The 20-minute averages were later spatially averaged to determine mean solar irradiances for the site, providing *in situ* observations of solar irradiance to compare with the model predictions. Photographs of the field sites and instrumentation are shown in Figure 4.2 (a, b and c).

Global and diffuse radiation above the canopy were measured from a tower near the station using two solarimeters, one of which was combined with a shadow band (Figure 4.3) built to specifications given by Horowitz (1969). A Campbell Scientific CR7 datalogger was used to record the instantaneous solar irradiance values, initiated at the same times as at the field sites and similarly averaged over twenty-minute intervals, providing overall site income of solar irradiance upon a horizontal surface without canopy interruption. Data from the sites, stored temporarily on the dataloggers, were subsequently transferred to computer storage. Appendix B presents the data graphically for each of the ten pyranometers at the forest floor (20-minute averages of instantaneous solar irradiance values) as well as for global and diffuse radiation above the canopy.

4.3. INSTRUMENT CALIBRATION

Two of the Kipp and Zonen CM-5 solarimeters were sent to the National Atmospheric Radiation Centre (Atmospheric Environment Service, Downsview, Ontario) for calibration by the integrating sphere method (Hill, 1966; Latimer, 1966; Drummond and Greer, 1966). The ten remaining pyranometers were then calibrated by comparison with these two reference radiometers, using 960 data points at an average temperature of 16.8°C for each of the Kipp & Zonen solarimeters, and 600 data points at an average temperature of 15.4°C for the Sol-A-

FIGURE 4.2a. Typical view of the leafless deciduous canopy, south-facing site, illustrating the difficulty in parameterizing the transmissivity of the crown space to solar radiation.

FIGURE 4.2b. Randomly located Kipp & Zonen solarimeters at the south-facing slope, adjusted to the same inclination and orientation as the slope itself, 15 March 1987 (Julian day 74). This view illustrates the spatial variability of shadows and and the variations of solar radiation at the surface.

FIGURE 4.2c. Solarimeters and data logger under diffuse sky conditions, south-facing site, 15 March 1987 (Julian day 74).

FIGURE 4.3. Solarimeter with shadow band installed for measuring diffuse radiation above the canopy (corrections are later made for the portion of the hemisphere blocked by the band itself). Photo taken during first-leafing, immediately after the data collection period.

Meter pyranometer. Coefficients for temperature dependence were determined for each solarimeter before calibration (using two instantaneous readings at temperatures of 11.4°C and 19.3°C) by comparison with the one solarimeter for which both temperature coefficient and calibration factor were known.

The instantaneous readings used for calibration purposes were taken every minute during 14 hours of sunshine and 2 hours of slight overcast conditions, collected at an open site immediately after the field data collection period. These particular values were chosen because the traces of the plotted data were "sufficiently high and reasonably smooth" (Latimer, 1972), as shown in Figure 4.4 for 8 May 1987, when data were selected between 700 and 1500 LST. The lower trace in Figure 4.4 corresponds to the Sol-A-Meter pyranometer which has a lower sensitivity (approximately 50 mV per Wcm^{-2}) than the Kipp & Zonen solarimeters (115 mV per Wcm^{-2}), and exhibits spectral response for a slightly shorter wavelength range. Calibration factors, along with derived coefficients for temperature dependence, were then used to convert the field data to solar irradiance in Wm^{-2}.

4.4. SHADOW BAND CORRECTION

Diffuse radiation measurements made in conjunction with a shadow band must be corrected in order to compensate for the portion of the hemisphere blocked by the band. Latimer (1972), Coulson (1975) and Iqbal (1983) all describe similar methods for determining the shadow band correction factor, although one method requires hour angle at sunset and another uses solar azimuth angle. This study uses Latimer's formula, where the fraction of the hemispherical diffuse radiation that is obscured by the ring, assuming an isotropically diffuse sky, is given by:

$$F_1/D_H = [2w/(\pi\tau)]\cos^3\delta[t_o\sin\phi\sin\delta + \cos\phi\cos\delta\sin(t_o)] \qquad (4.1)$$

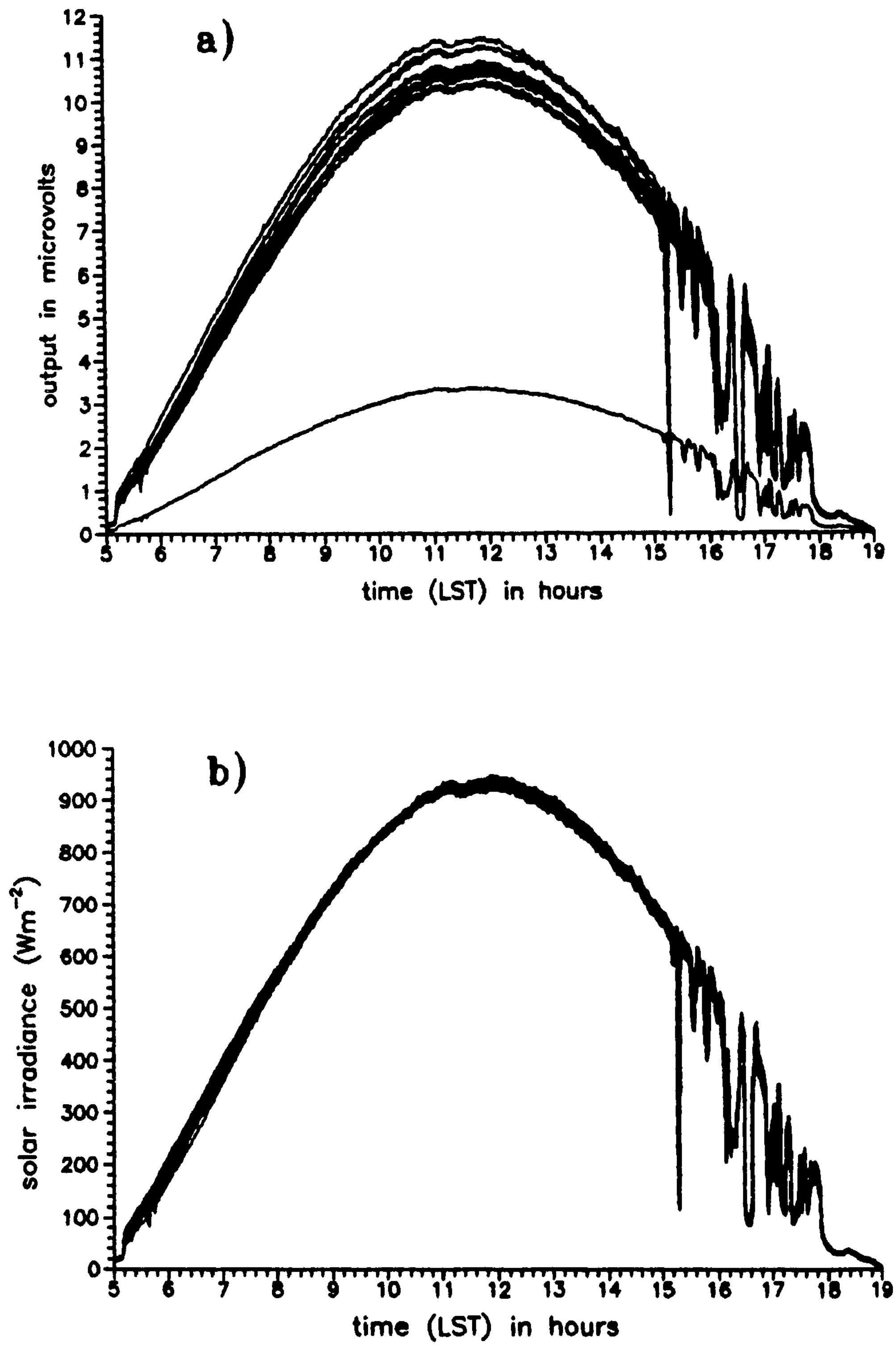

FIGURE 4.4. Solar irradiance data for 12 pyranometers for 8 May 1987: a) before calibration and b) after calibration. Data from 700 - 1500 LST were used for instrument calibration.

where F_1 is diffuse radiation from the portion of hemisphere blocked by the shadow band (Wm^{-2})

w is the width of the shadow band (m)

r is the radius of the shadow band (m)

t_o is hour angle of the sun at sunset (rad).

The following equation (Iqbal, 1983) is used to determine hour angle at sunset, in radians:

$$t_o = \cos^{-1}(-\tan\phi\tan\delta) \quad (4.2)$$

The correction factor (K_b) to be applied to the diffuse data measurements is given by:

$$K_b = 1/[1 -(F_1/D_H)] \quad (4.3)$$

A further correction of +4% is added to "relate isotropic to average real sky conditions" (Drummond, 1964). Direct beam radiation is then simply global radiation minus the corrected diffuse radiation.

4.5. SAMPLING VARIABILITY

A simple analysis of the spatial and temporal variations in the solar irradiance incident upon the forest floor was undertaken in order to determine the variability amongst the ten solarimeters, and the standard error of the mean, for particular data sets. The standard errors can then be used to estimate the precision of the observed irradiance values. The analysis was performed on the entire data set (verification and calibration data sets combined), and on subsets determined as a function of daily sky condition, combining data from sites 1 and 2 in both cases. Figure 4.5 depicts well both the spatial and temporal variability of solar irradiance at the forest floor under the leafless deciduous canopy for two representative days with sunny sky conditions. Figures 4.6 and 4.7 show the differences in variability of solar irradiance for representative days with partial cloud and overcast sky conditions, respectively. For further examples of the

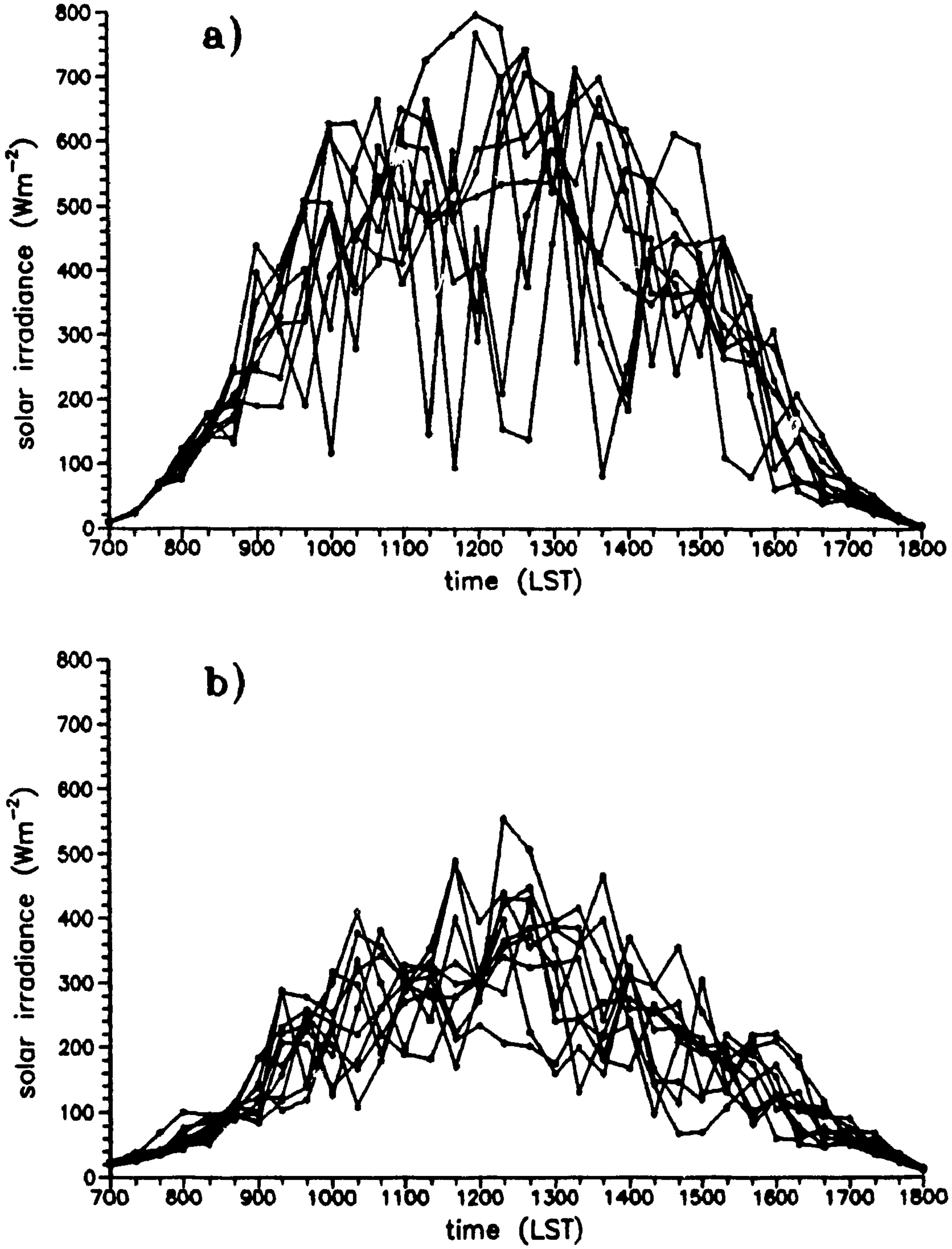

FIGURE 4.5. Solar irradiance data for 10 instruments under leafless deciduous canopy, sunny sky conditions: a) 9 March at site 1, and b) 23 March at site 2.

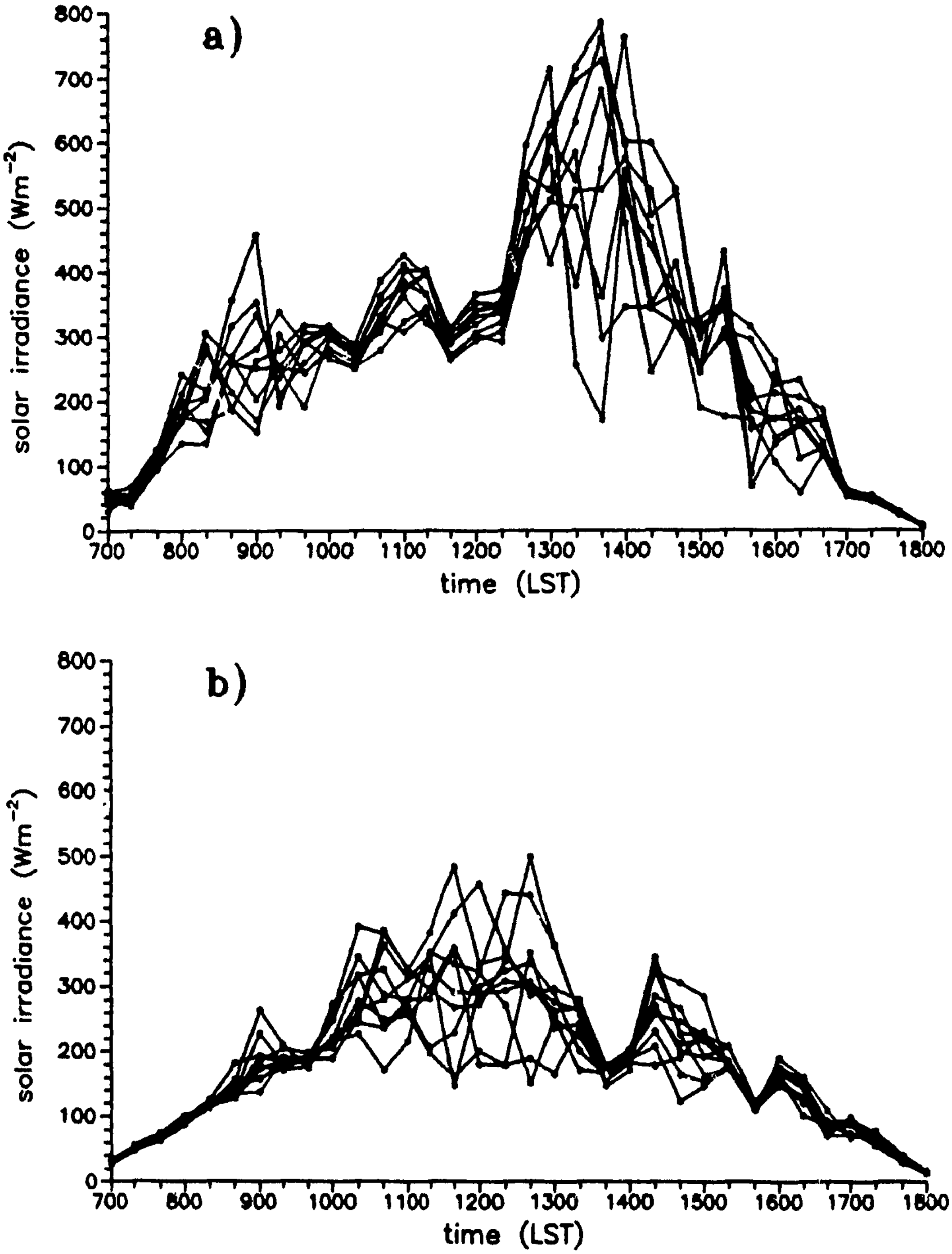

FIGURE 4.6. Solar irradiance data for 10 instruments under leafless deciduous canopy, partial cloud sky conditions: a) 19 March at site 1, and b) 29 March at site 2.

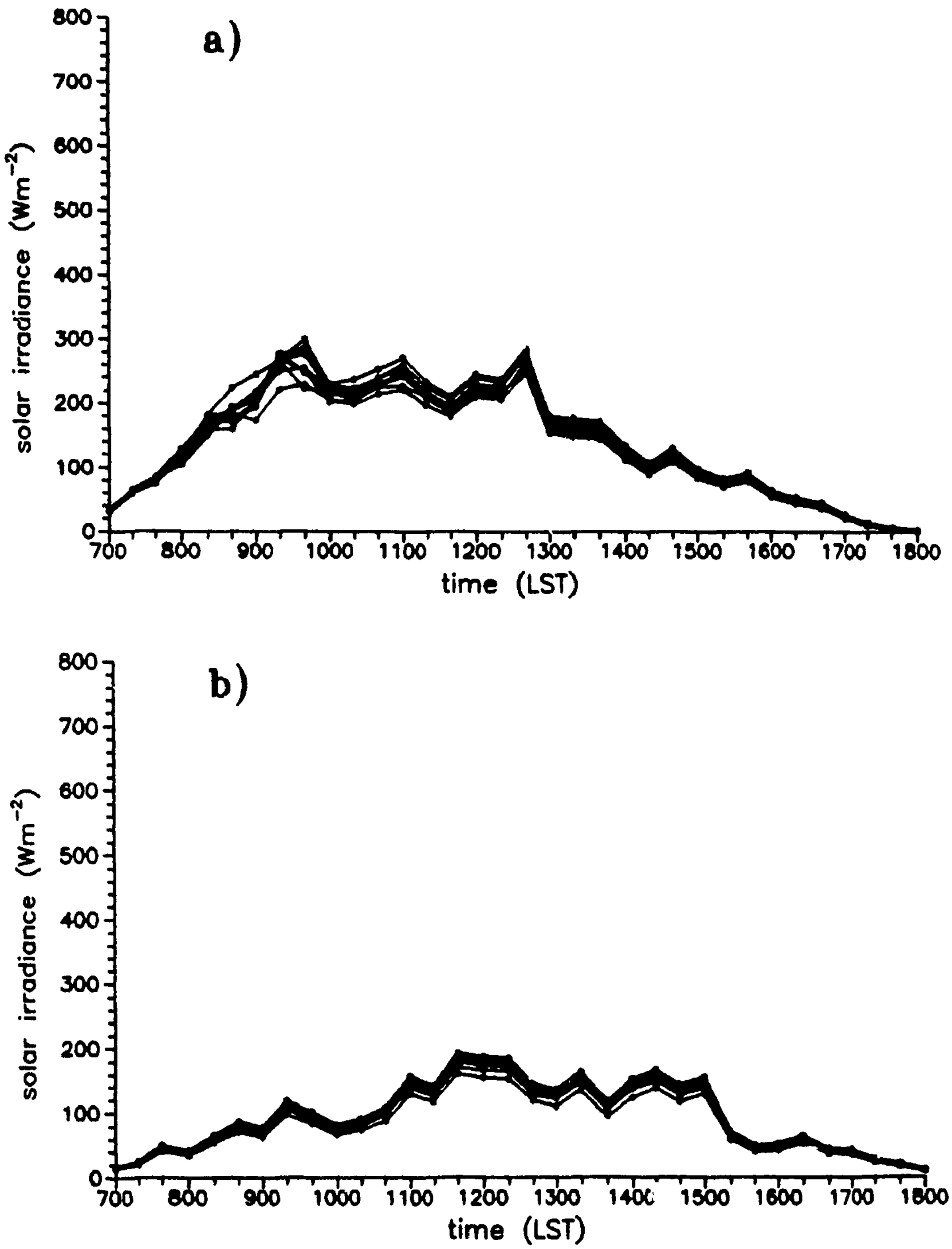

FIGURE 4.7. Solar irradiance data for 10 instruments under leafless deciduous canopy, overcast sky conditions: a) 16 March at site 1, and b) 27 March at site 2.

spatial variability of solar irradiance at the forest floor, see Appendix B.

Mean irradiance values should be representative of the canopy radiation regime within a leafless canopy since the frequency distribution of solar radiation at the surface is approximately normal (Baldocchi, Hutchison et al., 1984). According to Baldocchi et al. (1986) the distribution of photosynthetically active radiation (PAR) is slightly skewed, but the authors conclude that the mean irradiance values are, nevertheless, reasonable indicators of the radiation regime. Mean values of solar irradiance at the forest floor (from ten pyranometers) are presented in Appendix C as observed values.

For hourly and daily time periods, the original 20-minute averaged observations were further averaged over the appropriate time period. Standard deviations were calculated for the individual observations (10 radiometers), averaged for the particular data set, then used to determine coefficient of variation and standard error of the mean for that data set. Table 4.2 shows average standard deviation, coefficient of variation, and standard error of the mean for each of the data sets and averaging periods. Standard error of the mean (SE) is estimated by:

$$SE = SD/N^{(0.5)} \tag{4.4}$$

where SD is the sample standard deviation

N is the number of observations (instruments).

A bound on the difference between the sample mean and the true population mean can be calculated for a given level of significance (α_t) by:

$$B_m = \pm\, t(\alpha_t/2)\cdot SE \tag{4.5}$$

where B_m is the error bound

$t(\alpha_t/2)$ is the t-statistic for (N-1) degrees of freedom at the α_t-significance level.

The last column of Table 4.2 shows the calculated error bounds for a 95% confidence level (α_t = 0.05).

TABLE 4.2: Sampling variability for solar irradiance at the forest floor, as shown by coefficient of variation (CV%) in percentages and standard error of the mean (SE) in Wm^{-2} for data sets determined as functions of daily sky condition. Avg irrad and Avg SD are average solar irradiances and standard deviations in Wm^{-2}; n refers to the sample size for average solar irradiance. The last column gives error bounds for a 95% confidence level (values are ±). All values are for verification and calibration data sets combined.

Data set	Averaging period	Avg irrad	Avg SD	n	CV%	SE	95% bound
total set	20-min	202.0	42.2	1290	20.9	13.3	30.1
	hourly	202.0	32.0	430	15.8	10.1	22.8
	daily	209.6	17.1	38	8.2	5.4	12.2
overcast	20-min	106.9	9.0	450	8.4	2.8	6.3
	hourly	106.9	8.2	150	7.7	2.6	5.9
	daily	111.9	7.2	13	6.4	2.3	5.2
partial cloud	20-min	231.0	46.9	519	20.3	14.8	33.5
	hourly	231.1	35.9	173	15.6	11.4	25.8
	daily	235.4	19.5	15	8.3	6.2	14.0
sunny	20-min	288.4	81.2	321	28.2	25.7	58.1
	hourly	288.4	58.7	107	20.4	18.6	42.1
	daily	297.9	26.2	10	8.8	8.3	18.8

Reifsnyder et al. (1971) found that the diffuse radiation under both coniferous and fully leafed deciduous canopies is extremely uniform and, therefore, easy to sample. The variability associated with the direct component of solar radiation, however, requires a greater number of instruments for adequate sampling. This becomes evident in Table 4.2 when comparing different sky conditions, whether one considers coefficient of variation, standard error of the mean, or 95% precision bounds. On generally overcast days, the error bound changes only slightly with increasing time-averaging periods. On the other hand, on sunny days and partially cloudy days error bounds are much greater than for overcast conditions, although increasing the averaging period greatly reduces the error bound in each case. When sites 1 and 2 are analyzed separately for the total data sets, the variability (measured by the coefficient of variation) is from 13% to 27% higher for the south-facing site than for the north-facing site because of the smaller solar incidence and solar zenith angles encountered, and the resultant increases in direct beam penetration and variability associated with smaller angles.

The large number of radiometers required to estimate below-canopy global radiation adequately may be attributed to the penetrating direct component of solar radiation, and the resulting variations due to shadows moving across the forest floor. This has been documented by Reifsnyder (1971) for a fully leafed hardwood stand, and becomes apparent for the leafless deciduous forest when sky condition is considered. Table 4.3 gives the number of radiometers required to limit sampling error to within 5% of the average solar irradiance for different sky conditions. The last column of Table 4.3 gives the number of radiometers required to limit the error bound to ±5% of the average solar irradiance (for $\alpha_t = 0.05$). Values are calculated using equations 4.4 and 4.5 (solved for N and SE, respectively), along with standard deviation and solar irradiance values given in Table 4.2.

Table 4.3: Number of radiometers necessary to keep standard error of the mean (SE) or error bound (B) within 5% of the average solar irradiance for the particular sky condition. n refers to the sample size. All values are for verification and calibration data sets combined.

Data set- sky condition	Averaging period	n	No. of radiometers (SE=5%)	 (B=5%)
Total set	20-min	1290	18	90
	hourly	430	11	52
	daily	38	3	14
overcast	20-min	450	3	15
	hourly	150	3	12
	daily	13	2	9
partial cloud	20-min	519	17	85
	hourly	173	10	50
	daily	15	3	14
sunny	20-min	321	32	183
	hourly	107	17	85
	daily	10	4	18

For 20-minute averaging periods, only three radiometers would be required to limit solar irradiance values to within 5% of the average value for overcast sky conditions. This contrasts greatly with the number of radiometers required for 20-minute averages under partial cloud sky conditions (17) or sunny sky conditions (32). For daily averaging periods, the number of radiometers required is greatly reduced; furthermore, the differences in number of radiometers required for each of the sky conditions are also greatly reduced. However, even for hourly averages, and under an apparently homogeneous canopy, a large number of radiometers is required to limit the error bounds to ±5% at the 95% confidence level.

In comparison to the figures given in Table 4.3, Reifsnyder et al. (1971, p. 34) established that for sunny sky conditions and a desired standard error of the mean of approximately 10% of the average irradiance, 11 radiometers would be required to measure direct or global solar irradiance below a fully leafed deciduous canopy for 30-minute averaging periods; for hourly or daily averaging periods, the number of radiometers required are 8 and 1, respectively. For a coniferous canopy the equivalent numbers are 234, 174 and 10 radiometers, but for an allowable error of approximately 3.5% of the mean solar irradiance.

Table 4.3 also shows that, for ten solarimeters at a site, averaging intervals should be no less than one hour to keep the standard error within 5% of the average for the total data set; the same is true for partially cloudy sky conditions. For overcast sky conditions averaging periods may be much shorter, while for sunny sky conditions the averaging period must be greater than hourly. However, note that small changes in the allowable error will result in large changes in the number of radiometers needed, or time averaging period required, to remain within a given level of precision; doubling the allowable error results in a fourfold reduction in radiometers required.

CHAPTER 5

APPLICATION OF THE MODEL

5.1. INTRODUCTION

Model performance is assessed by means of validation statistics, namely, the root mean square error and the mean bias error. These statistics are calculated not only for the verification data sets, but also for data subsets determined as functions of cloud cover, solar incidence angle, solar zenith angle, and ratio of direct to global solar irradiance. This allows an analysis of the variability of solar irradiance for different sky conditions and different solar positions, the latter related to time of day.

Sensitivity analysis is carried out to determine how the model reacts to changes in specific input parameters such as tree height and diameter, basal area fraction, stand density, and slope inclination and orientation. Finally a simple analysis of the spatial and temporal variation of the incident radiation is undertaken to evaluate (1) the number of radiometers required to estimate solar radiation for different time averaging intervals and (2) the most appropriate time averaging interval for a given number of instruments, in order to keep irradiance estimates at a predetermined level of precision.

5.2. MODEL CALIBRATION

5.2.1. DERIVATION OF THE CROWN SPACE ABSORPTION COEFFICIENT

Model calibration requires fitting of the crown space absorption coefficient (α) to the measured transmissivity data. The absorption coefficient for a given site may be determined by minimizing the difference between the predicted and observed values, or expressed mathematically:

$$\Sigma\,[T \cdot K_{ao} - K_{bo}] = 0 \tag{5.1}$$

where the absorption coefficient (α) is contained in the total transmissivity of the canopy (T). K_{bo}, global radiation below the canopy, is a measured value. K_{ao}, global radiation above the canopy incident upon a sloping surface equivalent to the site slope, is given by

$$K_{ao} = I_S + D_S \tag{5.2}$$

as determined in section 3.2.2.

Equation 5.1 may be solved for the crown space absorption coefficient using a numerical approach such as the secant method to provide a rapidly converging solution (Press et al., 1987). The more common Newton-Raphson method cannot be used because the complexity of the function eliminates an evaluation of its derivative at arbitrary points. The numerical solution of equation 5.1 by the secant method results in a minimum for the predicted minus observed values and is, therefore, equivalent to minimizing the absolute value of the mean bias error (MBE). This method eliminates the possibility of determining α by minimizing the root mean square error (RMSE) because of the improbability that this function would have a real root (i.e., RMSE = 0).

A finite difference approach allows determination of the crown space absorption coefficient through minimization of either the MBE or RMSE. By calculating the RMSE and MBE for each value of α when allowed to vary throughout a given range, one may then determine that value of α which results when the RMSE or MBE is minimal; this is equivalent to determining the value of α for which d(RMSE)/d(α) is closest to zero. For verification of the extended model, this study uses values for the crown space absorption coefficient determined by means of minimizing the root mean square error; this minimizes the total error in a manner similar to least squares regression analysis.

The crown space absorption coefficient was determined for sites 1 and 2 by splitting the data set at each site into two sets of approximate equal size, one set to be used to calculate the absorption coefficient (calibration data set), the other set to be used as an independent test of the model (verification data set). Random splitting of the data sets is not employed because of the limited number of days at each site and the desire to ensure a value for α which might be representative of the weather types encountered. Thus, a stratified random procedure is employed. Data sets for each site were first divided into three subsets according to sky condition: clear sky, partial cloud and total overcast. One-half the days in each of these subsets were then selected at random to make up the calibration set. Appendix B presents data for the entire collection period, including both the calibration and verification data sets.

Figures 5.1 and 5.2 graphically portray RMSE and MBE for varying values of the (crown space) absorption coefficient for sites 1 and 2, respectively, showing both calibration and verification data sets at each site. These graphs also show the sensitivity of the model to the absorption coefficient. The RMSE is not very sensitive to small changes in α; however, the MBE is more sensitive, resulting in systematic under- or over-estimation if the absorption coefficient is not properly chosen.

The optimal alpha values at each site are the same for the calibration and the verification data sets when determined by minimizing the RMSE (Figures 5.1 and 5.2) and limiting precision to three decimal places. These values are 0.011 and 0.018 (m^{-1}) for sites 1 and 2, respectively. When determining the absorption coefficient by means of minimizing the MBE, optimal values vary slightly. At site 1, optimal alpha values are 0.009 (calibration data set) and 0.010 (verifica-

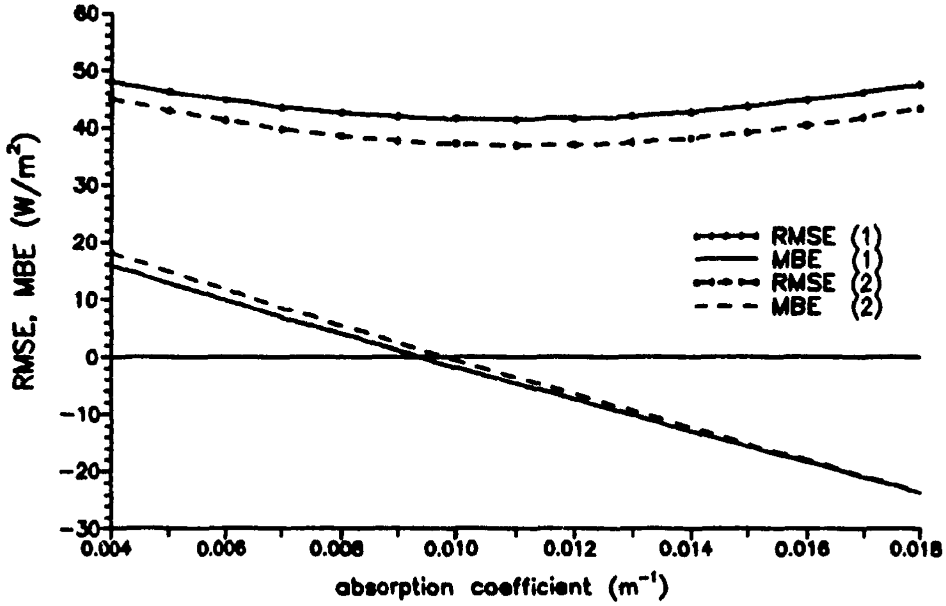

FIGURE 5.1. RMSE and MBE for varying values of the crown space absorption coefficient, calibration (1) and verification (2) data sets, site 1.

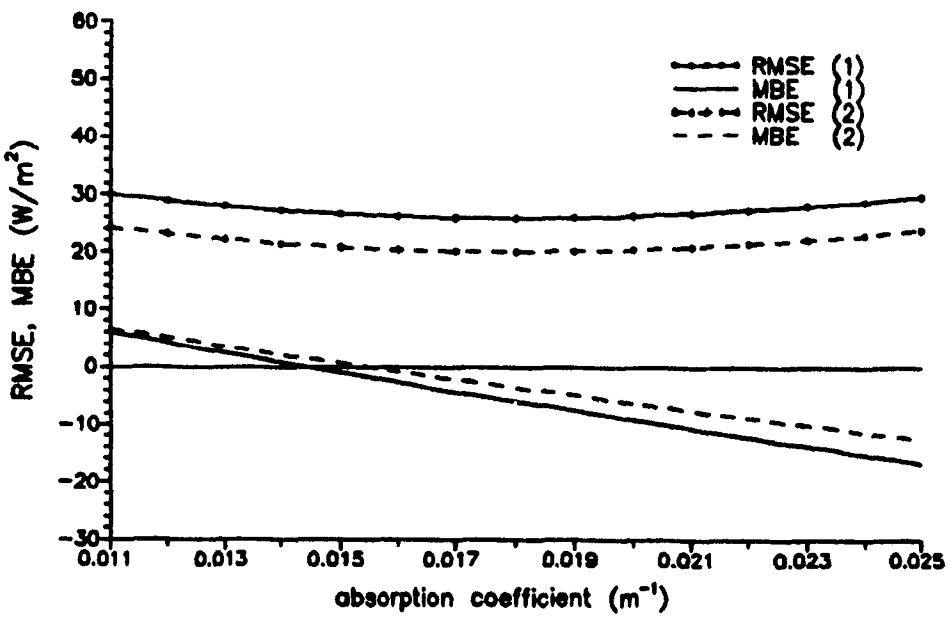

FIGURE 5.2. RMSE and MBE for varying values of the crown space absorption coefficient, calibration (1) and verification (2) data sets, site 2.

tion data set). At site 2, optimal values are 0.014 (calibration set) and 0.015 (verification set). Values of a derived through minimization of MBE, using the finite difference approach, will always agree to three decimal places with values calculated using the secant method if intervals of 0.001 m^{-1} are used for the former method. As previously mentioned, this study uses values for the crown space absorption coefficient determined by means of minimizing the root mean square error.

The difference in the absorption coefficient values for the two sites is likely due to the presence of two coniferous trees at site 2, since measured stand characteristics at the two sites do not differ greatly. This presence results in a larger value of a to compensate for the lower solar irradiance values at the surface due to added shadow. The extra shadow offered by the conifers is not included in the calculation of total shadow area since shadow area is determined from tree height and stem diameter.

5.2.2. ARITHMETIC AND QUADRATIC MEAN DIAMETER

Difficulties arise in the choice of which mean diameter to use to represent the width of a tree shadow in a non-uniform forest stand. Model theory is based on the assumption that the cylinders (representing tree stems) are uniform in height and diameter. In such a case, quadratic mean diameter (D_q) given by

$$D_q = [4B/(\pi n)]^{0.5} \qquad (5.3)$$

(Curtis, 1968) is the same as the arithmetic mean diameter, and basal area fraction may be calculated using equation 3.7 (Chapter 3). However, because of the non-linear relationship between diameter and area, when applying the model to a non-uniform forest stand, quadratic mean diameter (the diameter of a tree of mean basal area) is not equivalent to the arithmetic mean diameter; similarly, basal area fraction given by equation 3.7, using an average diameter, is not the same as the actual measured fraction. This study uses the arithmetic mean diameter since the theoretical model assumes trees of similar height and diameter, resulting in shadow area cast by a tree (before accounting for shadow overlap) equal to shadow length times diameter. For the extended model, in a non-uniform forest, average shadow area will be best estimated using the arithmetic mean diameter as a substitute for mean shadow width.

Differences resulting from using arithmetic and quadratic mean diameters are shown in Table 5.1. Although values for the crown space absorption coefficient change significantly, only minor differences are observed in the RMSE and MBE values due to the nature of the empirically derived coefficient. The most noticeable change is an increase in negative bias when using the quadratic mean diameter; this is expected since the quadratic mean diameters are larger than the arithmetic mean diameters. RMSE decreases very slightly for all cases when using the quadratic mean diameter.

Basal area, in order to be representative of the site in approximating the semicircles of shadow produced at both top and bottom of the cylinders or stems, has been calculated as the sum of the individual basal areas. A simpler approach to this problem is to calculate total area shaded in terms of length and width of shadows, using equation 3.13 to define t_e rather than equation 3.12, since it has already been assumed that basal area is negligible when compared to shadow area.

5.3. MODEL VERIFICATION

The data sets to be used for verification of the model at sites 1 and 2 were subdivided into smaller sets as functions of daily cloud cover, solar incidence angle, solar zenith angle and ratio of direct to global solar irradiance,

Table 5.1: Differences in crown space absorption coefficient and model verification statistics using arithmetic mean diameter (arith) and quadratic mean diameter (quad).

	site 1		site 2	
	arith	quad	arith	quad
mean diameter (m)	0.100	0.120	0.096	0.121
α coefficient (m^{-1})	0.011	0.017	0.018	0.025
diffuse transmissivity	0.591	0.586	0.523	0.521
calibration dataset				
RMSE (Wm^{-2})	41.3	41.0	25.9	25.3
MBE (Wm^{-2})	-4.6	-5.3	-5.9	-5.8
verification dataset				
RMSE (Wm^{-2})	36.9	36.6	20.0	19.6
MBE (Wm^{-2})	-3.6	-4.1	-3.5	-3.6

in order to test model performance under varying weather conditions and solar positions. The model was also run for the entire verification data set at each site, and for the two sites combined. It is worthwhile to look at results for the two sites combined as well as for each site individually. The combination of the two data sets will give an indication of model performance when applied to more diverse situations; this is important for studies dealing with the radiation budget of a larger area such as a watershed, comprising slopes of different degrees and aspects.

Validation statistics (root mean square error and mean bias error) are generally given both in Wm^{-2} and as percentages of the mean solar irradiance for the particular data set in question. Root mean square error (RMSE) and mean bias error (MBE) values are calculated using the following equations (Willmott, 1981):

$$RMSE = \left[(1/N) \sum_{i=1}^{N} (P_i - O_i)^2 \right]^{0.5} \tag{5.4}$$

$$MBE = (1/N) \sum_{i=1}^{N} (P_i - O_i) \tag{5.5}$$

where P is the predicted or computed value

O is the observed or measured value.

To determine RMSE and MBE as percentage values, the quantities computed using equations 5.4 and 5.5 were divided by the average observed value. This procedure for providing dimensionless values is the same as that used by Davies et al. (1984), cited in Badescu (1988). All values for RMSE and MBE are calculated for 20-minute averages of instantaneous readings of solar irradiance, unless otherwise specified.

5.3.1. MODEL PERFORMANCE TESTED AT FIELD SITES

When the model is run using the verification data set at each site, the resulting root mean square errors for the two sites are, in fact, the smallest errors possible

(Table 5.2), since the optimal RMSE-minimized absorption coefficients remain the same for calibration and verification data sets at each particular site. The mean bias errors in each case are less than the errors for the calibration data sets (see Table 5.1,). Although the average solar irradiance for the verification data set at site 1 is 2.9% higher than for the calibration data set, the absolute values of the RMSE and MBE for the verification data set are in fact lower, and the resulting percentage errors are then 15.0% and 1.7% lower for the RMSE and MBE, respectively, than for the calibration data set. At site 2 the average solar irradiance for the verification data set is 14.2% less than for the calibration data set, while the RMSE and MBE are 22.9% and 40.4% less, respectively, for the verification data set than for the calibration data set. These results attest to the overall good performance of the model concerning its application to the verification data sets. When data from the two sites are combined the overall percentage errors, based on 20-minute averages of instantaneous values, are 15.5% (23.7 Wm^{-2}) for the RMSE and -1.9% (-3.5 Wm^{-2}) for the MBE. Appendix C shows time-series of predicted and observed solar irradiance values for all days included in the verification data set.

On sunny days a recurring discrepancy is generally noted at site 1 between the hours of 1120 and 1220 LST when the observed solar irradiance values drop considerably lower than the predicted values, e.g., 10 March and 14 April (Figure 5.3). Values of global radiation above the canopy show no tendency toward lower values at these times, and the discrepant values may be attributable to a greater number of solarimeters in the shade for this period than theoretically should be, a result of the fixed-solarimeter sampling strategy and

Table 5.2: RMSE and MBE for verification datasets in Wm^{-2} and as percent values (RMSE%, MBE%). Avg (Wm^{-2}) is the average solar irradiance for the data set; n refers to the number of data points.

	site 1	site 2	sites 1&2
RMSE	36.9	20.0	28.7
RMSE%	13.2	18.0	15.5
MBE	-3.6	-3.5	-3.5
MBE%	-1.3	-3.2	-1.9
avg	279.6	111.1	185.7
n	303	381	684

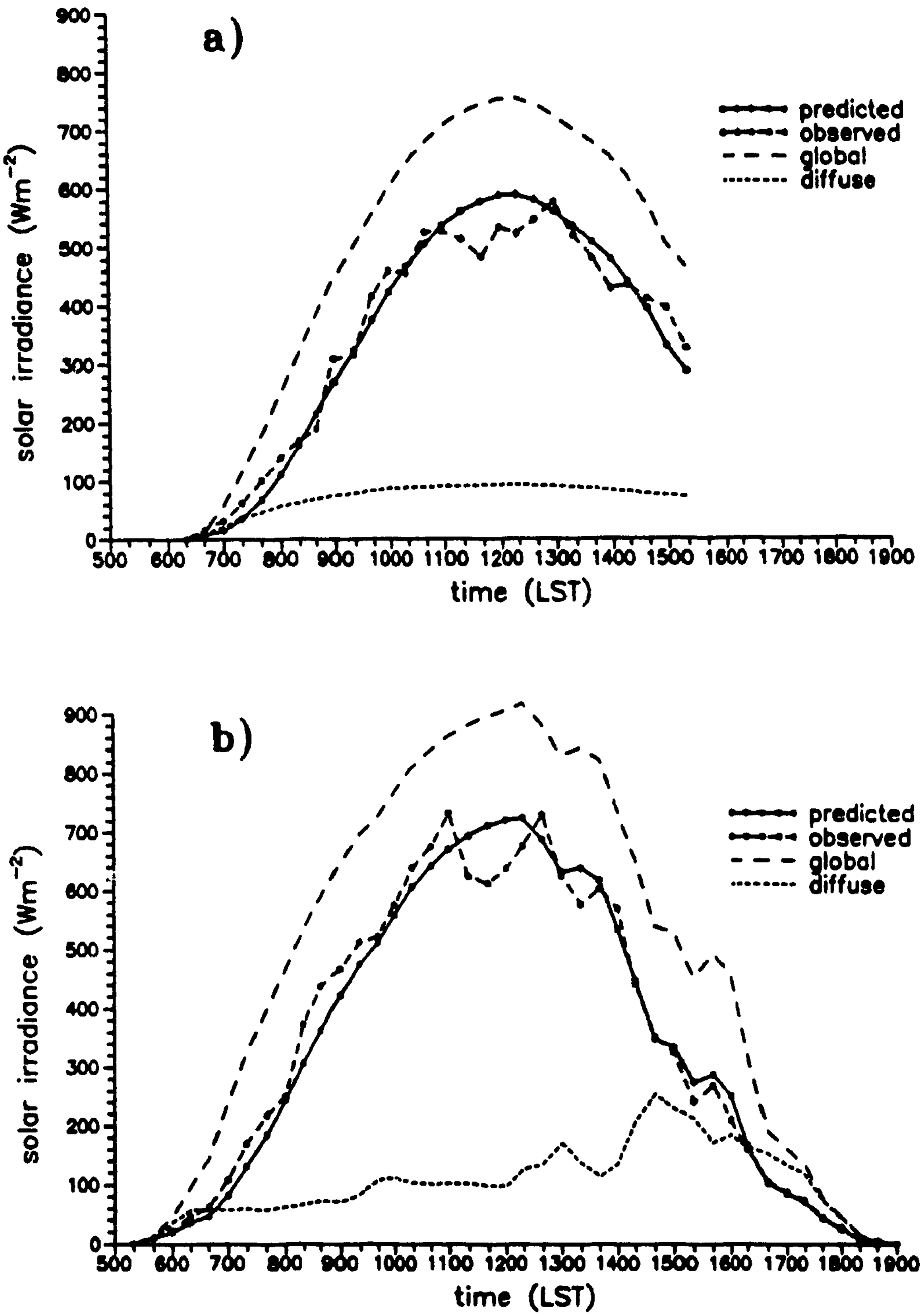

FIGURE 5.3. Time series of solar irradiance values showing discrepancy between predicted and observed values from 1120 -1220 LST: a) 10 March and b) 14 April. Global and diffuse refer to solar irradiance above the canopy. Solar irradiance values after 1520 LST have been eliminated because of unsatisfactory adjustment of the shadow band.

limited number of instruments. (See also Appendix B, Julian days 68, 70, 72 and 74 from the calibration data set, where the discrepancy is evident when comparing global radiation above the canopy with the observed values of solar irradiance at the forest floor.)

5.3.2. DATA SUBSETS AS A FUNCTION OF DAILY SKY CONDITION

Three simple types of daily cloud cover condition have been defined for this study: overcast (approximately 8/10 to 10/10 cloud cover), partially cloudy (3/10 to 7/10 cloud cover), and sunny sky conditions (0/10 to 2/10 cloud cover). Average cloud cover conditions for each day have been determined from the traces of global and diffuse radiation above the canopy, and from records of meteorological data at the research station (cloud cover at 800 and 1600 LST, times and quantity of precipitation). Table 5.3 shows the effects of different cloud cover conditions upon model performance as measured by RMSE and MBE.

The large error associated with partial cloud cover at site 1 is due primarily to the distance between the tower and the field sites, resulting at times in clouds that obscure beam irradiance at the tower while not at the slopes, and vice versa. The most severe example of such a case during the data collection period may be seen on the time-series graph for 14 March, Julian day 73 (Figure 5.4). On this otherwise sunny day it seems that a large cloud or small frontal system passed over the area, obscuring beam irradiance at the tower site about 20 minutes before doing so at the field site, then similarly beginning to clear at the tower site 20 minutes earlier than at the field site. This situation involves a total time of slightly over one hour, and results in four very poor predictions for solar irradiance at site 1 based on the measured irradiance at the tower site.

Although it may be desirable to eliminate such data from the analysis, this was not done because of the difficulty

Table 5.3: RMSE and MBE as a function of daily sky condition. Values are given in Wm^{-2} (RMSE, MBE, avg), and as percentages (RMSE%, MBE%) of the average solar irradiance for the data set (avg); n refers to the number of data points.

daily sky condition		site 1	site 2	sites 1&2
sunny:	RMSE	37.5	31.0	34.8
	RMSE%	10.3	16.5	12.2
	MBE	-2.0	-11.2	-6.1
	MBE%	-0.6	-6.0	-2.1
	avg	364.0	187.4	285.9
	n	96	76	172
partial cloud:	RMSE	44.2	16.2	32.6
	RMSE%	16.5	13.0	17.0
	MBE	-1.0	-2.0	-1.5
	MBE%	-0.4	-1.6	-0.8
	avg	268.3	124.6	192.2
	n	135	152	287
overcast:	RMSE	11.8	13.4	12.9
	RMSE%	6.3	22.4	12.8
	MBE	-8.9	-0.1	-2.9
	MBE%	-4.7	-0.2	-2.9
	avg	188.4	59.8	101.0
	n	72	153	225

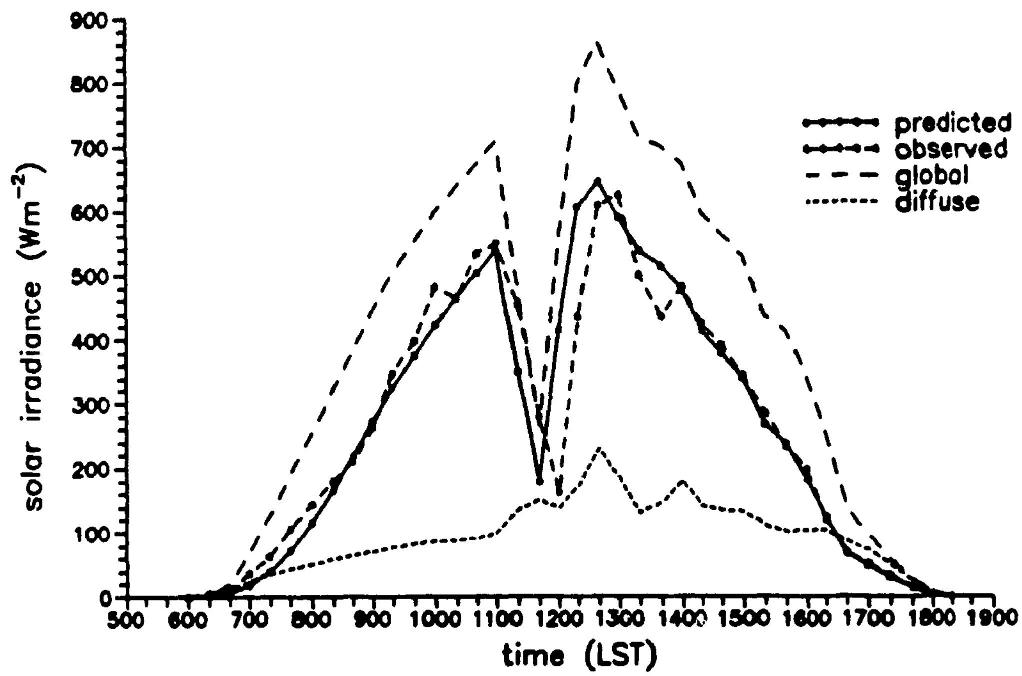

FIGURE 5.4. Time series of solar irradiance values for 14 March, showing predicted and observed values at the surface, and emphasizing the error attributable to the distance between the tower and field sites. Global and diffuse refer to solar irradiance above the canopy.

entailed in evaluating less severe cases from the data. Furthermore, for application of the model to larger areas or entire watersheds, predictions of solar irradiance under partly cloudy sky conditions based upon measurements at one point will always entail similar situations for areas which extend some distance beyond this observation point. Howevcr, as an exercise, the model was run for day 73 both with and without the four 20-minute periods which may be considered anomalous errors for this observational study. When these four data points were eliminated RMSE decreased from 61.6 Wm^{-2} to 25.1 Wm^{-2} (21.7% to 9.0%). When the same four data points were eliminated from the subset for partially cloudy conditions, RMSE dropped from 44.2 Wm^{-2} to 33.9 Wm^{-2} (16.5% to 12.7%).

The large error (RMSE) for cloudy conditions at site 2 is due primarily to one day, Julian day 93 (3 April), for which predicted values were consistently higher than observed values (Figure 5.5), contrary to the usual negative bias for low solar irradiance values. This may be a result of partial clearing of the sky which was concentrated near the tower site and not at the slope site (Figure 5.5, 940-1040 and 1200-1300 LST). A further explanation for some of the discrepancy might be the elimination of data from one solarimeter for Julian days 92, 93 and 94 because of condensation within the outer of the two hemispherical glass domes. This solarimeter was consistently measuring solar irradiance values higher than the average (especially between 1120-1500 LST); subsequently, lack of data from this instrument would result in lower observed averages relative to other days. However, data for Julian days 92 and 94 do not reveal similar discrepancies, even though average solar irradiance values for these two days are slightly higher (see Appendix C).

The scattergrams of Figures 5.6 and 5.7 show predicted vs. observed solar irradiance values as a function of daily sky condition for sites 1 and 2, respectively. There is an evident increase in error associated with an increase in

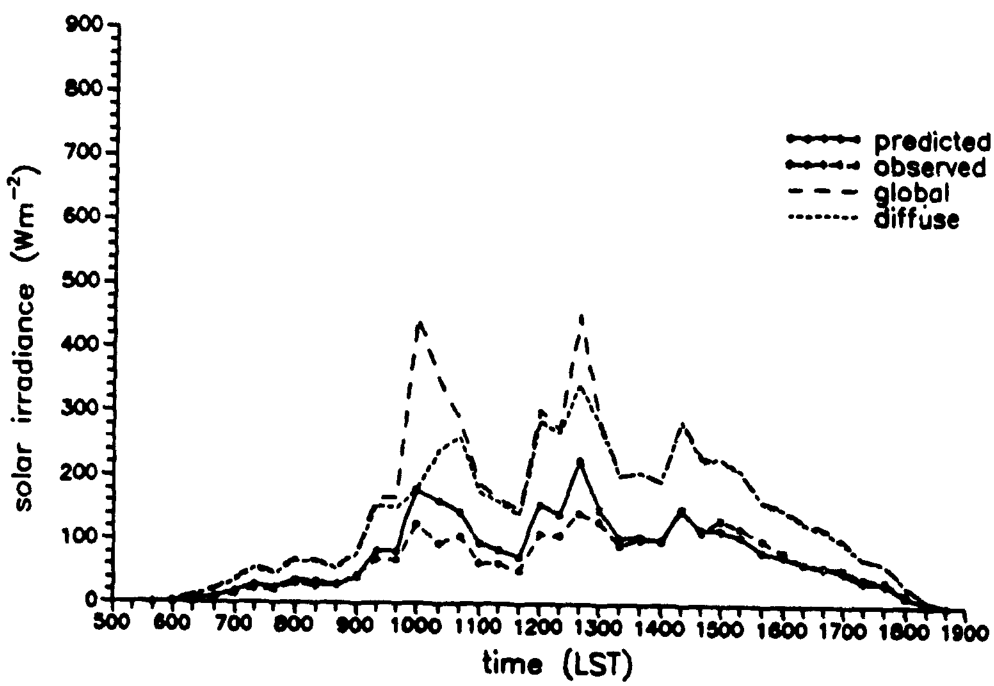

FIGURE 5.5. Time series of solar irradiance values for 3 April, emphasizing predicted values that are consistently higher than observed values. Global and diffuse refer to solar irradiance above the canopy.

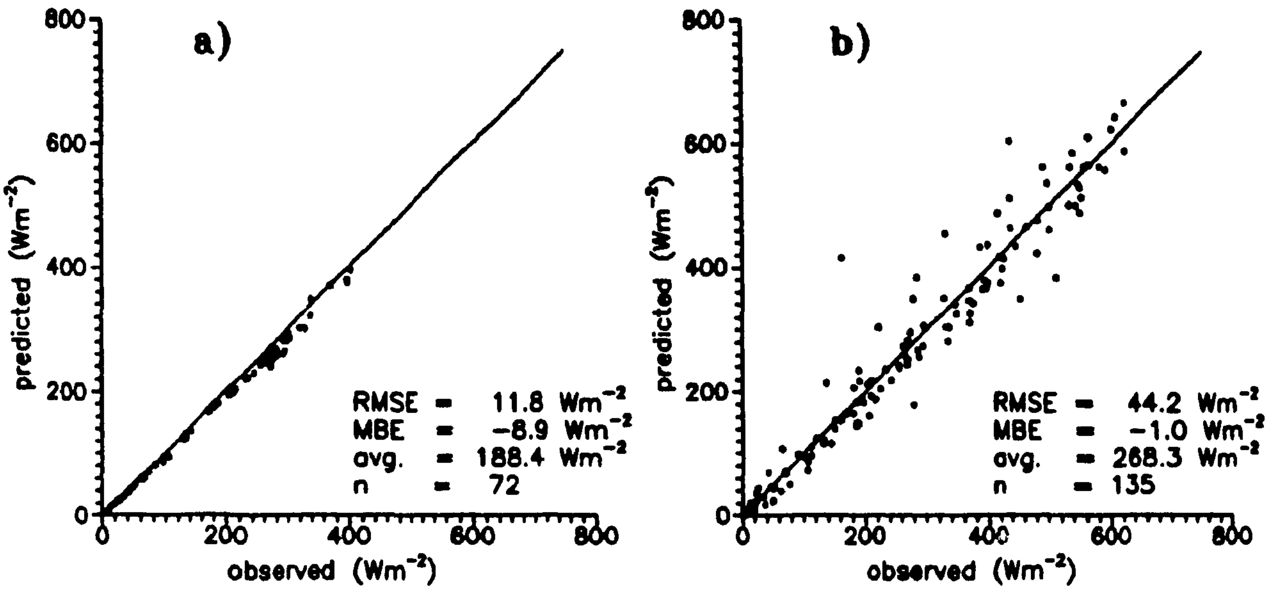

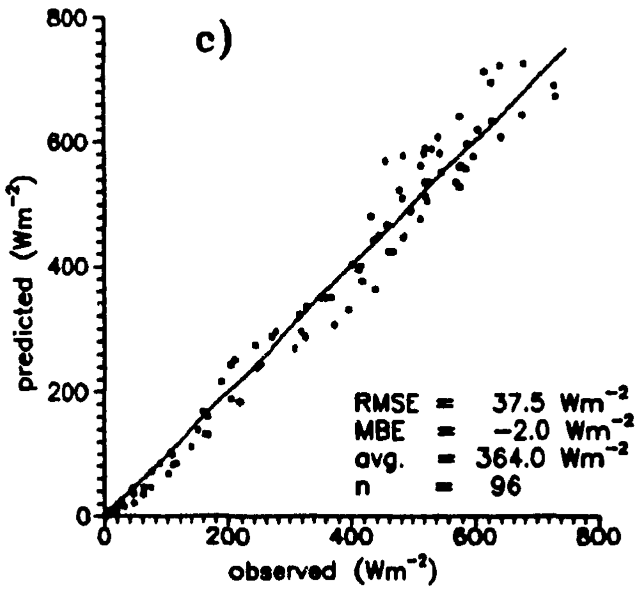

FIGURE 5.6. Predicted vs. observed solar irradiance values as a function of daily sky condition, site 1: a) overcast, b) partial cloud and c) sunny sky conditions. avg. refers to the average solar irradiance for the particular data set; n is the number of data points. Scattergrams are fitted with 1:1 ratio lines.

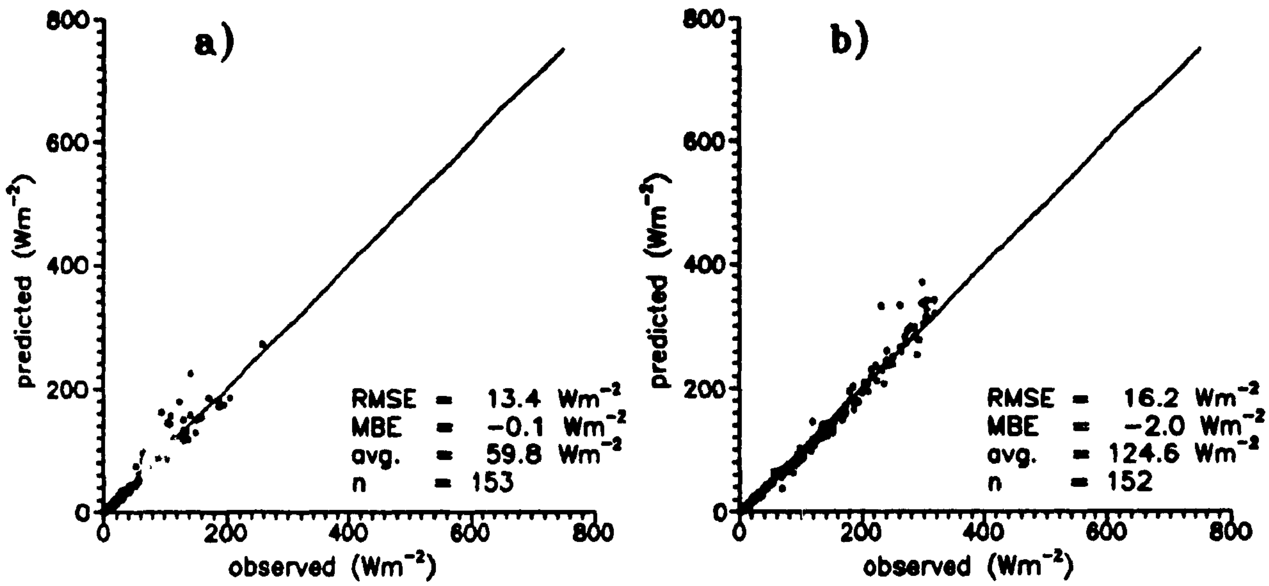

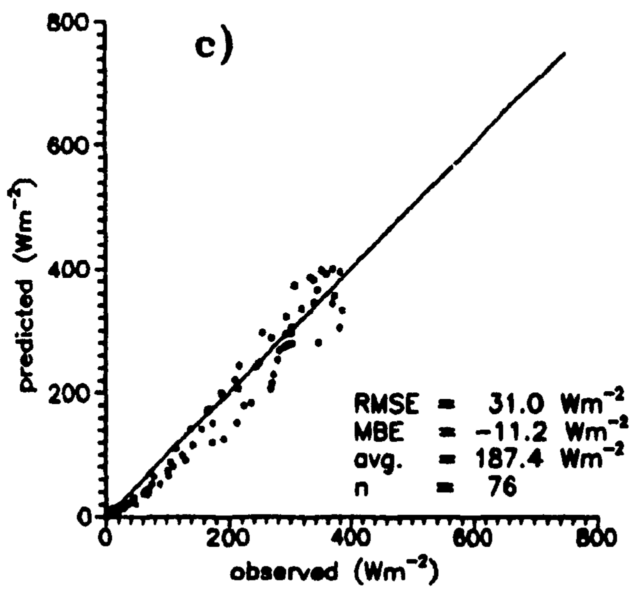

FIGURE 5.7. Predicted vs. observed solar irradiance values as a function of daily sky condition, site 2: a) overcast, b) partial cloud and c) sunny sky conditions. avg., n, and ratio lines are as in Figure 5.6.

solar irradiance values. Furthermore, there is an increase in the variability in the error encountered when considering sunny sky conditions or partial cloud conditions as opposed to overcast sky conditions. The greatest variability in the error appears for partial cloud conditions, primarily because of the aforementioned problem associated with the distance between the tower and the field sites, reflecting the variability at the surface inherent in partially sunny sky conditions with cloud movement. However, because of the great variability in the error associated with such conditions, MBE is generally very low for partial cloud conditions. For sunny sky conditions the model slightly over- predicts at high solar irradiance values, and generally under-predicts at lower irradiance values. For overcast sky conditions the model tends to under-predict very slightly at all times, if the anomalous values of Julian day 93 are disregarded.

The tendency for over-prediction at high solar irradiance values and under-prediction at lower values may be due in part to the assumption that basal area is negligible. At high sun angle (resulting in high irradiance values on sunny and partially sunny days), basal area may account for a significant portion of the total shadow area, whereas at low sun angle basal area accounts for a much smaller proportion of the total shadow. The errors associated with over- and under-prediction may also be due to inhomogeneity of the canopy, i.e., a crown space which is not an isotropic absorber of solar irradiance. In such a case, different zenith angles would require different values for the crown space absorption coefficient. Thus, errors resulting from the assumption of a homogeneous crown space may be related to errors associated with high and low solar irradiance values because of the generally negative relationship between zenith angle and solar irradiance.

Table 5.4 shows a comparison between the model error and the observed error. Observed values of solar irradiance

Table 5.4: Comparison between observed error, RMSE%(obs), and model error, RMSE%(mod), according to daily sky condition, sites 1 and 2 combined.

Data set	RMSE%	RMSE%(obs)	RMSE%(mod)
total set	15.5	6.6	14.0
overcast	12.8	2.6	12.5
partial cloud	17.0	6.4	15.7
sunny	12.2	8.9	8.3

are not without error, due to both instrument and sampling error. Therefore, an attempt has been made to estimate modelling error as separate from sampling error. The total calculated error (RMSE), based upon predicted and observed values, may be considered to comprise model error, based upon the difference between model and true values, and observed or sample error, based upon observed and true values. If model error and observed error are random and uncorrelated, and if predicted and/or observed values are unbiased, then an estimate of the modelling error, RMSE%(mod), is given by:

$$RMSE\%(mod) = [(RMSE\%)^2 - (RMSE\%(obs))^2]^{0.5} \qquad (5.6)$$

where RMSE%(obs) is the error in the observed values, estimated by the standard error (SE) as a percentage value. The interesting point to note is that the large sampling error associated with the direct beam component of solar radiation results in the total error being approximately equally divided between sampling and modelling error for sunny sky conditions. In contrast, the low sampling error associated with overcast sky conditions means that most of the error for such conditions is related to modelling error. This may result from the calibration procedure for both instruments and model. Instrument calibration involves data taken from mostly sunny sky conditions; calibration of the model through the crown space absorption coefficient tends to favor minimizing error for high solar irradiance values.

Sunny sky conditions, then, result in large sampling error due to the changing shadows, but relatively small modelling error. Partial cloud sky conditions result in large modelling error due to the spatial and temporal variability associated with partial cloud sky conditions, and moderate modelling error. Finally, overcast sky conditions result in very small sampling error, but large modelling error (relative error) because of instrument and model calibration. Although the distinction between total error and model error is not made in the following discussions concerning data subsets, it should be kept in mind that the total error is a combination of model error and observed error.

5.3.3. DATA SUBSETS AS A FUNCTION OF SOLAR ZENITH ANGLE AND SOLAR INCIDENCE ANGLE

The verification data sets were also divided, irrespective of cloud cover, into subsets as functions of solar incidence angle and solar zenith angle: 25-45°, 45-65° and 65-90° intervals, as well as 10° intervals; the appropriate angles were determined for the mid-point of each 20-minute averaging period. For the following discussion, data from sites 1 and 2 have been combined since similar trends were observed at each site individually (Tables 5.5 and 5.6). The scattergrams of Figure 5.8 show the increasing variability in the error associated with decreasing incidence angle. At large incidence angle the path length of the solar beam through the crown space is longer, solar irradiance values are lower (although not necessarily true for surfaces of greater slope degree), and more of the solar irradiance reaching the forest floor is diffuse, than for small incidence angle. At small incidence angle, the decrease in shadow area due to the greater amount of direct solar irradiance reaching the forest floor results in greater variability in the error. The diagrams also show a progressive tendency from under-prediction to over-prediction with decreasing incidence angle. This is probably a result of the under- and over-prediction associated with low and high solar irradiance values, as discussed in the previous section, since low sun angle is equivalent to large zenith angle and, for slopes of minor inclination, is also equivalent to large incidence angle.

The scattergrams of Figure 5.9, using data sets determined as a function of solar zenith angle rather than incidence angle, show results very similar to those of Figure 5.8. For surfaces of small slope degree, incidence angle approaches

Table 5.5: RMSE and MBE as a function of solar incidence angle. Values are given in Wm^{-2} (RMSE, MBE, avg) and as percentages (RMSE%, MBE%) of the average solar irradiance for the data set (avg); n refers to the number of data points. There are no values for incidence angle less than 45° for the north-facing slope.

incidence angle		site 1	site2	sites 1&2
65° - 90°	RMSE	14.9	13.3	13.8
	RMSE%	23.3	24.8	24.2
	MBE	-8.4	-6.5	-7.1
	MBE%	-13.1	-12.1	-12.5
	avg	63.9	53.6	57.0
	n	83	172	255
45° - 65°	RMSE	30.0	23.6	25.9
	RMSE%	11.0	14.1	12.8
	MBE	-6.0	-0.3	-2.2
	MBE%	-2.2	-0.2	-1.1
	avg	273.2	167.0	202.4
	n	99	198	297
25° - 45°:	RMSE	49.0	---	49.0
	RMSE%	11.3	---	11.3
	MBE	2.6	---	2.6
	MBE%	0.6	---	0.6
	avg	432.9	---	432.9
	n	109	---	109

Table 5.6: RMSE and MBE as a function of solar zenith angle. Values are given in Wm^{-2} (RMSE, MBE, avg) and as percentages (RMSE%, MBE%) of the average solar irradiance for the data set (avg); n refers to the number of data points.

zenith angle		site 1	site2	sites 1&2
65° - 90°	RMSE	18.1	9.6	13.9
	RMSE%	19.3	25.8	22.7
	MBE	-6.6	-4.9	-5.7
	MBE%	-7.0	-13.2	-9.3
	avg	94.0	37.2	61.2
	sample	106	144	250
45° - 65°	RMSE	44.1	22.2	35.0
	RMSE%	11.9	15.9	13.7
	MBE	-0.5	-6.1	-3.3
	MBE%	-0.1	-4.4	-1.3
	avg	370.9	139.8	256.4
	n	159	156	315
25° - 45°:	RMSE	42.1	25.4	31.7
	RMSE%	9.9	13.1	11.8
	MBE	-4.2	6.3	2.9
	MBE%	-1.0	3.2	1.1
	avg	427.1	194.3	269.2
	n	37	78	115

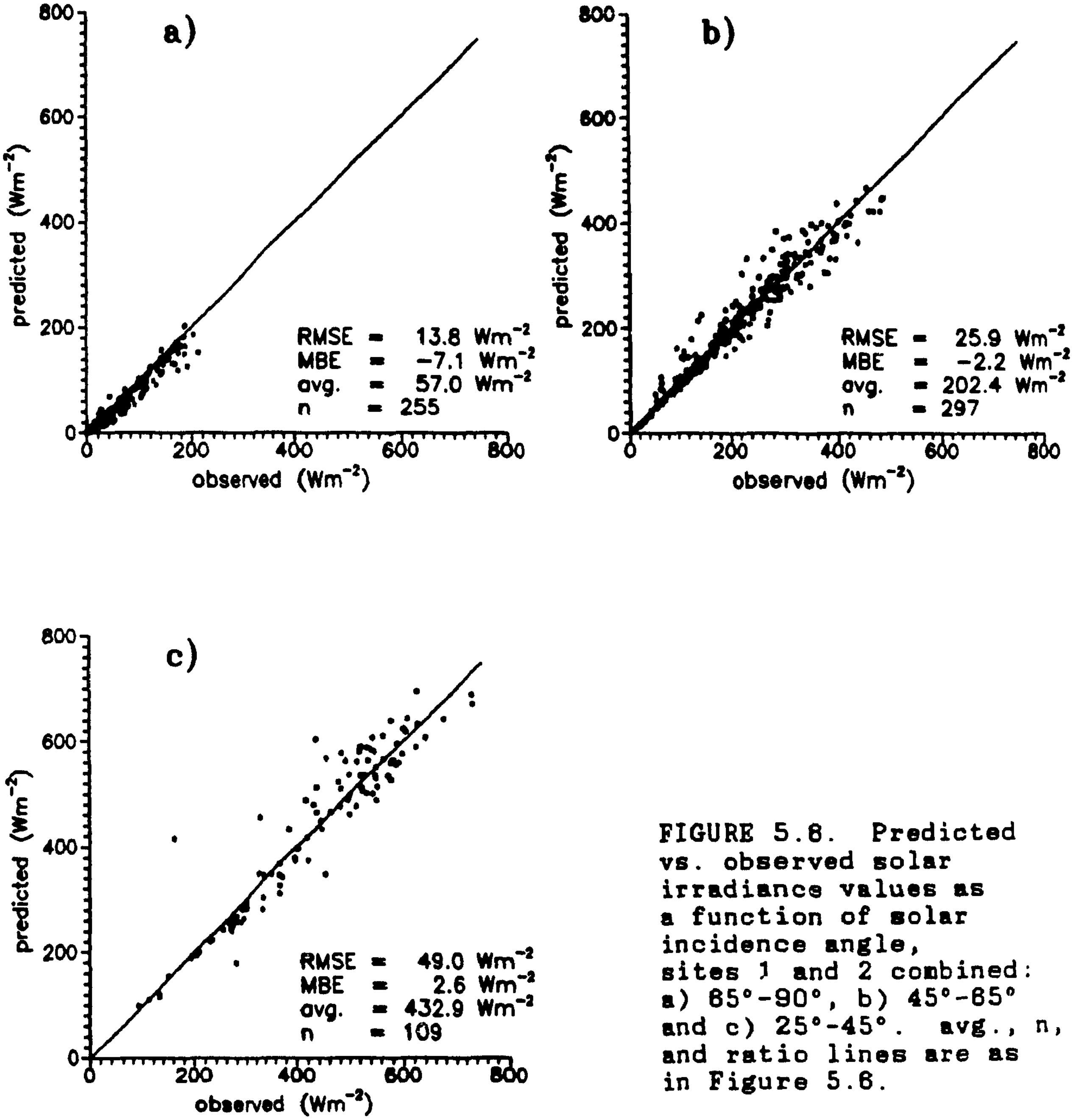

FIGURE 5.8. Predicted vs. observed solar irradiance values as a function of solar incidence angle, sites 1 and 2 combined: a) 65°-90°, b) 45°-65° and c) 25°-45°. avg., n, and ratio lines are as in Figure 5.6.

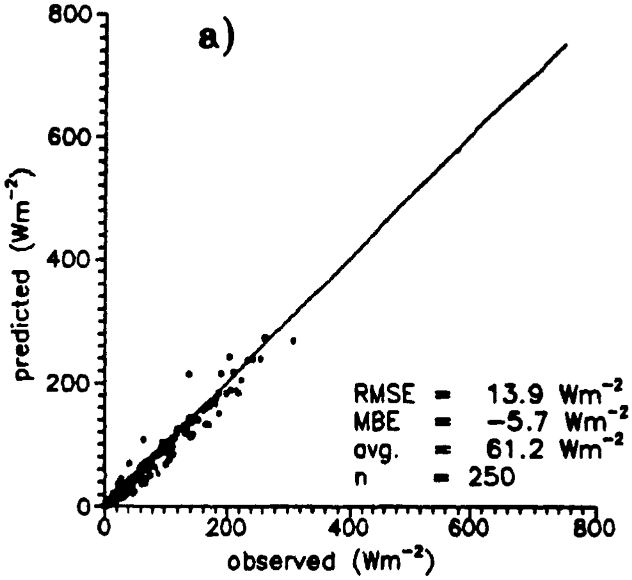

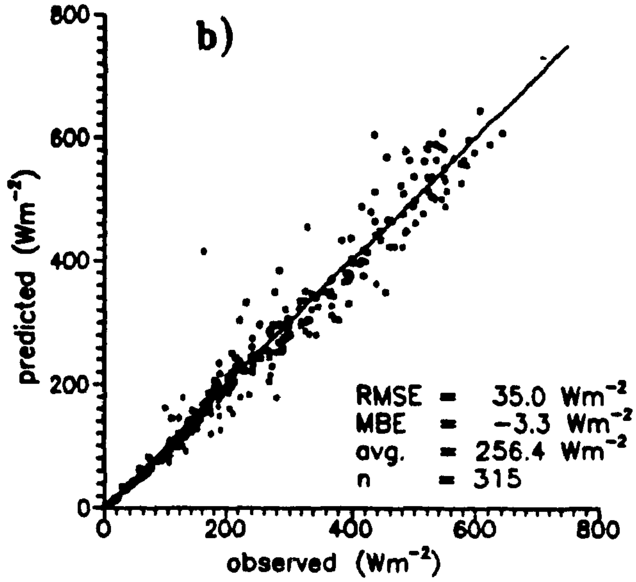

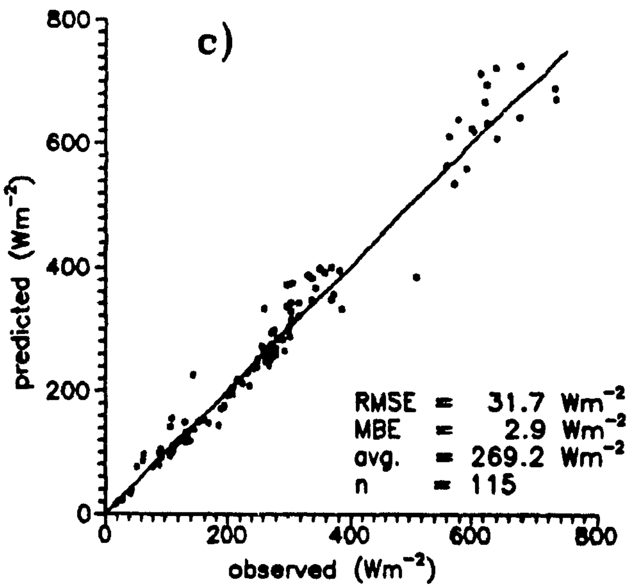

FIGURE 5.9. Predicted vs. observed solar irradiance values as a function of solar zenith angle, sites 1 & 2 combined: a) 65°-90°, b) 45°-65° and c) 25°-45°. avg., n, and ratio lines are as in Figure 5.6.

zenith angle and similar results are expected. Predicted minus observed solar irradiance values increase in variability significantly from large to medium zenith angle. At large zenith angles (low solar elevation) more of the solar irradiance reaching the forest floor is diffuse because of the increased area in shadow, and not necessarily because of increased path length through the crown space; theoretically, for a steep slope (and subsequent steeply sloping crown space) zero zenith angle could result in longer path length than for 90° zenith angle. For sites of greater slope degree, then, one expects an increase in variability with decreasing incidence and zenith angles associated with the decreasing path length and shadow area. However, between minimum incidence angle and minimum zenith angle, the case arrives for which path length increases while shadow area decreases, resulting in a tendency for both increasing and decreasing variability. This may be slightly evident in Figure 5.9, diagrams b) and c), where the variability in the error decreases with decreasing zenith angle, while for some of the data points solar incidence angle may be increasing. The decrease in RMSE is also due in part to the inclusion of the anomalous errors of Julian day 73 in the data set for zenith angle between 45 and 65 degrees.

The root mean square and mean bias errors have been calculated for 10° intervals for both incidence angle and zenith angle. Results are shown in Figure 5.10 in Wm^{-2} and as percentages of the average solar irradiance for the particular interval. Although RMSE values are high for incidence or zenith angles less than 60°, the percent error is not large; MBE values are very low for the same intervals. For incidence or zenith angles greater than 70° both the RMSE and MBE, as percentage errors, become large. However, because of low solar irradiance values at large incidence or zenith angle, the actual error over time is not large. Root mean square error for both sites combined is approximately 15% of the

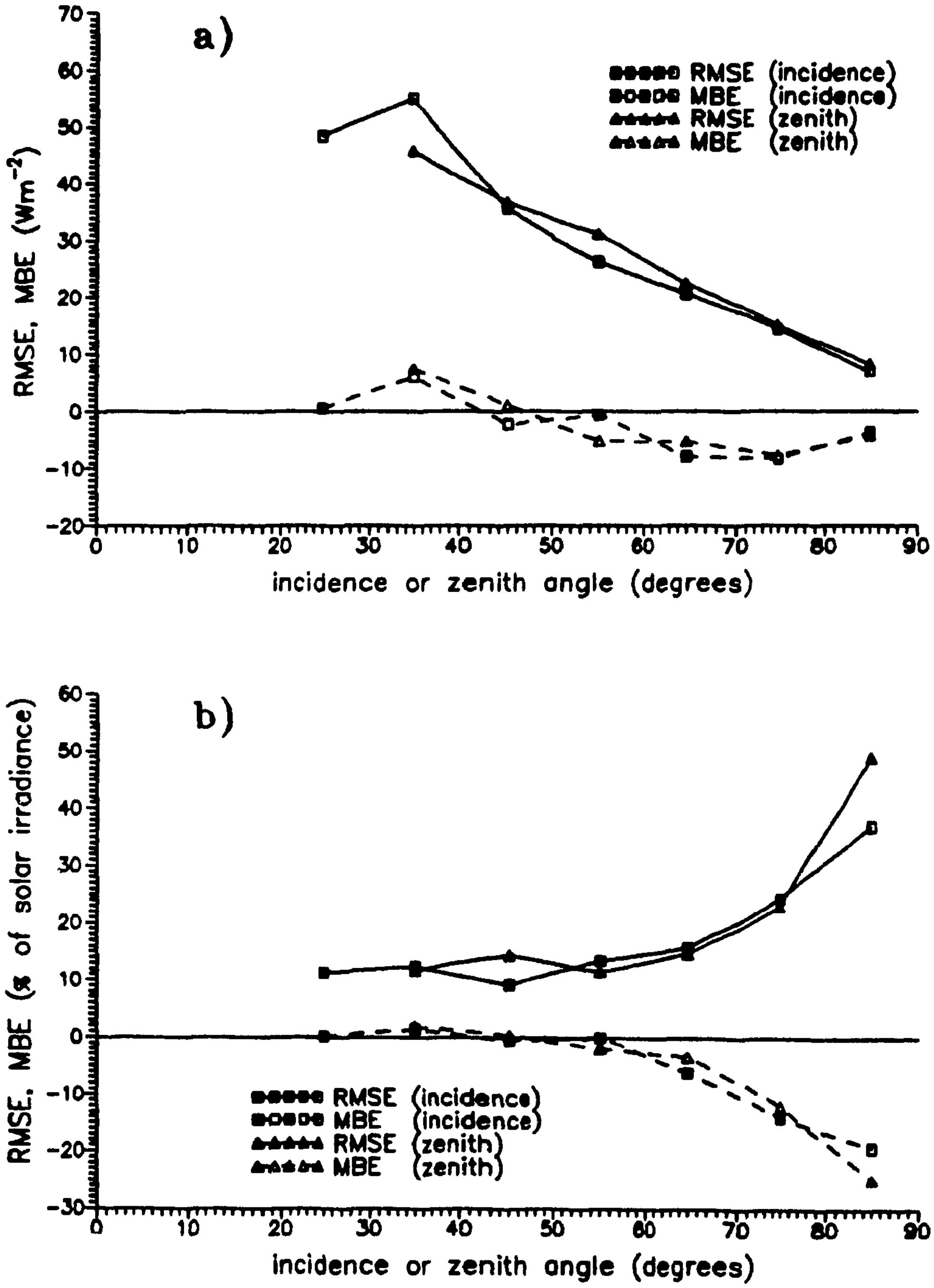

FIGURE 5.10. RMSE and MBE vs. solar incidence angle and solar zenith angle in 10° intervals, sites 1 and 2 combined: a) in Wm^{-2} and b) as percentages of average solar irradiance values. Data points are depicted at the mid-point of the 10° interval.

average solar irradiance, and MBE is only -1.9% of the solar irradiance.

5.3.4. DATA SETS AS A FUNCTION OF THE RATIO OF DIRECT TO GLOBAL SOLAR IRRADIANCE

Except for during periods of large zenith angle, greater values of solar irradiance are generally positively related to the ratio of direct to global solar irradiance. The model was therefore applied to data sets determined as a function of this ratio in 20% intervals, in order to analyze model performance for this criterion. Results are shown in Figure 5.11 for sites 1 and 2. At both sites, RMSE (in Wm^{-2}) increases with increasing ratio, but remains relatively constant as a percentage value. Mean bias error does not seem to follow any specific trend, but remains within a range of ±7 percent.

When validation statistics were calculated for data grouped into 10% ratio intervals, the results were very erratic for both RMSE and MBE, although the overall trend of increasing RMSE with increasing ratio was evident. For 33% ratio intervals, the results were very much smoothed, and depicted even more dramatically the trend for constant RMSE percentages and low MBE values. The increase in RMSE with increasing ratio of direct to global solar radiation is similar to the increase in RMSE with decreasing incidence or zenith angle. High values of global solar radiation generally imply high values of direct solar radiation and high ratios of direct to global radiation, which in turn generally occur at smaller incidence or zenith angle.

5.4. SENSITIVITY ANALYSIS

Sensitivity analysis was carried out to determine which parameters affected model performance most severely. A particular parameter was allowed to vary over a range of

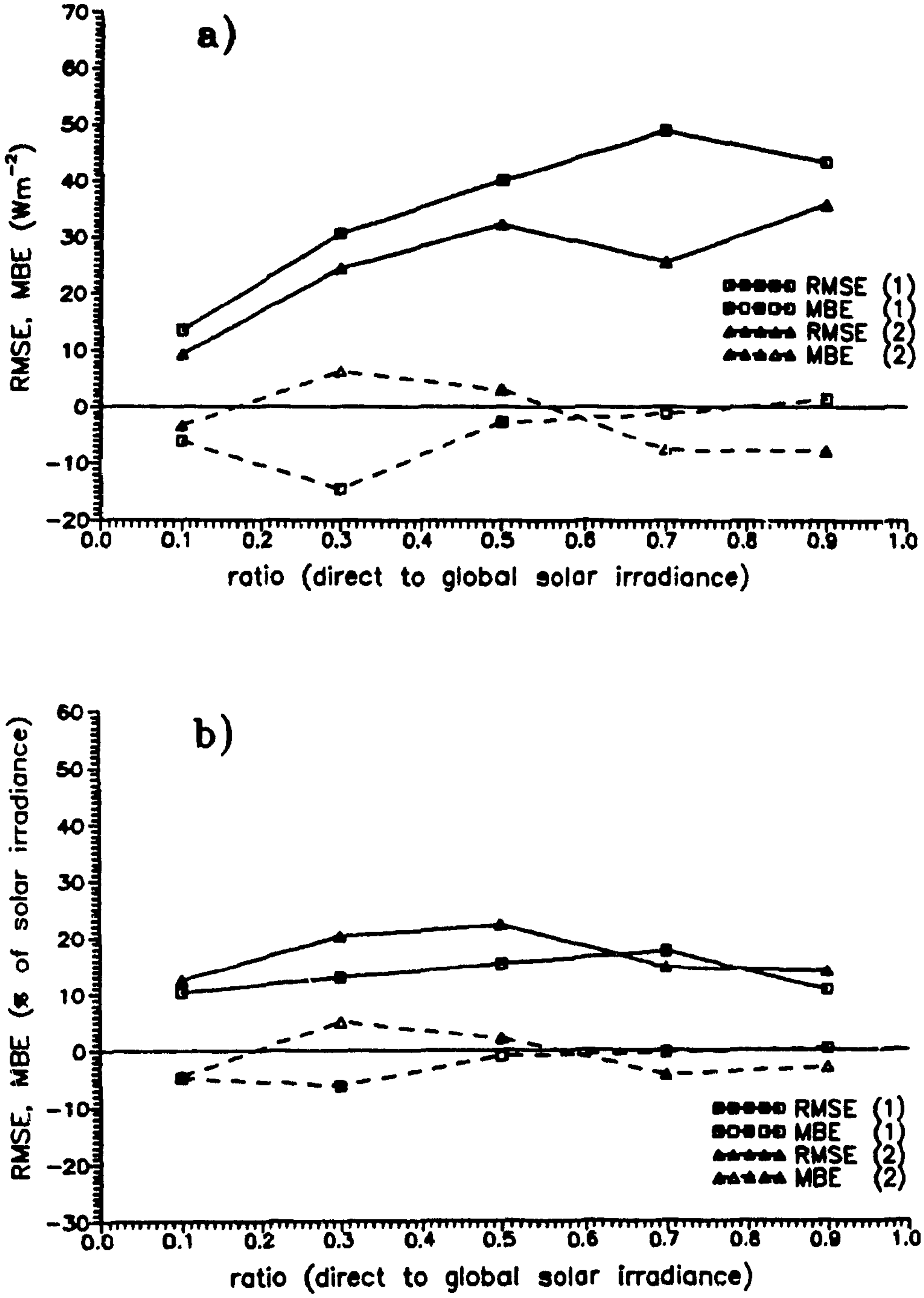

FIGURE 5.11. RMSE and MBE vs. ratio of direct to global solar irradiance in 20% intervals, sites 1 (1) and 2 (2): a) in Wm^{-2} and b) as percentages of average solar irradiance values. Data points are depicted at the mid-point of the 20% interval.

values while RMSE and MBE were calculated for each value, for both the calibration and verification data sets. Because of similar results for several of the cases, the parameters have been divided into two groups for the following discussion: stand characteristics (tree height, mean arithmetic diameter, basal area fraction and stand density) and site characteristics (slope degree and slope aspect).

5.4.1. STAND CHARACTERISTICS

Stand parameters were allowed to vary ±10% from the values given in Table 4.1 (Chapter 4). The range of values used is equivalent to errors of greater than ±1.5 m for tree height, ±0.010 m for mean diameter, ±0.00036 for basal area fraction, and ±315 trees ha^{-1} for stand density. The sensitivity of the model to basal area fraction was tested because of its use as a measured input value for the original Federer model; stand density and arithmetic mean diameter are used as input to the extended model.

Several trends are evident in the results, shown in Figures 5.12 through 5.15. These figures show results for both the south- and north-facing sites, and for both the calibration and verification data sets. Of the four parameters tested, the model is most sensitive to tree height with respect to both RMSE and MBE (Figure 5.12). However, for the ranges tested RMSE shows very little deviation from the minimum value for variations in mean diameter, basal area fraction and stand density (Figures 5.13, 5.14 and 5.15, respectively). Maximum increases in RMSE at either site for 10% changes in parameter values are as follows: 4.6% for a decrease in basal area fraction, 4.5% for an increase in mean diameter, and 3.0% for a decrease in stand density. Deviations in tree height result in more dramatic increases in RMSE. In the worst case, a decrease of 10% in tree height entails an increase of 6.1% in the RMSE. A similar decrease in tree height at site 2 results in an increase in the RMSE of approximately 7.0%.

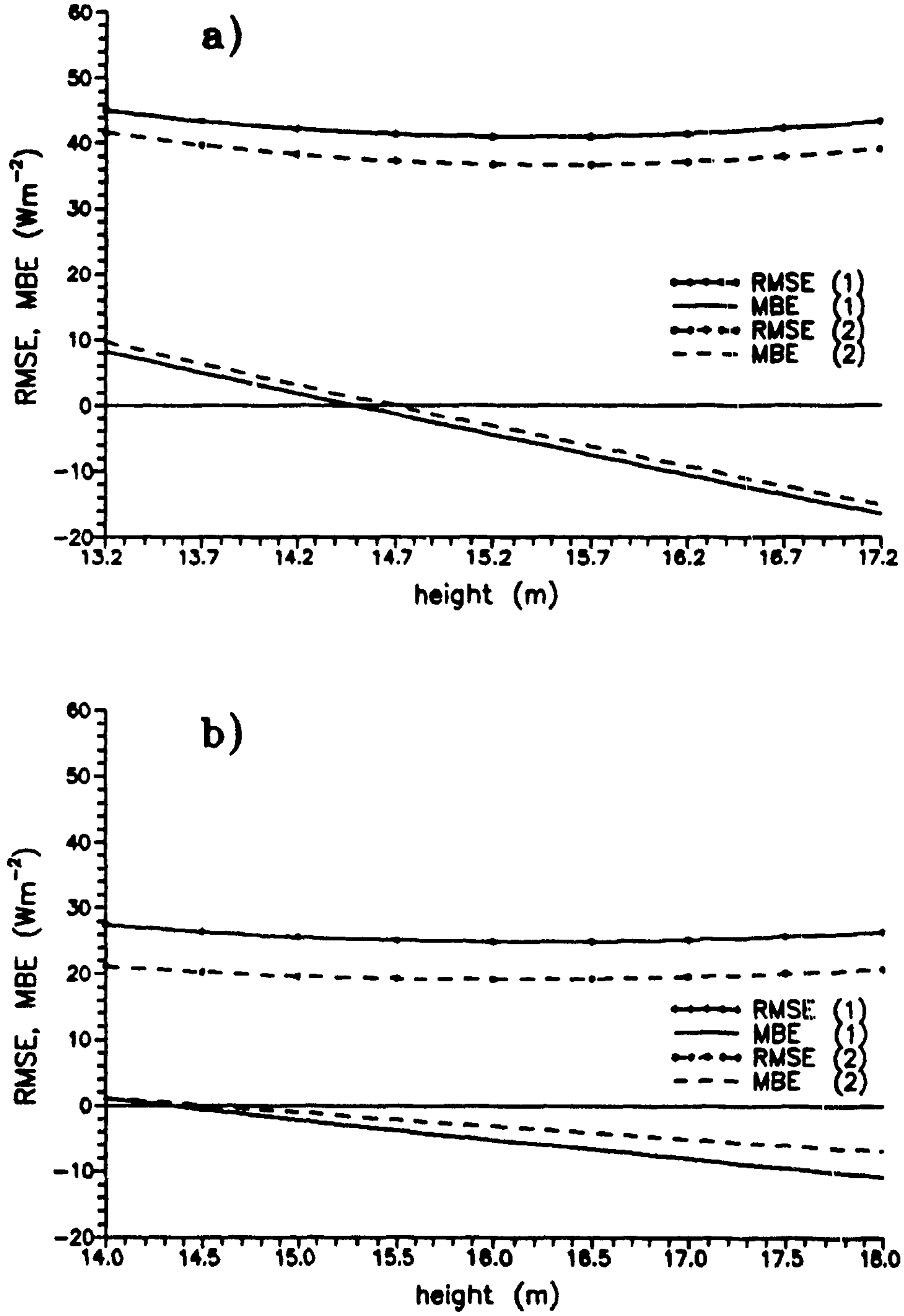

FIGURE 5.12. RMSE and MBE vs. tree height, for calibration (1) and verification (2) data sets: a) site 1 and b) site 2.

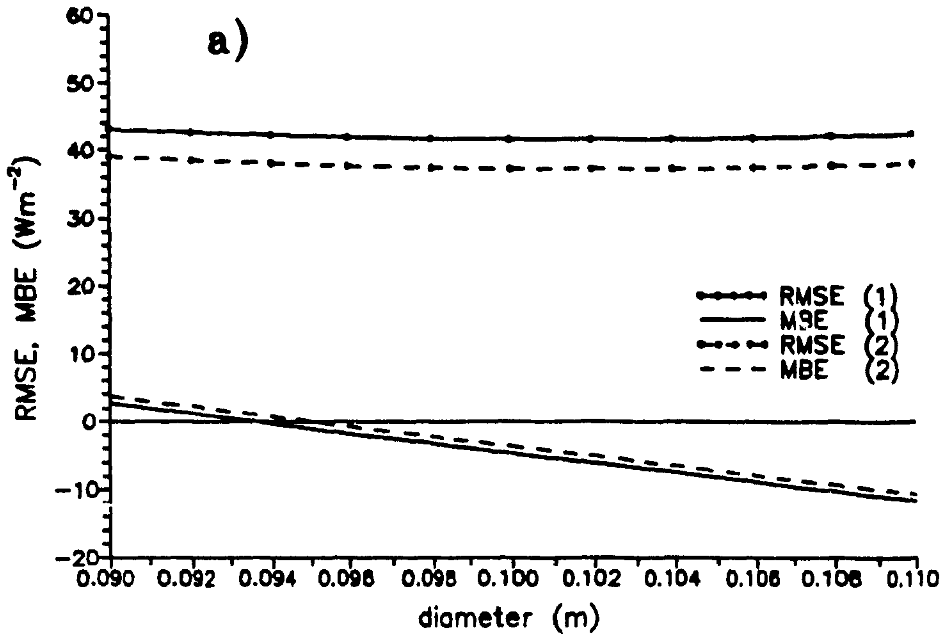

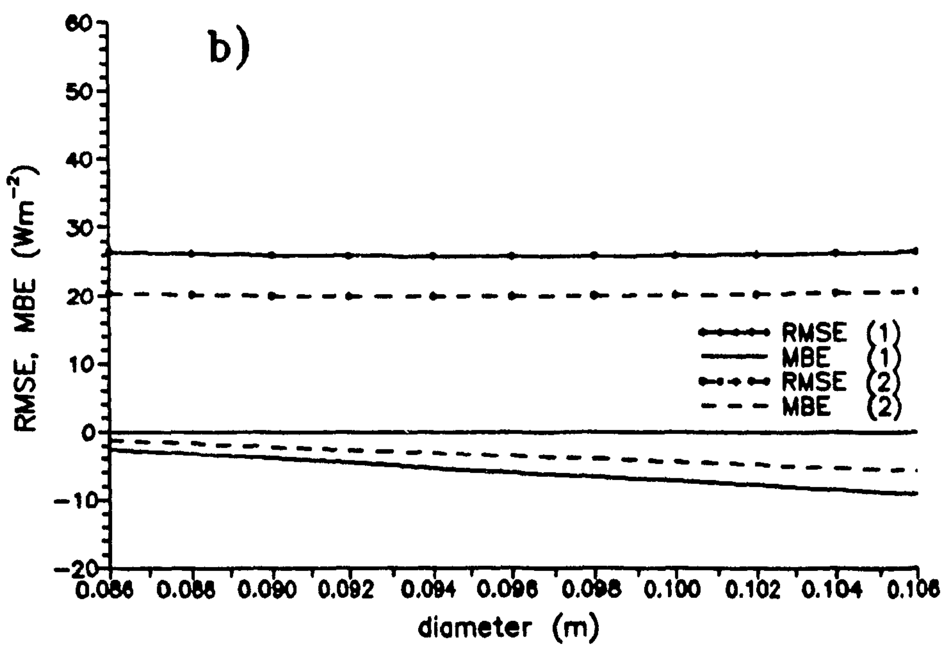

FIGURE 5.13. RMSE and MBE vs. arithmetic mean diameter, for calibration (1) and verification (2) data sets: a) site 1 and b) site 2.

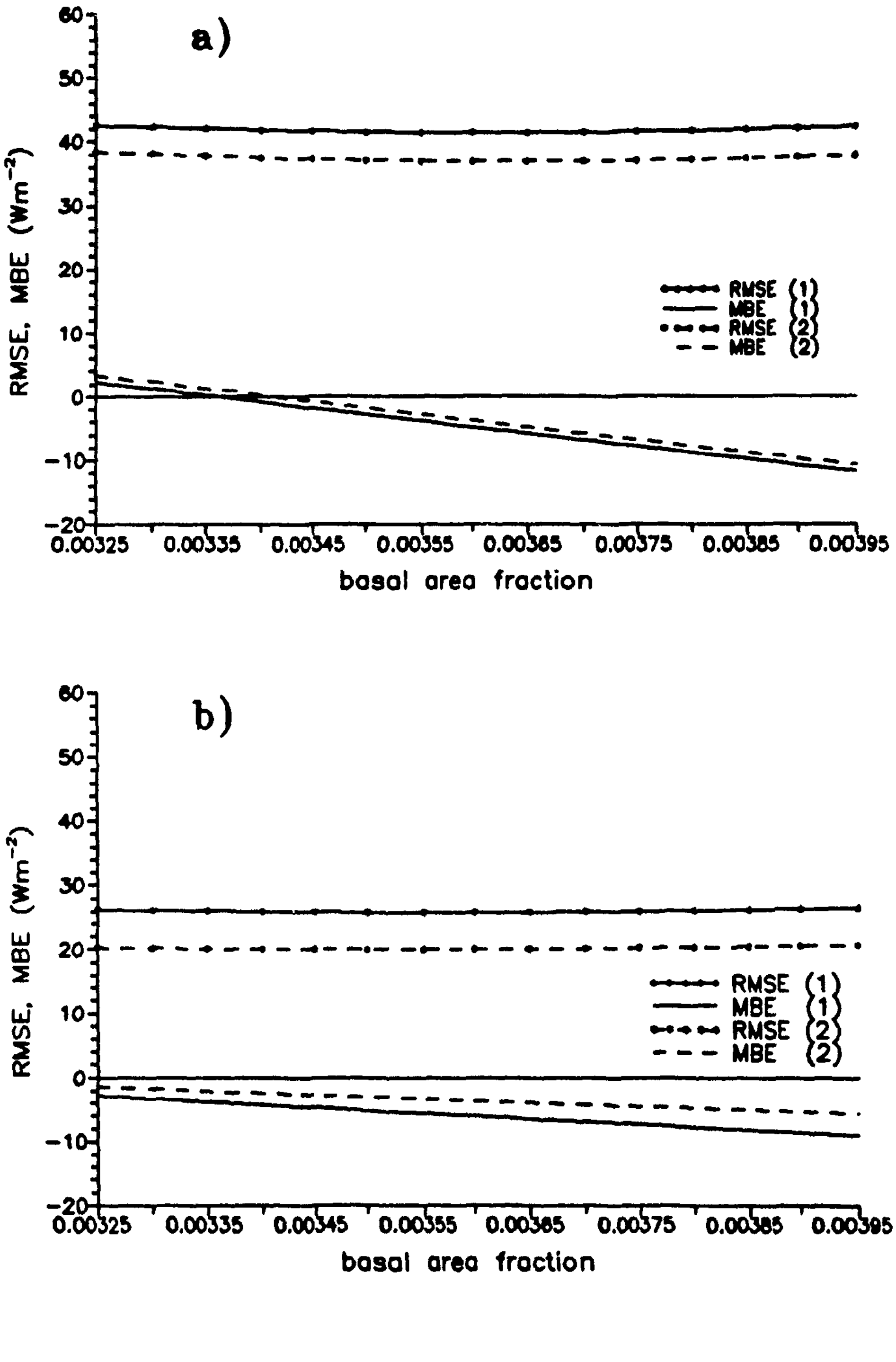

FIGURE 5.14. RMSE and MBE vs. basal area fraction, for calibration (1) and verification (2) data sets: a) site 1 and b) site 2.

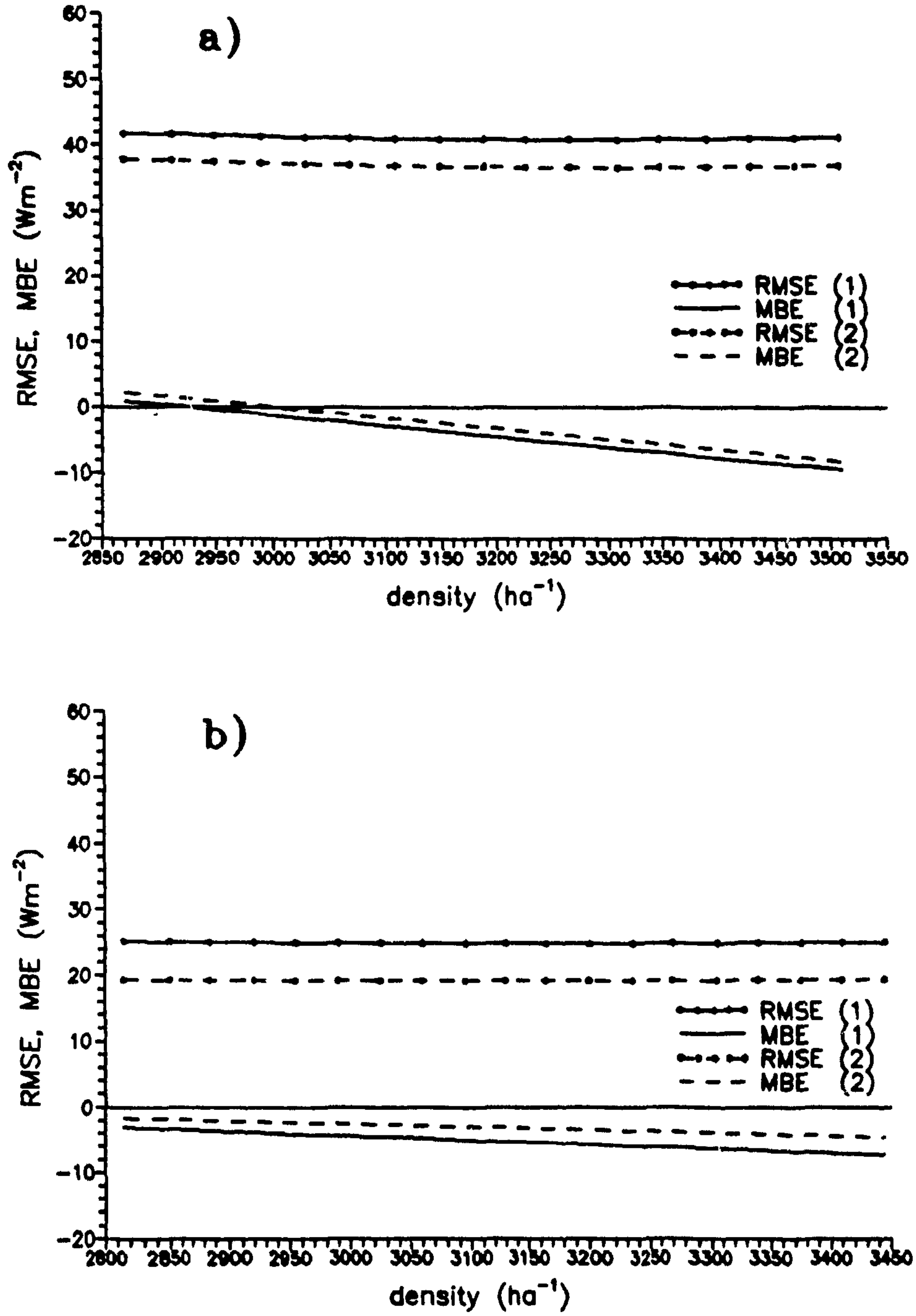

FIGURE 5.15. RMSE and MBE vs. stand density, for calibration (1) and verification (2) data sets: a) site 1 and b) site 2.

Note that these are all worst case deviations, dependent upon the data set; worst case values for the three other sets of calculations involved with each parameter are often much less than the values mentioned.

Tree height changes also have the greatest effect on model performance as measured by the mean bias error; however, the differences amongst the four parameters are not as great as for the RMSE. Worst case deviations for 10% decreases in each parameter are as follows: -9.0 Wm^{-2} for tree height, -7.1 Wm^{-2} for basal area fraction, -7.0 Wm^{-2} for arithmetic mean diameter, and -5.0 Wm^{-2} for stand density. Variations in MBE are given in Wm^{-2} rather than as percentage values because the small absolute values of MBE (ranging from 3.5 to 5.9 Wm^{-2}) result in seemingly unrealistic percentage changes.

The model is most sensitive to tree height because it is the only stand parameter which has an effect on the transmissivity of the crown space to solar radiation. An increase in tree height will cause a larger error at the surface due to cumulative errors in both the crown space and stem space. For all stand parameters, an increase in the parameter value results in a more negative value for the MBE because each case 'adds' shadow to the slope of the theoretical stem space, resulting in a greater under-prediction of the actual solar irradiance incident upon the surface. Sensitivity of the model to basal area fraction is tested because of its use as measured input to the original Federer model (1971); arithmetic mean diameter is used as input to the extended model. Federer's model cannot be tested for sensitivity to the quadratic mean diameter because this parameter would be in the denominator (equation 3.12), resulting in less negative values of MBE with increasing diameter, which is contrary to the actual situation.

Finally, with respect to all parameters the model appears more sensitive to the data at site 1 than at site 2. This is probably due to two factors: first, the data set for site 1 includes more sunny days and considerably fewer cloudy days than for site 2 and, secondly, because of its southerly exposure, a greater proportion of the solar irradiance values at site 1 were observed during periods of small incidence and small zenith angle. Both of these factors tend to result in higher and more variable solar irradiance values for site 1 and, consequently, a greater increase in the error.

5.4.2. SITE CHARACTERISTICS

To determine sensitivity of the model to site characteristics, slope degree was allowed to vary ±5° and slope azimuth approximately ±20°. Changes in slope inclination affect model performance, as determined by the RMSE, much more severely at site 2 than at site 1 (Figure 5.18). An increase in slope of five degrees at site 2 results in increases in RMSE of 11.4% (2.8 Wm^{-2}) and 12.3% (2.4 Wm^{-2}) for the calibration and verification data sets, respectively. At site 1, the equivalent increases in RMSE are 3.9% (1.4 Wm^{-2}) and 2.2% (0.9 Wm^{-2}). Decreases in slope degree affect model performance much less; a decrease of five degrees results in increases in RMSE of only 1.5% for both the calibration and verification data sets at site 2 (similar results occur at site 1).

Percent increases in RMSE associated with increases in slope degree are larger at site 2 than at site 1, but this is primarily due to two factors. First, the lower solar irradiance values at site 2 result in larger percentage errors. Secondly, slope orientation plays an important role. North-facing site 2 is more sensitive to changes at these slope inclinations because of the relationship between slope degree, solar incidence angle, and solar irradiance values. An increase in slope at the north-facing site results in proportionately larger changes in solar incidence angle (for given solar zenith and azimuth angles) than at the south-facing site and, consequently, results in greater changes in the error.

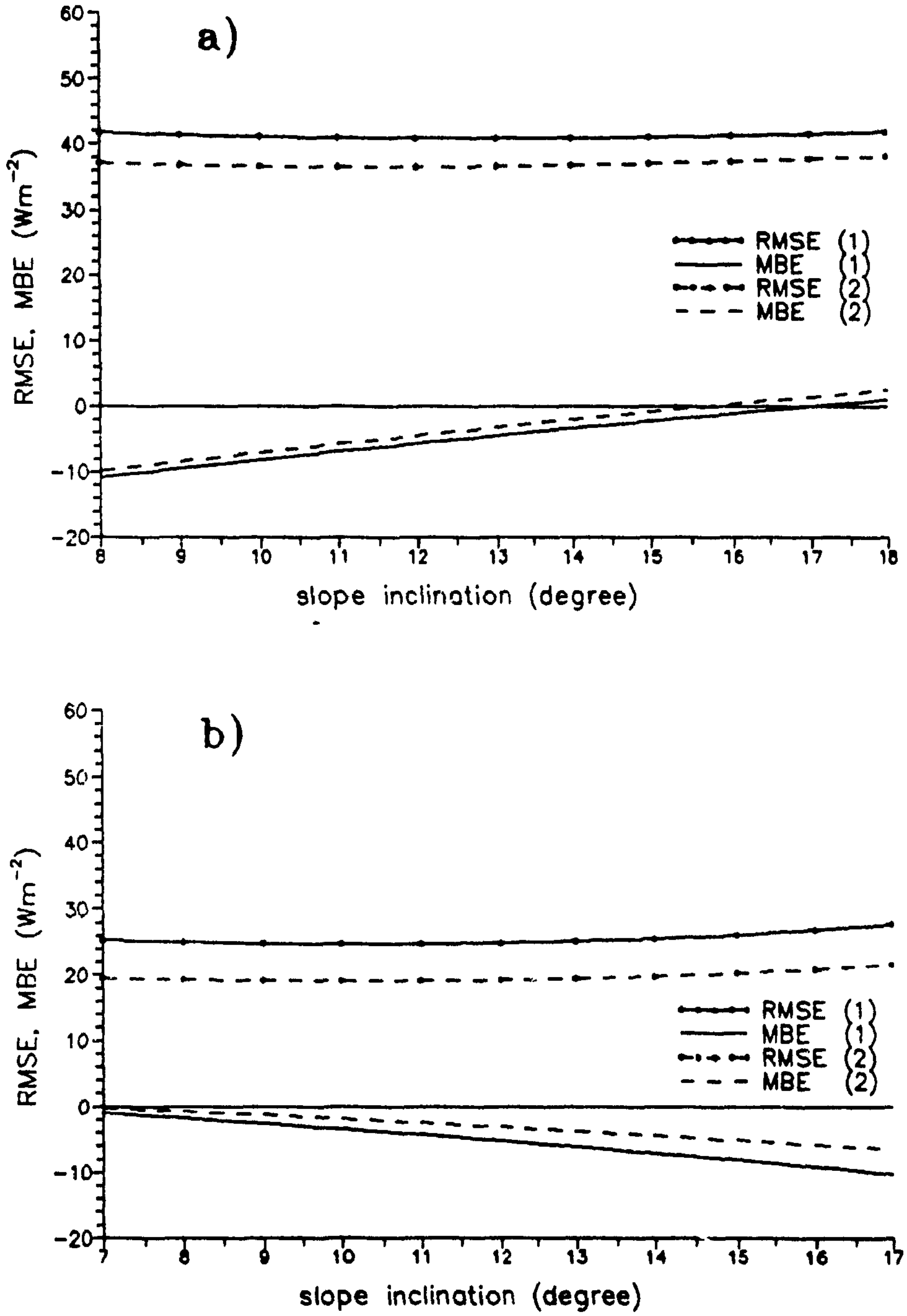

FIGURE 5.16. RMSE and MBE vs. slope inclination, for calibration (1) and verification (2) data sets: a) site 1 and b) site 2.

Root mean square error tends either to increase or to decrease monotonically as azimuth angle varies, contrary to results for the previous parameters for which RMSE always increased from a minimum value as the parameter value either increased or decreased. The changes, however, are not great (Figure 5.17). Maximum increases in RMSE for a change in azimuth of ±20° are 10.3% (2.6 Wm^{-2}) at site 2 and 5.3% (2.2 Wm^{-2}) at site 1. The greater percentage increase at site 2 is due primarily to the lower solar irradiance values.

When model performance is analyzed using MBE as the sensitivity criterion, the model appears insensitive to changes in azimuth angle of ±20° (maximum MBE change of 2.0 Wm^{-2}), but sensitive to changes in slope degree of ±5° (maximum MBE change of 8.6 Wm^{-2}). Variations in site orientation at a south-facing slope will result in over/under-predictions followed by under/over-predictions as the sun follows its path across the sky (if sky conditions remain relatively constant), and thus MBE changes very little. The same tendency for under and over-predictions to cancel each other would exist for north-facing slopes, but not necessarily for other slope aspects. Changes in slope degree will affect model performance more severely when solar incidence and/or zenith angle are large.

Sensitivity of the model to changes in slope inclination and orientation cannot be directly compared to each other for a similar range of -10% to +10% since both variables are relative rather than absolute values. However, allowing deviations of ±5° for slope degree should cover any error involved in field measurements. Because slope aspect is more difficult to determine than slope degree, and because the total range of possible azimuth angles is four times that of zenith angles, azimuth values have been allowed to vary as much as ±20°. It does appear, though, that for slopes of

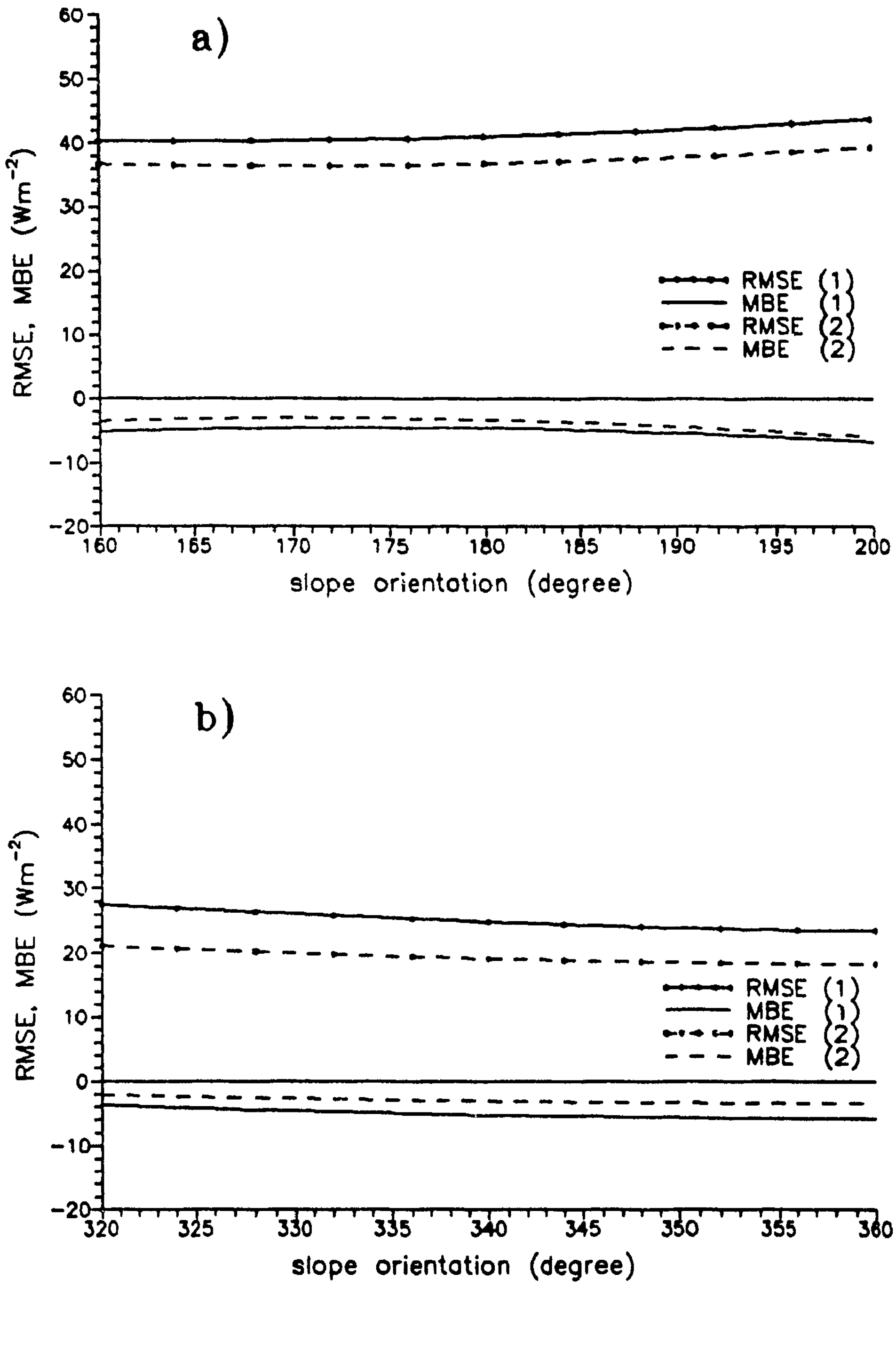

FIGURE 5.17. RMSE and MBE vs. slope orientation, for calibration (1) and verification (2) data sets: a) site 1 and b) site 2.

moderate inclination the model is slightly more sensitive to slope degree than to slope azimuth, especially if slope degree varies as much as azimuth angle.

5.5. IMPROVEMENT IN MODEL PERFORMANCE WITH INTEGRATION TO HOURLY AND DAILY TIME PERIODS

Error calculations were made for hourly and daily time periods to determine whether model performance improves, and if so by how much, for lengthened time intervals. For integration to hourly time periods, observed and predicted solar irradiance values were first averaged over the hour (three 20-minute periods), then compared to produce hourly data points for the RMSE and MBE. For integration to daily

time periods, an error value is obtained from daily averages for predicted and observed values. Daily error, as a percent value, may be regarded as the absolute value of the predicted minus observed, divided by the observed value. Results are shown in Figure 5.16 for the total data collection period. Although the daily errors are not true RMSE values in the sense that they are derived from only one pair of values, they do give an indication of the total error associated with that time period, and are therefore included in the graph for comparison purposes. The connecting lines are included only to facilitate reading of the graph and make no inference concerning intervening days which belong to the calibration data set. Although there are exceptions, the greatest improvements in performance generally occur for sunny sky conditions (Julian dates 69, 77, 82, 101 and 104), while the smallest improvements occur for overcast conditions (Julian dates 71, 90, 92, 93, 97 and 105), especially at the south-facing site.

Results for the entire verification data sets are given in Table 5.7. There is a significant improvement in model performance (decrease in RMSE) when integrating from 20-minute averaging periods to hourly averaging periods; RMSE

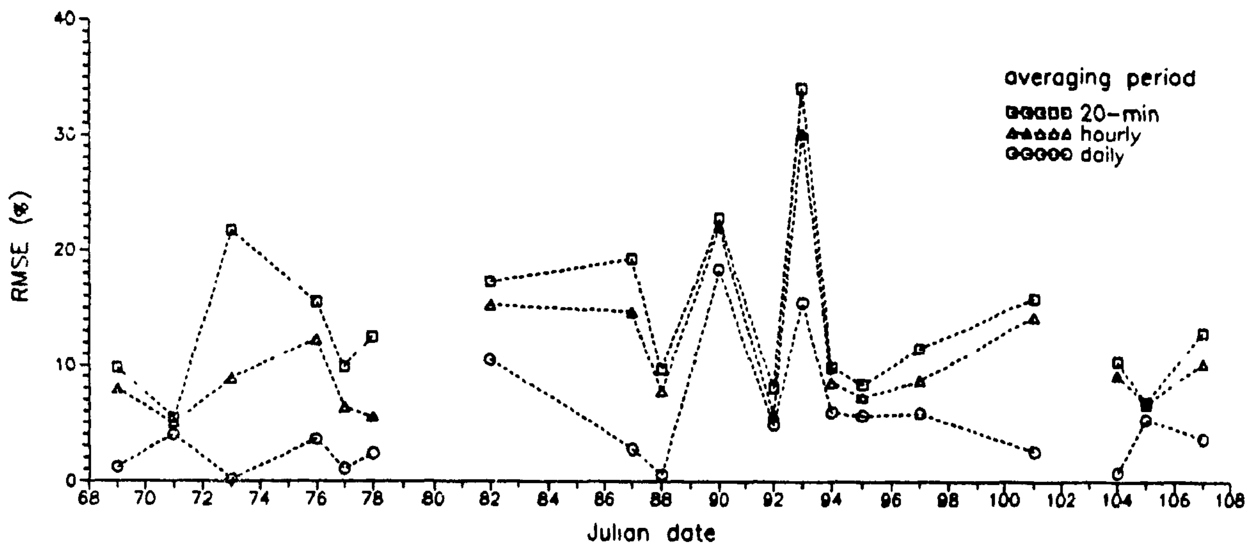

FIGURE 5.18. Root mean square and daily errors for 20-minute, hourly and daily averaging periods; lines connecting data points are to facilitate interpretation of the graph, and intend no inference concerning the intervening days which belong to the calibration data set.

Table 5.7: Improvement in model performance (RMSE%) with integration from 20-minute time periods to hourly and daily time periods. RMSE% values are given as percentages of the average solar irradiance for the particular data set.

averaging period	RMSE% Site 1	RMSE% Site 2
20-minute	13.0	17.0
hourly	8.8	14.6
daily	2.5	6.8

decreases 32.3% and 14.1% at sites 1 and 2, respectively. Values for RMSE differ slightly from those given in Table 5.2 for 20-minute averaging periods; the desire to use the same data set when comparing with results for hourly periods required the elimination of several 20-minute periods. An even greater decrease in the total error is experienced when further integrating to daily averaging periods (further decreases of 71.6% and 53.4%). Root mean square errors as percent values for the entire verification data sets are only 2.5% and 6.8% for site 1 and site 2, respectively, when daily averaged values are considered. Mean bias errors, which do not change with increasing time intervals, are -1.1% and -2.8% for the same data sets. The greater improvements at the south-facing site are probably due to the extra sunny day and one less overcast day included in its verification data set compared to the north-facing site, and the high percentage errors at site 2 resulting from very low solar irradiance averages for certain days (e.g., for Julian dates 90 and 93, average solar irradiance values are 15.2 and 73.3 Wm^{-2}, respectively).

CHAPTER 6

CONCLUSION

6.1. SUMMARY

This study has tested a physically based model which quantitatively describes solar irradiance incident upon slopes of any inclination and orientation under a leafless, deciduous forest. Furthermore, the variability of the incident solar irradiance has been analyzed for different meteorological conditions and earth-sun geometric configurations. This chapter discusses briefly some problems inherent in the model, presents a summary of the major findings of the study, and suggests directions for further research.

6.2. PROBLEMS INHERENT IN THE MODEL

Calibration of the model presents the first problem inherent in the model. The crown space absorption coefficient must be empirically derived from the measured transmissivity data, resulting in a parameter which is site specific. The empirical nature of the absorption coefficient also means that it may mask deficiencies in the parameterization of the stem space as shadow-casting cylinders. Since the model contains a parameter which is site specific it may be useful for long-term studies involving solar irradiance incident upon sloping surfaces under leafless deciduous canopies, or subsequent melting of a snowpack within such forests, but may not be directly applied to characteristically different forest stands.

Values for the absorption coefficient differ substantially from one site to the other, as well as from those given by Federer (1971, p. 8). However, the difference between sites 1 and 2 is probably due to the inhomogeneity of the forest stand at site 2; the difference between values for the absorption coefficient for this study and those derived by Federer are probably due in large part to the use of arithmetic mean diameter rather than quadratic mean diameter. Use of quadratic mean diameter results in absorption coefficients much nearer the value given by Federer for a stand with similar basal area fraction (0.017 and 0.025 vs. 0.019), although the coefficient remains site specific.

Another problem inherent in the model is its reliance upon values of global and diffuse irradiance measured at one site above the canopy to represent the same values throughout a larger area. This is a problem particularly for instantaneous values or short-term averaging for partial cloud sky conditions. For overcast or sunny sky conditions, distance between the above-canopy site and any slope facet is not important. For longer averaging periods, solar irradiance may be considered conservative over large areas, and short-term differences generally cancel each other. It has been shown that model performance improves (RMSE as percentage value decreases) 32.2% when integrating from 20-minute averages to hourly averages, and 80.8% when integrating from 20-minute averages to daily averages.

Although not a problem inherent in the model, calibration of the model may present problems. Contrary to the insensitivity of the model to changes in the crown space absorption coefficient when measured by RMSE, the model is quite sensitive when evaluated using MBE as a criterion. Hence, the absorption coefficient must be properly chosen in order to minimize the possibility of large systematic error. The model would give better results if the absorption coefficient were determined through minimization of the absolute value of MBE rather than RMSE. This would improve model performance for both short- and long-term averaging periods, since the systematic error would remain near zero while the overall error would be only very slightly larger. For predicting solar irradiance at the surface, and for subsequent use in operational snowmelt models, eliminating or minimizing systematic error would be preferable. However, this eliminates the possibility of determining whether systematic error exists, and/or reducing systematic error.

6.3. MODEL PERFORMANCE AND SENSITIVITY ANALYSIS

Results attest to the overall good performance of the model when applied to verification data sets as an independent test. When data from the two sites are combined, percentage errors, based on 20-minute averages of instantaneous values, are 15.5% for RMSE and -1.9% for MBE. A comparison between the total error (RMSE) and that component of RMSE which is due to error in the sample means (SE) allows an estimate of the modelling error. For the case cited above, model error is 14.0%. Partial cloud sky conditions result in the highest model error (15.7%) due to the inherent spatial and temporal variability of solar irradiance at the surface under such conditions, such that both sunny and overcast sky conditions can be more reliably modelled (as evaluated by the total or root mean square error) than the former over the time period from sunrise to sunset. Sunny sky conditions result in low model error (6.3%) due to calibration procedures, but also result in the highest sampling error (6.9%) due to the spatial distribution of shadows. Lowest sampling error occurs for overcast sky conditions (2.6%).

When the data set at each site is divided into subsets according to daily sky condition, results show an increase in both the error and the variability in the error associated with high solar irradiance values. This is generally due to the variability of the direct component of solar irradiance, and the positive association between direct and global solar irradiance values. The greatest variability appears for partial cloud conditions, but is due to the problem associated with the distance between tower and field sites; this would not be a problem for longer interval averaging periods.

Variability in the error increases with decreasing zenith or incidence angle, although for steeper slopes zenith angle may increase while incidence angle decreases, resulting in a tendency for the error to both increase and decrease in variability at the same time. Surprisingly, both RMSE and MBE as percentage values remain relatively constant with increasing ratio of direct to global solar irradiance. In this case, the increase in the absolute values of RMSE probably result not from the increased variability due to the direct component of solar irradiance, but from inhomogeneity of the crown space (i.e., not a homogeneous absorber of solar irradiance as assumed). A slight portion of the increase in RMSE may also be due to the assumption that basal area is negligible.

Sensitivity analyses show that the model is insensitive to changes in stand and site characteristics when RMSE is used to evaluate model performance. When MBE is used as a criterion, results show that the model reacts most severely to changes in tree height; this is because tree height is the only stand parameter which has an effect upon the transmissivity of the crown space, as well as upon the parameterization of the stem space. The model also exhibits more sensitivity to changes in slope inclination than slope orientation.

6.4. SAMPLING VARIABILITY AND INSTRUMENT REQUIREMENTS

The time and investment involved in acquiring field data imparts importance to an analysis of sampling variability and the number of radiometers required to limit sampling error to a predetermined level. For overcast sky conditions, as well as for daily averaging periods, error bounds about the sample means for a 95% confidence level remain low, ranging from 4.6 to 6.3 percent of the average irradiance values for all cases. However, for partially cloudy sky conditions, 95% confidence bounds for hourly and 20-minute averaging periods are 11.2% and 14.5% of the average irradiance values, respectively. The equivalent values for sunny sky conditions are 14.6% and 20.1%.

The large number of radiometers required to estimate below-canopy global radiation adequately may be attributed to the spatial variations in shadows as they move across the forest floor. For overcast sky conditions only two or three radiometers are required to limit solar irradiance values to within 5% of the mean values for daily, hourly or 20-minute averaging periods. For partial cloud sky conditions, the number of radiometers required is three and seventeen for daily and 20-minute averaging periods, respectively. For sunny sky conditions the equivalent numbers are four and thirty-two instruments. Doubling the allowable error results in a fourfold reduction in number of radiometers necessary.

6.5. IMPROVEMENT IN SOLAR IRRADIANCE PREDICTION

Federer's model (1971), when extended to allow for slopes of any inclination and orientation, works well for predicting solar irradiance incident upon the forest floor under a leafless deciduous canopy if properly calibrated. However, several minor adjustments should result in a more realistic calibration of the model. The model should be adapted to anisotropic sky conditions, especially for circumsolar brightening, possibly reducing the systematic under- and over-prediction at low and high solar irradiance values on sunny days. Incorporation of basal area into the total shadow area cast by the tree stems would also help in eliminating differences between under- and over-prediction at large and small zenith or incidence angle.

For application of the model to sites of greater slope inclination, and for subsequent application to snowmelt modelling, further analysis should first determine the dependency of transmissivity of the canopy to solar irradiance values (and the variability of such values) upon solar incidence angle and solar zenith angle; minimum solar incidence angle results in the shortest path length through the crown space, whereas minimum zenith angle results in the least amount of shadow area. Also, the model should be tested in other leafless deciduous forests to determine the possible range of values for the crown space absorption coefficient, as well as tested for sites of different slope inclinations and orientations.

Further studies should concentrate on the physical parameterization of the crown space with the intent of eliminating the need to derive the absorption coefficient empirically for each site. This should allow another test of the validity of the present stem space parameterization. The albedo of the forest stand, multiple reflections between the surface and the canopy, and radiation reflected from surrounding terrain should be considered in order to account more realistically for solar radiative exchanges within the canopy.

REFERENCES

Anderson, E.A., 1976. A point energy and mass balance model of a snow cover. *NOAA Technical Report*, No. NWS 19. U.S. Department of Commerce, Washington D.C.

Arnfield, A.J., 1987. A Fourier series approach to skyline generalization for surface irradiance estimates in alpine terrain. *Arctic and Alpine Research*, 19: 270-278.

Badescu, V., 1988. Comment on the statistical indicators used to evaluate the accuracy of solar radiation computing models. *Solar Energy*, 40: 479-480.

Baldocchi, D.D., B.A. Hutchison, D.R. Matt and R.T. McMillen, 1984. Seasonal variations in the radiation regime within an oak-hickory forest. *Agricultural and Forest Meteorology*, 33: 177-191.

Baldocchi, D.D., B.A. Hutchison, D.R. Matt and R.T. McMillen, 1986. Seasonal variation in the statistics of photosynthetically active radiation penetration in an oak-hickory forest. *Agricultural and Forest Meteorology*, 36: 343-361.

Baldocchi, D.D., D.R. Matt, B.A. Hutchison and R.T. McMillen, 1984. Solar radiation within an oak-hickory forest: an evaluation of the extinction coefficients for several radiation components during fully-leafed and leafless periods. *Agricultural and Forest Meteorology*, 32: 307-322.

Becker, P., D.W. Erhart and A.P. Smith, 1989. Analysis of forest light environments: Part I. Computerized estimation of solar radiation from hemispherical canopy photographs. *Agricultural and Forest Meteorology*, 44: 217-232.

Bourges, B., 1985. Improvement in solar declination computation. *Solar Energy*, 35: 367-369.

Burch, G.J., R.K. Bath, I.D. Moore and E.M. O'Loughlin, 1987. Comparative hydrological behaviour of forested catchments in southeastern Australia. *Journal of Hydrology*, 90: 19-42.

Christopherson, N., S. Rustad and H.M. Seip, 1984. Modelling streamwater chemistry with snowmelt. *Philosophical Transactions of the Royal Society of London, Series B*, 305: 427-439.

Cohen, S. and M. Fuchs, 1987. The distribution of leaf area, radiation, photosynthesis and transpiration in a shamouti orange hedgerow orchard. *Agricultural and Forest Meteorology*, 40: 123-144.

Coulson, K.L., 1975. *Solar and Terrestrial Radiation*. Academic Press, New York, 322 pp.

Curtis, R.O., 1968. Which average diameter? *Journal of Forestry*, 66: 570.

Davies, J.A., 1981. Models for estimating incoming solar irradiance. *Canadian Climate Centre*, Report no. 81-2, (unpublished manuscript). Atmospheric Environment Service, Downsview, Ontario.

Davies, J.A., M. Abdel-Wahab and D.C. McKay, 1984. Estimating solar irradiation on horizontal surfaces. *International Journal of Solar Energy*, 2: 405.

Dozier, J., 1979. A solar radiation model for a snow surface in mountainous terrain. In: S.C. Colbeck and M. Ray (Editors), *Proceedings: Modeling of Snow Cover Runoff*. U.S. Army CRREL, Hanover, NH, pp. 144-153.

Dozier, J., 1980. A clear-sky spectral solar radiation model for snow-covered mountainous terrain. *Water Resources Research*, 16: 709-718.

Drummond, A.J., 1964. Comments on "Sky radiation measurement and corrections". *Journal of Applied Meteorology*, 3: 810-811.

Drummond, A.J. and H.W. Greer, 1966. An integrating hemisphere (artificial sky) for the calibration of meteorological pyranometers. *Solar Energy*, 10: 190-194.

Federer, C.A., 1971. Solar radiation absorption by leafless hardwood forests. *Agricultural Meteorology*, 9: 3-20.

Fitzgibbon, J.E. and T. Dunne, 1980. Snowmelt prediction in a subarctic drainage area. *Nordic Hydrology*, 11: 243-254.

Flint, A.L. and S.W. Childs, 1987. Calculation of solar radiation in mountainous terrain. *Agricultural and Forest Meteorology*, 40: 233-249.

Garnier, B.J. and A. Ohmura, 1968. A method of calculating the direct shortwave radiation income of slopes. *Journal of Applied Meteorology*, 7: 796-800.

Garnier, B.J. and A. Ohmura, 1970. The evaluation of surface variations in solar radiation income. *Solar Energy*, 13: 21-34.

Gay, L.W., K.R. Knoerr and M.O. Braaten, 1971. Solar radiation variability on the floor of a pine plantation. *Agricultural Meteorology*, 8: 39-50.

Geiger, R., 1965. *The Climate near the Ground.* Harvard University Press, Cambridge, MA, 611 pp.

Granberg, H.B., 1988. A forest shading model using bit-mapped graphics. *Agricultural and Forest Meteorology*, 43: 225-234.

Hay, J.E., 1986. Calculation of solar irradiances for inclined surfaces: validation of selected hourly and daily models. *Atmosphere-Ocean*, 24: 16-41.

Hay, J.E. and J.A. Davies, 1980. Calculation of the solar radiation incident on an inclined surface. In: J.E. Hays and T.K. Won (Editors), *Proceedings, First Canadian Solar Radiation Data Workshop.* Atmospheric Environment Service, Downsview, Ontario, pp. 59-72.

Hay, J.E. and D.C. McKay, 1985. Estimating solar irradiance on inclined surfaces: a review and assessment of methodologies. *International Journal of Solar Energy*, 3: 203-240.

Hendrick, R.L., B.D. Filgate and W.M. Adams, 1971. Application of environmental analysis to watershed snowmelt. *Journal of Applied Meteorology*, 10: 418-429.

Hendrie, L.K. and A.G. Price, 1979. Energy balance and snowmelt in a deciduous forest. In: S.C. Colbeck and M. Ray (Editors), *Proceedings: Modeling of Snow Cover Runoff.* U.S. Army CRREL, Hanover, NH, pp. 211-221.

Herbert, T.J., 1987. Area projections of fisheye photographic lenses. *Agricultural and Forest Meteorology*, 39: 215-223.

Hill, A.N., 1966. Calibration of solar radiation equipment in the U.S. Weather Bureau. *Solar Energy*, 10: 184-187.

Horowitz, J.L., 1969. An easily constructed shadow-band for separating direct and diffuse solar radiation. *Solar Energy*, 12: 543-545.

Hutchison, B.A. and D.R. Matt, 1977. The annual cycle of solar radiation in a deciduous forest. *Agricultural Meteorology*, 18: 255-265.

Impens, I., R. Lemeur and R. Moermans, 1970. Spatial and temporal variation of net radiation in crop canopies. *Agricultural Meteorology*, 7: 335-337.

Iqbal, M., 1983. *An Introduction to Solar Radiation*. Academic Press, Toronto, 390 pp.

Jeffrey, W.W., 1968. Snow Hydrology in the forest environment. In: *Snow Hydrology, Proceedings of Workshop Seminar*. Secretariat, Canadian National Committee for the International Hydrological Decade, Ottawa, pp. 1-19.

Kauth, J. and J.L. Penquite, 1967. The probabililty of clear lines of sight through a cloudy atmosphere. *Journal of Applied Meteorology*, 6: 1005-1017.

Kondrat'yev, K. Ya., 1965. *Radiative Heat Exchange in the Atmosphere*. Pergamon Press, Oxford, 411 pp.

Kondrat'yev, K. Ya., 1969. *Radiation in the Atmosphere*. Academic Press, New York, 912 pp.

Kondrat'yev, K. Ya., 1977. Radiation regime of inclined surfaces. *WMO Technical Note*, 152. Secretariat of the WMO, Geneva, 82 pp.

Kuuluvainen, T. and T. Pukkala, 1987. Effect of crown shape and tree distribution on the spatial distribution of shade. *Agricultural and Forest Meteorology*, 40: 215-231.

Latimer, J.R., 1966. Calibration program of the Canadian Meteorolgical Service. *Solar Energy*, 10: 187-190.

Latimer, J.R., 1972. Radiation Measurement. In: J. MacDowall (Editor), *International Field Year for the Great Lakes*. Canadian National Committee for the International Hydrological Decade, Ottawa, pp. 1-51.

Lawrence, G.B., C.T. Driscoll and R.D. Fuller, 1988. Hydrologic control of aluminum chemistry in an acidic headwater stream. *Water Resources Research*, 24: 659-669.

Lemeur R. and B.L. Blad, 1974. A critical review of light models for estimating the shortwave radiation regime of plant canopies. *Agricultural Meteorology*, 14: 255-286.

Male, D.H. and R.J. Granger, 1981. Snow surface energy exchange. *Water Resources Research*, 17: 609-627.

McKay, G.A., 1970. Precipitation. In: D.M. Gray (Editor), *Handbook on the Principles of Hydrology*. Canadian National Committee for the International Hydrological Decade, Ottawa, pp. 2.1 - 2.111.

Mukammal, E.I., 1971. Some aspects of radiant energy in a pine forest. *Archiv fur Meteorologie Geophysik und Bioklimatologie, Serie B*, 19: 29-52.

Myneni, R.B., J. Ross and G. Asrar, 1989. A review of the theory of photon transport in leaf canopies. *Agricultural and Forest Meteorology*, 45: 1-153.

Nadeau, C.A. and H. B. Granberg, 1986. Variations in net radiation over snow at a boreal forest edge. In: J.E. Lewis (Editor), *Proceedings of the Forty-third Eastern Snow Conference*. Hanover, NH, pp. 198-203.

Norman, J.M. and J.M. Welles, 1983. Radiative transfer in an array of canopies. *Agronomy Journal*, 75: 481-488.

Nunez, M., 1985. Modelling daily global radiation at the forest floor. *Boundary Layer Meteorology*, 33: 379-395.

Obled, Ch. and H. Harder, 1979. A review of snow melt in the mountain environment. In: S.C. Colbeck and M. Ray (Editors), *Proceedings: Modeling of Snow Cover Runoff*. U.S. Army CRREL, Hanover, NH, pp. 179-204.

Ohmura, A., 1977. The derivation of a formula to calculate direct short-wave radiation on slopes. *Climatological Bulletin*, 21. McGill University, Montréal, pp. 34-41.

Ovington, J.D. and H.A.I. Madgwick, 1955. A comparison of light in different woodlands. *Forestry*, 28: 141-146.

Péch, G., 1986. Mobile sampling of solar radiation under conifers. *Agricultural and Forest Meteorology*, 37: 15-28.

Peterson, W.A., I. Dirmhirn and R.L. Hurst, 1985. A theoretical model to determine solar and diffuse irradiance in valleys. *Solar Energy*, 35: 503-510.

Petzold, D.E., 1981. The radiation balance of melting snow in open boreal forest. *Arctic and Alpine Research*, 13: 287-293.

Press, W.H., B.P. Flannery, S.A. Teukolsky and W.T. Vetterling, 1987. *Numerical Recipes*. Cambridge University Press, New York, 818 pp.

Price, A.G., 1988. Prediction of snowmelt rates in a deciduous forest. *Journal of Hydrology*, 101: 145-157.

Price, A.G. and T. Dunne, 1976. Energy balance computations of snowmelt in a subarctic area. *Water Resources Research*, 12: 686-694.

Reifsnyder, W.E., G.M. Furnival and J.L. Horowitz, 1971. Spatial and temporal distribution of solar radiation beneath forest canopies. *Agricultural Meteorology*, 9: 21-37.

Reifsnyder, W.E. and H.W. Lull, 1966. *Radiant Energy in Relation to Forests*. Technical Bulletin No. 1344, USDA Forest Service, Washington, D.C., 111 pp.

Roberge, J., H.G. Jones, J. Stein and W. Sochanska, 1985. An integrated model of snowmelt quality for boreal forest sites. In: J.E. Lewis (Editor), *Proceedings of the Forty-second Eastern Snow Conference*. Montréal, pp. 69-83.

Sattler, M.A., S.Sharples and J.K. Page, 1987. The geometry of the shading of buildings by various tree shapes. *Solar Energy*, 38: 187-201.

Skartveit, A. and J.A. Olseth, 1986. Modelling slope irradiance at high latitudes. *Solar Energy*, 36: 333-344.

Swift, L.W. Jr., 1976. Algorithm for solar radiation on mountain slopes. *Water Resources Research*, 12: 108-112.

Takenaka, A., 1987. Analysis of light transmissivity of forest canopies with a telephoto method. *Agricultural and Forest Meteorology*, 40: 359-369.

U.S.A.C.E. (U.S. Army Corps of Engineers), 1956. *Snow Hydrology*. North Pacific Division, U.S.A.C.E., Portland, Oregon.

Vales, D.J. and F.L. Bunnell, 1988. Relationships between transmission of solar radiation and coniferous forest stand characteristics. *Agricultural and Forest Meteorology*, 43: 201-223.

Walraven, R., 1978. Calculating the position of the sun. *Solar Energy*, 20: 393-397.

Wang, H. and D.D. Baldocchi, 1989. A numerical model for simulating the radiation regime within a deciduous forest canopy. *Agricultural and Forest Meteorology*, 46: 313-337.

Willmott, C.J., 1981. On the validation of models. *Physical Geography*, 2: 184-194.

Wilson, R.G. and D.E. Petzold, 1973. A solar radiation model for sub-arctic woodlands. *Journal of Applied Meteorology*, 12: 1259-1266.

WMO (World Meteorological Organization), 1986. Intercomparison of conceptual models of snowmelt runoff. *Operational Hydrology Report*, No. 23, Geneva.

Zavitkovski, J., 1982. Characterization of light climate under canopies of intensely-cultivated hybrid poplar plantations. *Agricultural Meteorology*, 25: 245-255.

Zuzel, J.F. and L.M. Cox, 1975. Relative importance of meteorological variables in snowmelt. *Water Resources Research*, 11: 174-176.

APPENDIX A

DERIVATION OF GENERALIZED RELATIONSHIPS

(R.D. Moore)

Consider a Cartesian coordinate system (x,y,z) with x increasing to the east, y increasing to the north and z increasing vertically. A point in this system, in reference to earth-sun geometry, can also be represented in terms of the spherical coordinates (r,z_1,θ), where r is the distance from the origin to the point, z_1 is the solar azimuth angle (east equals zero, and increases anti-clockwise) and θ is solar zenith angle. Transformation from spherical to Cartesian coordinates is as follows:

$$(x,y,z) = [r\cdot\cos(z_1)\sin\theta, r\cdot\sin(z_1)\sin\theta, r\cdot\cos\theta] \qquad \text{(A1)}$$

In Cartesian coordinates, the unit vector from the origin in the direction of the sun (S) is given by:

$$\mathbf{S} = [\cos(z1)\sin\theta, \sin(z1)\sin\theta, \cos\theta] \qquad \text{(A2)}$$

A slope with azimuth (a) and inclination (β, horizontal equals zero), will have a unit normal vector (**X**) defined by:

$$\mathbf{X} = [\cos(a)\sin\beta, \sin(a)\sin\beta, \cos\beta] \qquad \text{(A3)}$$

If the slope is represented by a plane including the origin (0,0,0) then the equation of the slope is

$$\mathbf{X}\cdot\mathbf{p} = 0 \qquad \text{(A4)}$$

where p is a vector representing all points on the plane.

Consider a tree stem on the slope with height (h_s) and diameter (D), both in metres, and the centre of its base at the origin (0,0,0). The vector **L** on the plane which spans the length of the shadow between the points corresponding to the top and bottom of the centre of the stem is derived by finding the point (p^*) which satisfies both Eq. (A4) and the following:

$$\mathbf{p^*} = (0,0,h_s) - v\ \mathbf{S} \tag{A5}$$

where v is the length (in metres) of the vector which connects the centre of the top of the stem to the point p^*, and $\mathbf{p^*}$ is a vector from the origin to the point p^*. Solving Eqs. (A4) and (A5) for v yields:

$$\begin{aligned} v &= h_s\cos\beta/(\mathbf{X}\cdot\mathbf{S}) \\ &= h_s\cos\beta/[\sin\beta\sin\theta\cos(z_1-a) + \cos\beta\cos\theta] \end{aligned} \tag{A6}$$

For economy of expression, the denominator in Eq. (A6) will be denoted C (= cos(i) where i is the solar incidence angle). Substituting for v in Eq. (A5) then yields

$$\mathbf{p^*} = (h_s/C)\ [-\cos\beta\cos(z_1)\sin\theta, -\cos\beta\sin(z_1)\sin\theta, \sin\beta\sin\theta\cos(z_1-a)] \tag{A7}$$

Because the tree is centred at the origin, the vector $\mathbf{L}$ equals $\mathbf{p^*}$.

To find a vector spanning the width of the shadow, we first determine the points (representing vectors $\mathbf{p'}$ and $\mathbf{p''}$ from the origin) where the two edges of the shadow meet the base of the tree; these can be found to be

$$\mathbf{p'} = (D/2)\ [-\sin(z_1), \cos(z_1), \tan\beta\sin(z_1-a)] \tag{A8}$$
$$\mathbf{p''} = (D/2)\ [\sin(z_1), -\cos(z_1), -\tan\beta\sin(z_1-a)] \tag{A9}$$

The desired vector, denoted $\mathbf{w_s}$, is then

$$\mathbf{w_s} = \mathbf{p''} - \mathbf{p'} = D\ [\sin(z_1), -\cos(z_1), -\tan\beta\sin(z_1-a)] \tag{A10}$$

The area of the shadow on the slope will be equal to the area of a parallelogram spanned by the vectors $\mathbf{L}$ and $\mathbf{w_s}$ (this includes half the base of the cylinder and assumes that the end of the stem's shadow is a straight line). The area of the shadow (A_s) is then equal to the modulus of the cross product of $\mathbf{L}$ and $\mathbf{w_s}$, which can be found to be:

$$A_s = D\cdot h_s\sin\theta/C \tag{A11}$$

The path length through the crown space will be given by

$$l_o = (h_o/h_s)v = h_o\cos\beta/C \tag{A12}$$

since h_o and h_s are each defined to be one-half the total tree height.

APPENDIX B

MEASURED DATA IN GRAPHIC PRESENTATION:

GLOBAL RADIATION ABOVE CANOPY
DIFFUSE RADIATION ABOVE CANOPY
GLOBAL RADIATION AT THE SURFACE

The entire data set for each site is presented graphically. Data from the south-facing site (site 1) are presented first, for days 67-79 and 103-108 (8-20 March and 13-18 April), inclusive. Data from the north-facing site (site 2) are presented for days 81-83 and 86-101 (22-24 March and 27 March - 11 April), inclusive.

Global radiation above the canopy on a horizontal surface is shown as a solid line connecting data points. Diffuse radiation above the canopy for a horizontal surface is depicted as a dashed line connecting data points. Global radiation data from the ten solarimeters at the field sites, on sloping surfaces under leafless deciduous canopies, are simply portray as data points. Legends are included on only the first two graphs because of the obvious nature of the traces.

All data are presented in the graphs; however, some data were subsequently eliminated for running of the model due to unsatisfactory adjustment of the shadow band (e.g., after 1500 LST on day 67, after 1640 LST on day 77). Day numbers are given for the day of the year at the top left of each graph.

Calibration data sets (day of the year):

site 1: 67, 68, 70, 72, 74, 75, 79, 103, 106 and 108.

site 2: 81, 83, 86, 89, 91, 96, 98, 99 and 100.

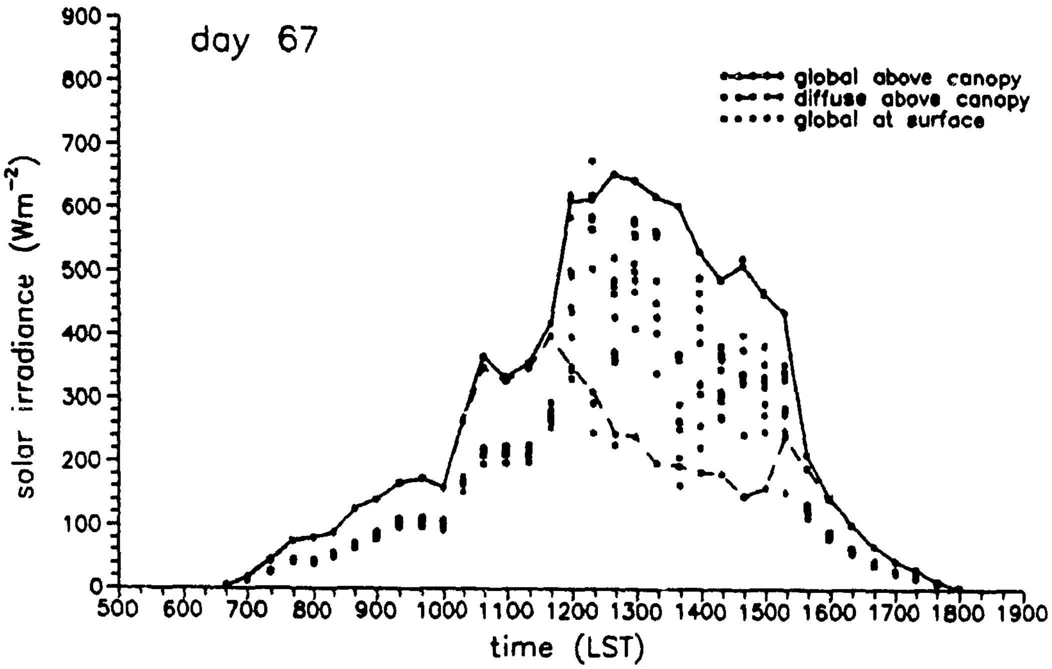
day 67
global above canopy
diffuse above canopy
global at surface
solar irradiance (Wm^{-2})
time (LST)
0
100
200
300
400
500
600
700
800
900
500
600
700
800
900
1000
1100
1200
1300
1400
1500
1600
1700
1800
1900

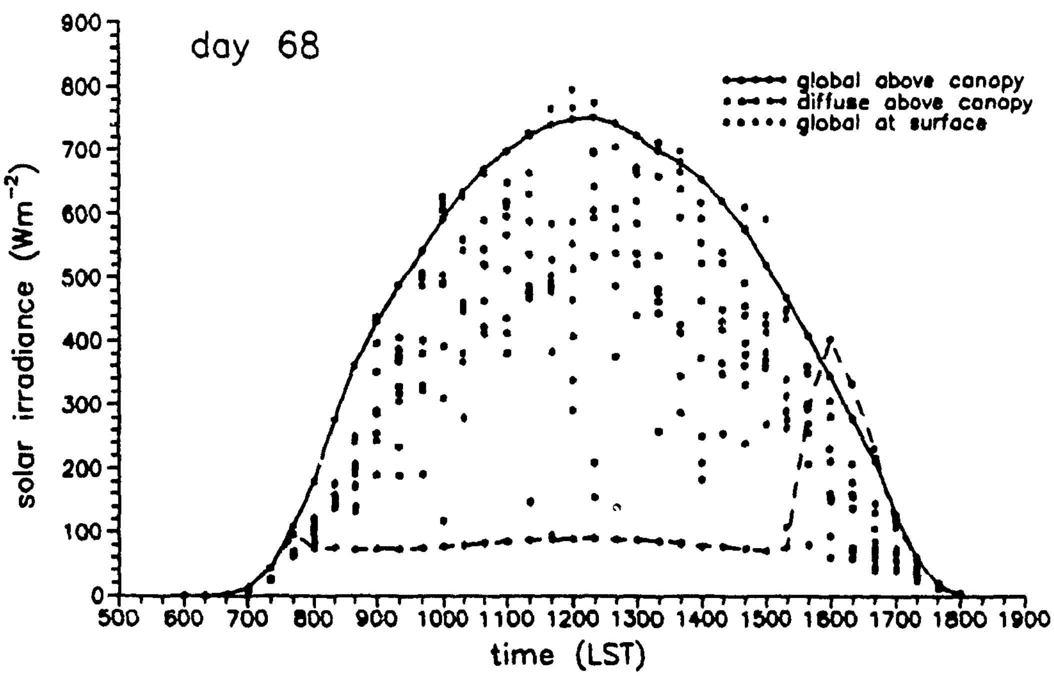
day 68
global above canopy
diffuse above canopy
global at surface
solar irradiance (Wm^{-2})
time (LST)
0
100
200
300
400
500
600
700
800
900
500
600
700
800
900
1000
1100
1200
1300
1400
1500
1600
1700
1800
1900

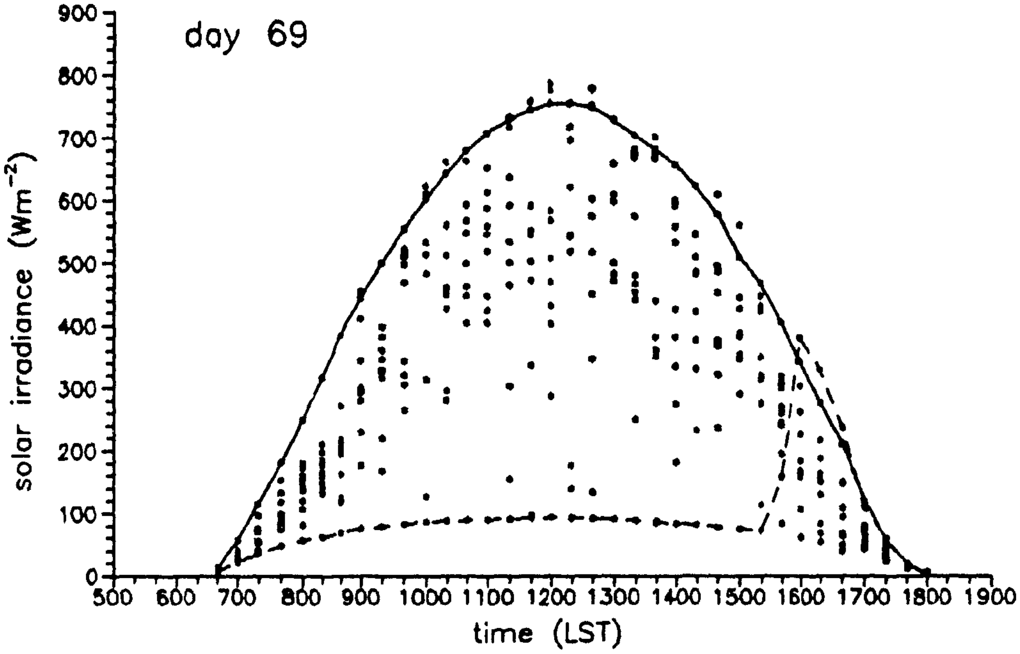
day 69
solar irradiance (Wm^{-2})
900
800
700
600
500
400
300
200
100
0
500 600 700 800 900 1000 1100 1200 1300 1400 1500 1600 1700 1800 1900
time (LST)

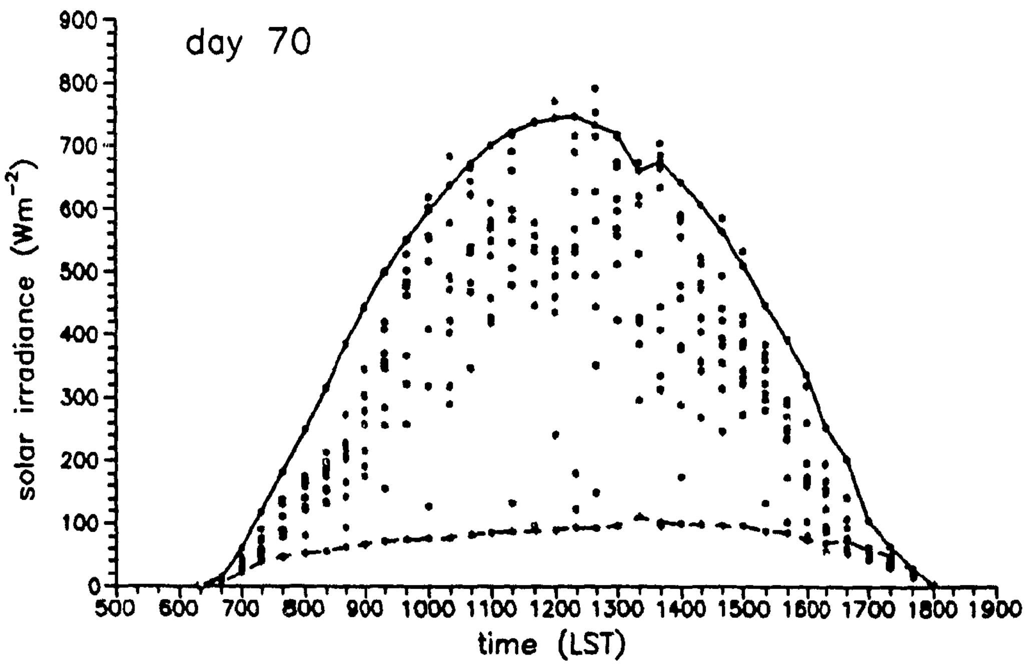
day 70
solar irradiance (Wm^{-2})
900
800
700
600
500
400
300
200
100
0
500 600 700 800 900 1000 1100 1200 1300 1400 1500 1600 1700 1800 1900
time (LST)

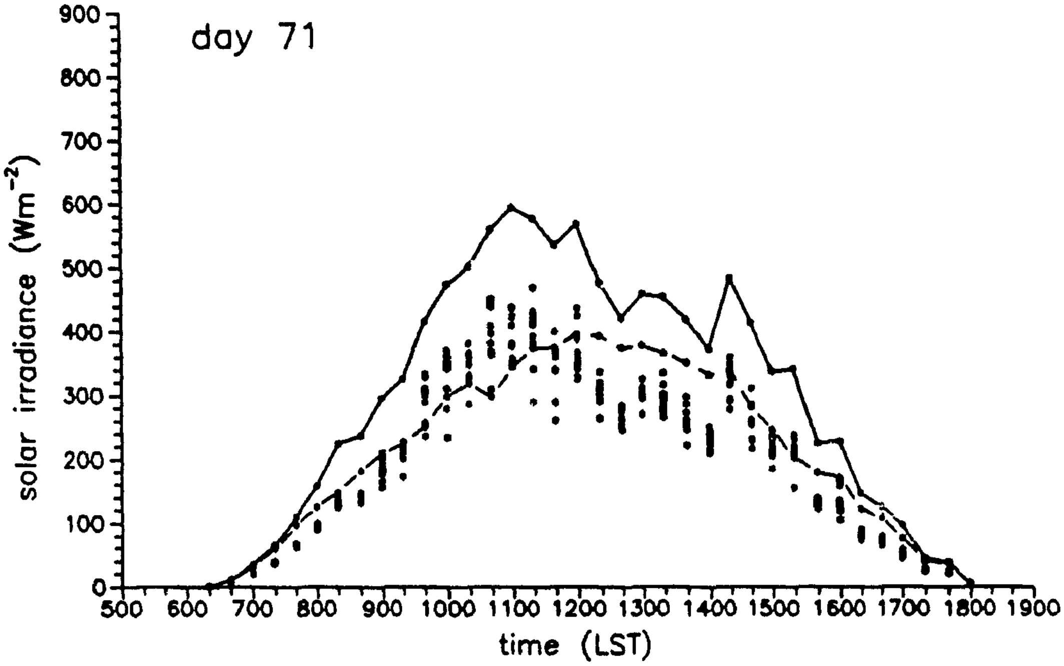
day 71
solar irradiance (Wm^{-2})
0
100
200
300
400
500
600
700
800
900
500 600 700 800 900 1000 1100 1200 1300 1400 1500 1600 1700 1800 1900
time (LST)

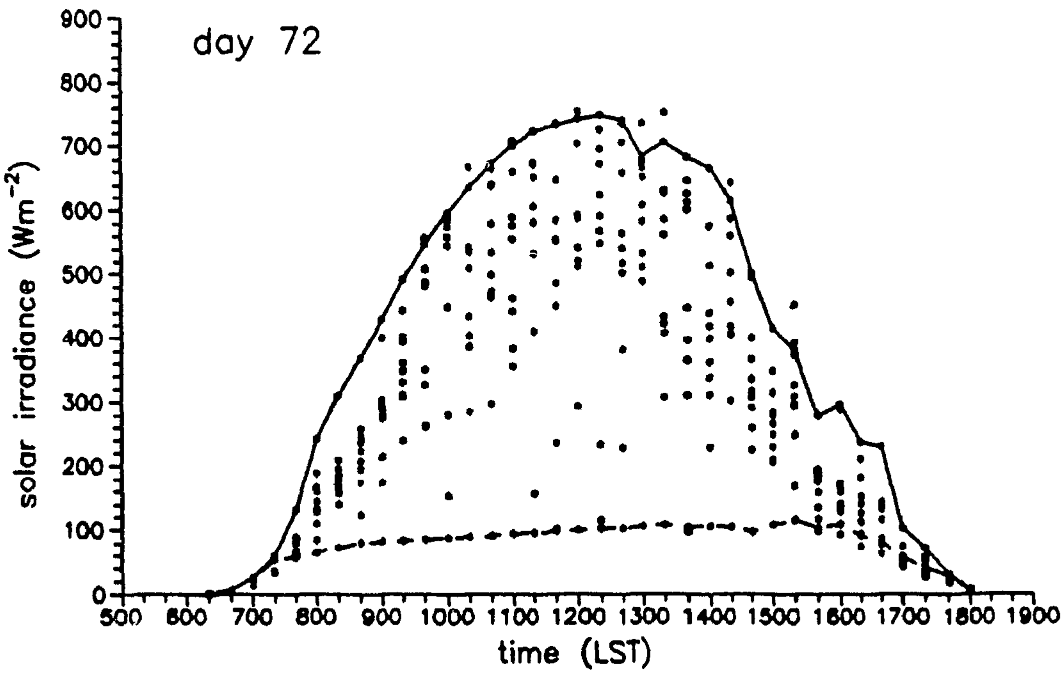
day 72
solar irradiance (Wm^{-2})
0
100
200
300
400
500
600
700
800
900
500 600 700 800 900 1000 1100 1200 1300 1400 1500 1600 1700 1800 1900
time (LST)

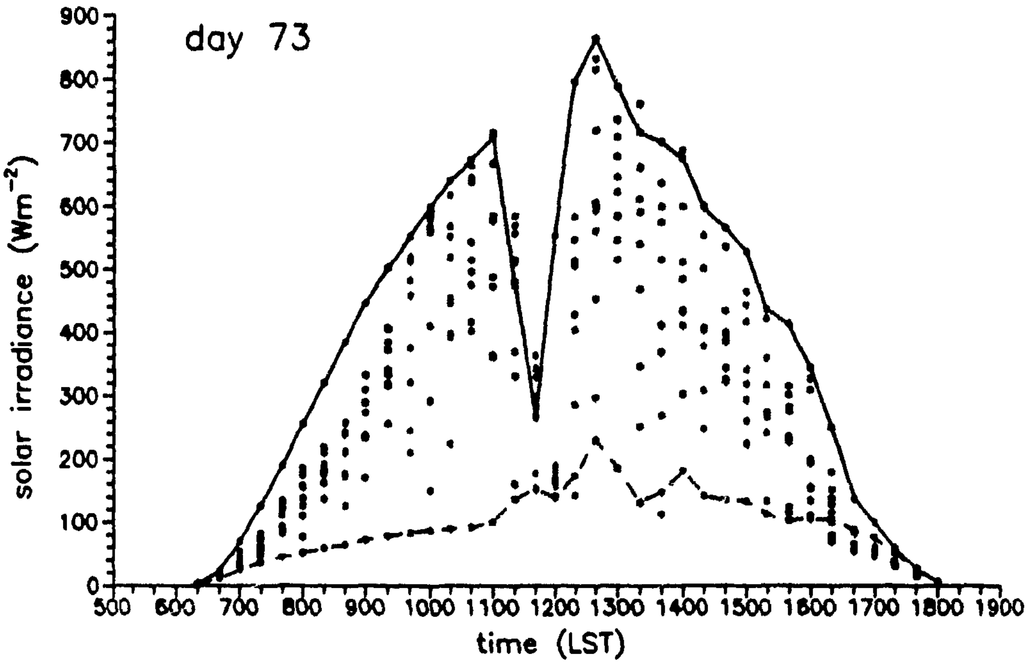
day 73
solar irradiance (Wm^{-2})
900
800
700
600
500
400
300
200
100
0
500 600 700 800 900 1000 1100 1200 1300 1400 1500 1600 1700 1800 1900
time (LST)

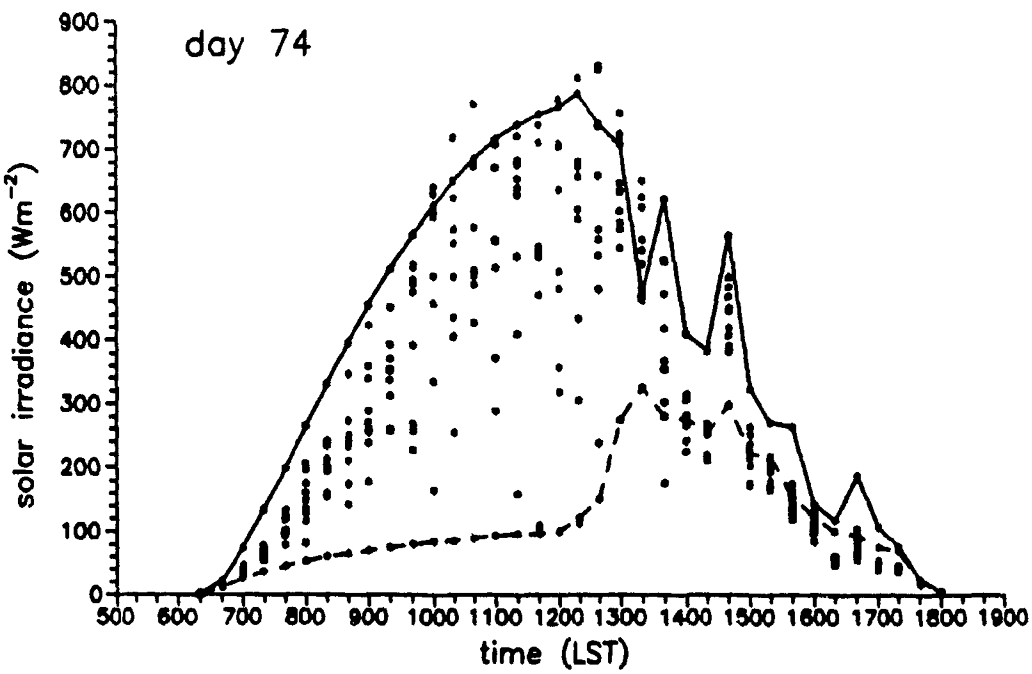
day 74
solar irradiance (Wm^{-2})
900
800
700
600
500
400
300
200
100
0
500 600 700 800 900 1000 1100 1200 1300 1400 1500 1600 1700 1800 1900
time (LST)

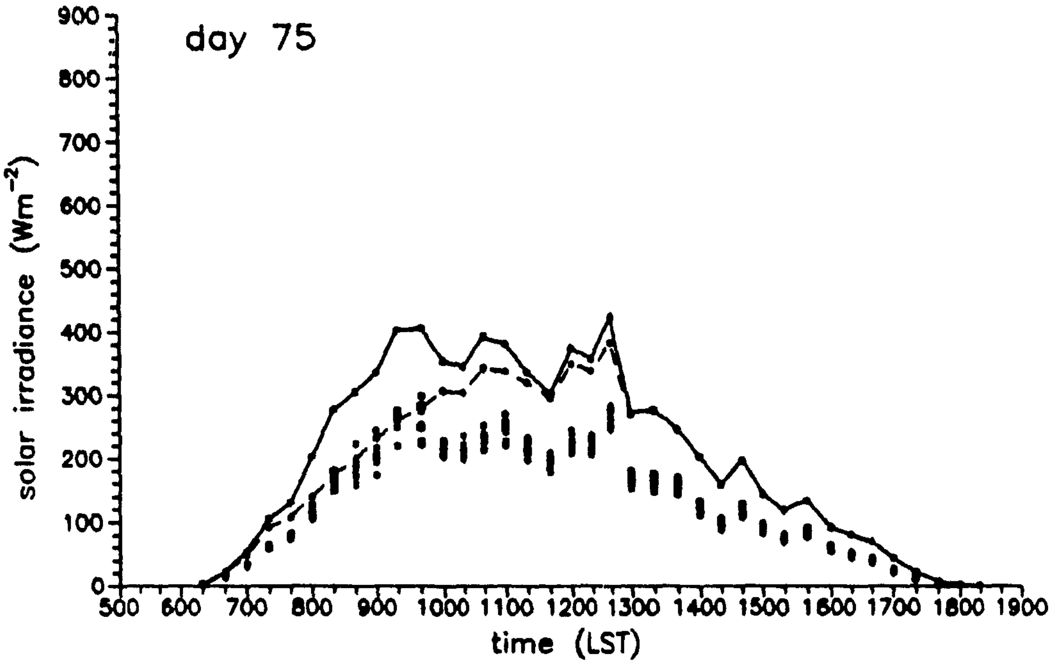
day 75
solar irradiance (Wm^{-2})
900
800
700
600
500
400
300
200
100
0
500 600 700 800 900 1000 1100 1200 1300 1400 1500 1600 1700 1800 1900
time (LST)

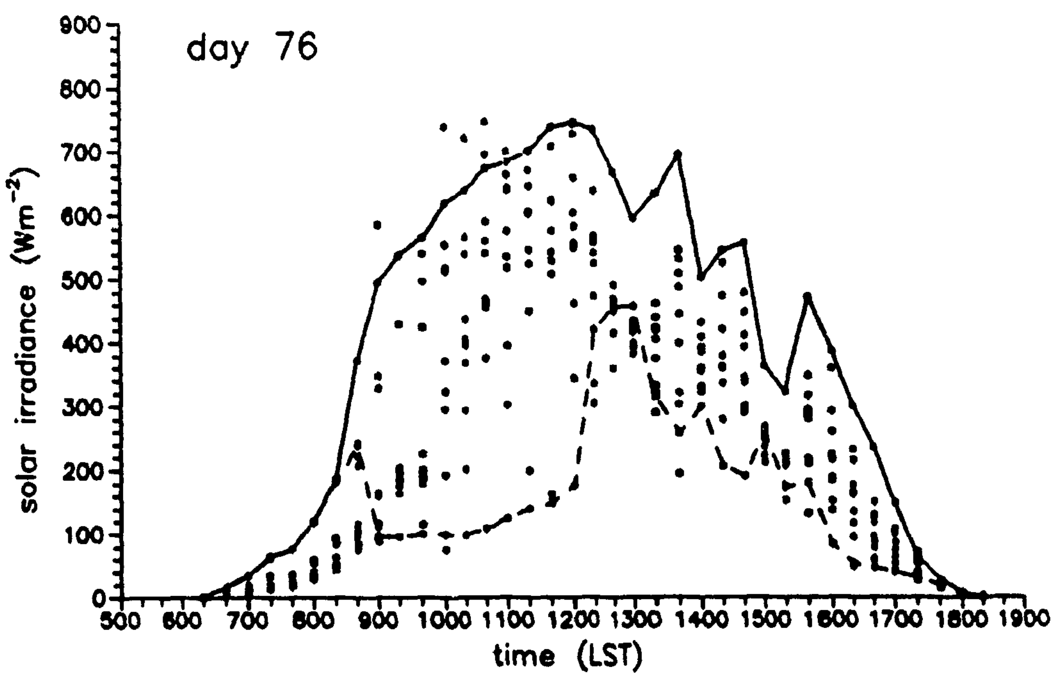
day 76
solar irradiance (Wm^{-2})
900
800
700
600
500
400
300
200
100
0
500 600 700 800 900 1000 1100 1200 1300 1400 1500 1600 1700 1800 1900
time (LST)

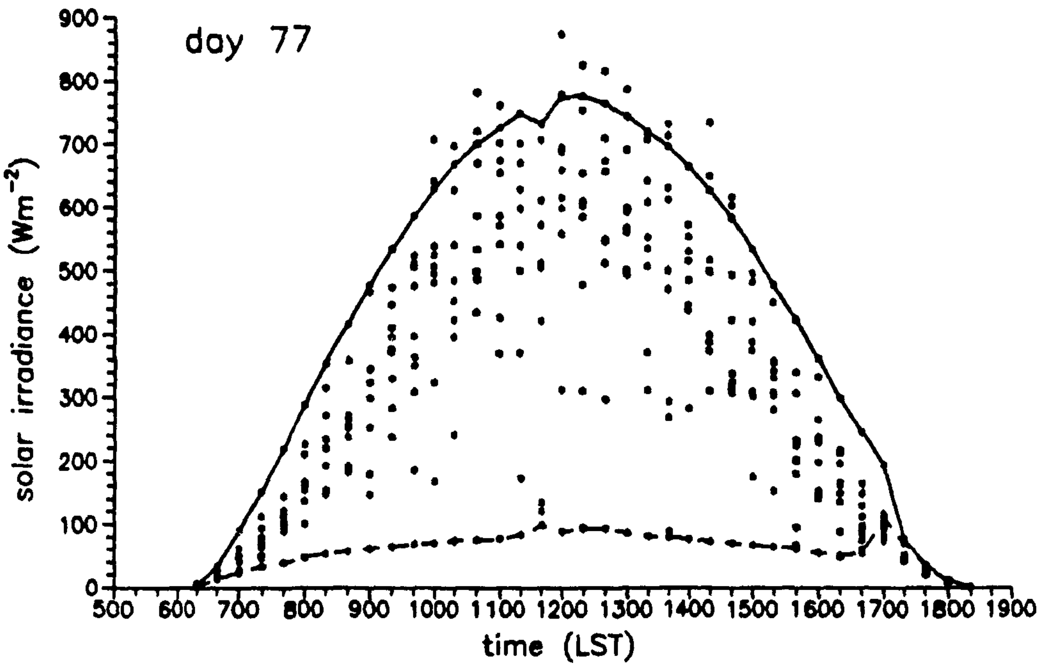
day 77
solar irradiance (Wm^{-2})
time (LST)
0
100
200
300
400
500
600
700
800
900
500 600 700 800 900 1000 1100 1200 1300 1400 1500 1600 1700 1800 1900

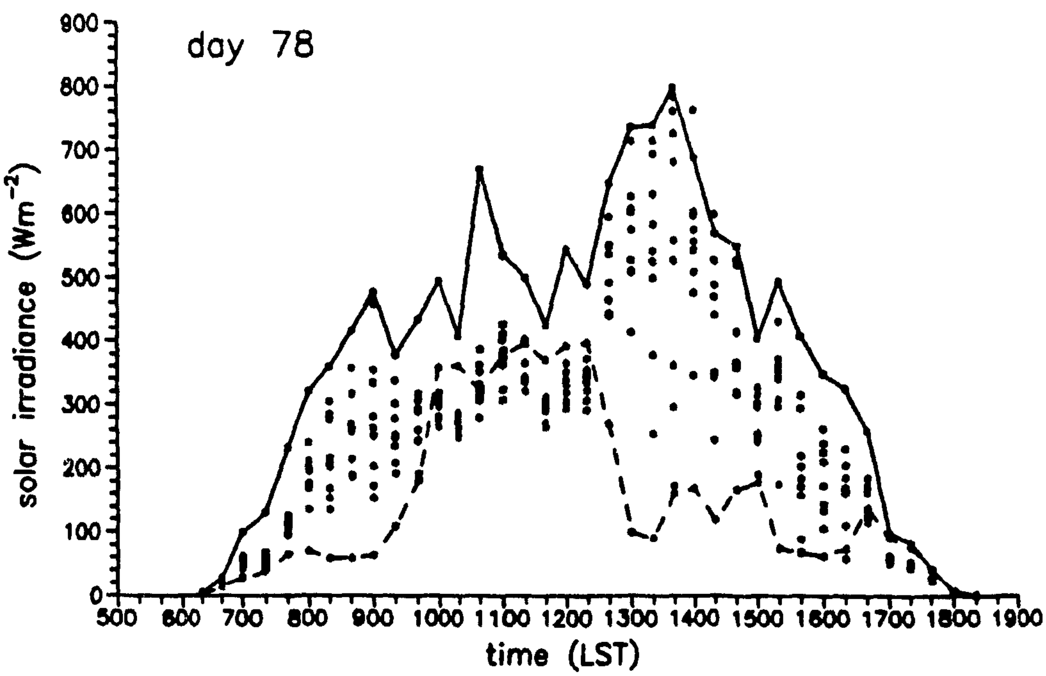
day 78
solar irradiance (Wm^{-2})
time (LST)
0
100
200
300
400
500
600
700
800
900
500 600 700 800 900 1000 1100 1200 1300 1400 1500 1600 1700 1800 1900

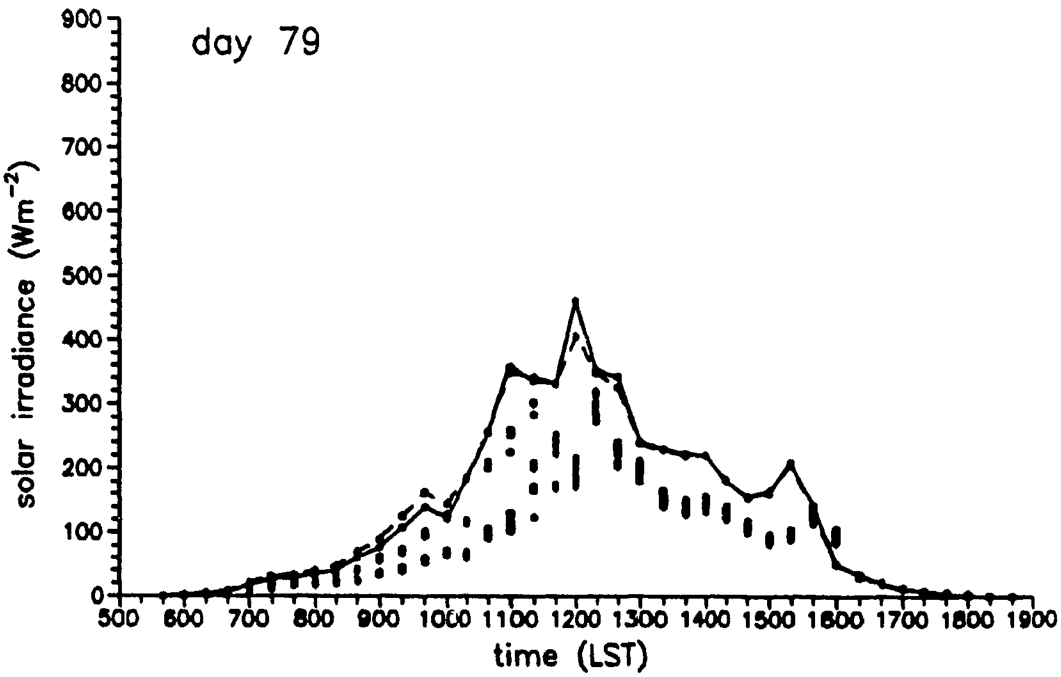

day 79
solar irradiance (Wm^{-2})
900
800
700
600
500
400
300
200
100
0
500
600
700
800
900
1000
1100
1200
1300
1400
1500
1600
1700
1800
1900
time (LST)

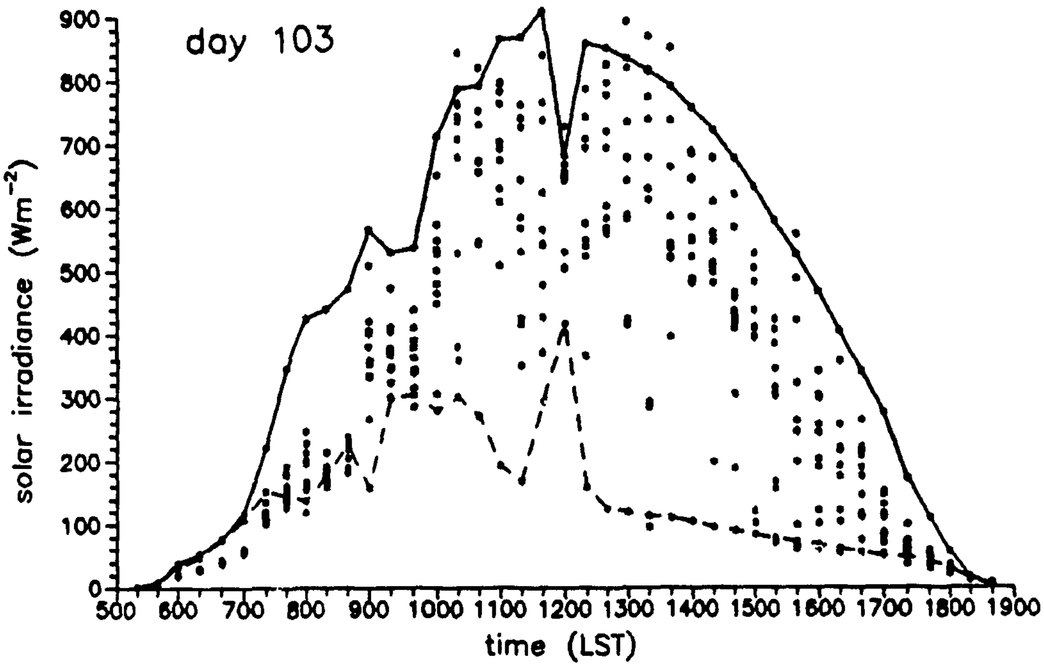
day 103
solar irradiance (Wm⁻²)
time (LST)
0
100
200
300
400
500
600
700
800
900
500 600 700 800 900 1000 1100 1200 1300 1400 1500 1600 1700 1800 1900

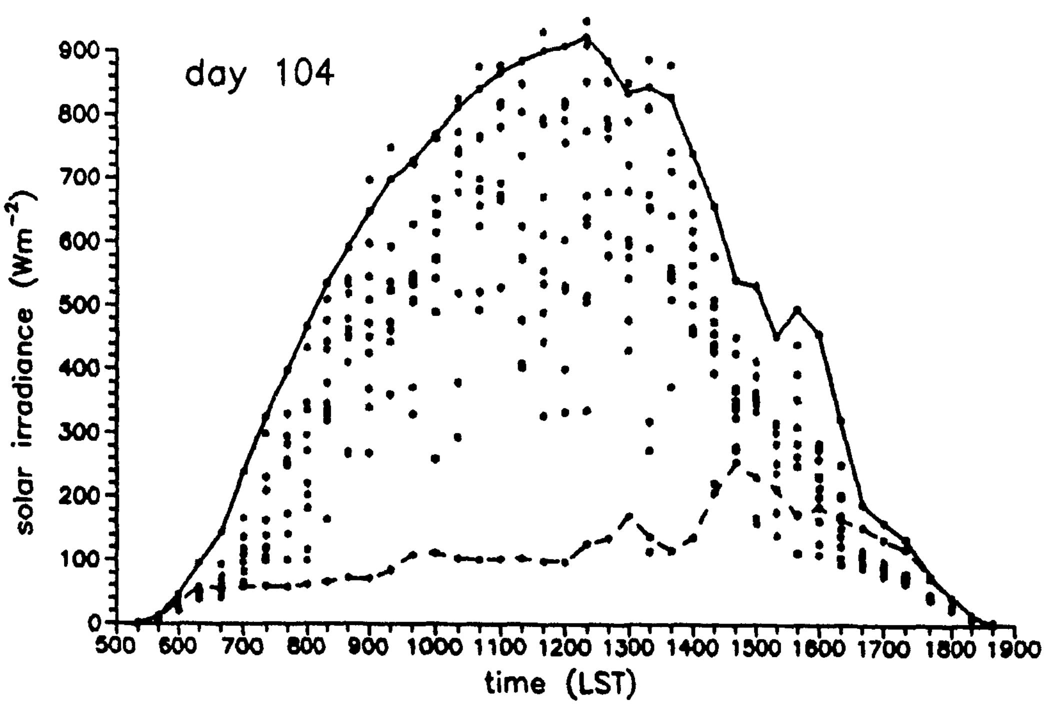
day 104
solar irradiance (Wm⁻²)
time (LST)
0
100
200
300
400
500
600
700
800
900
500 600 700 800 900 1000 1100 1200 1300 1400 1500 1600 1700 1800 1900

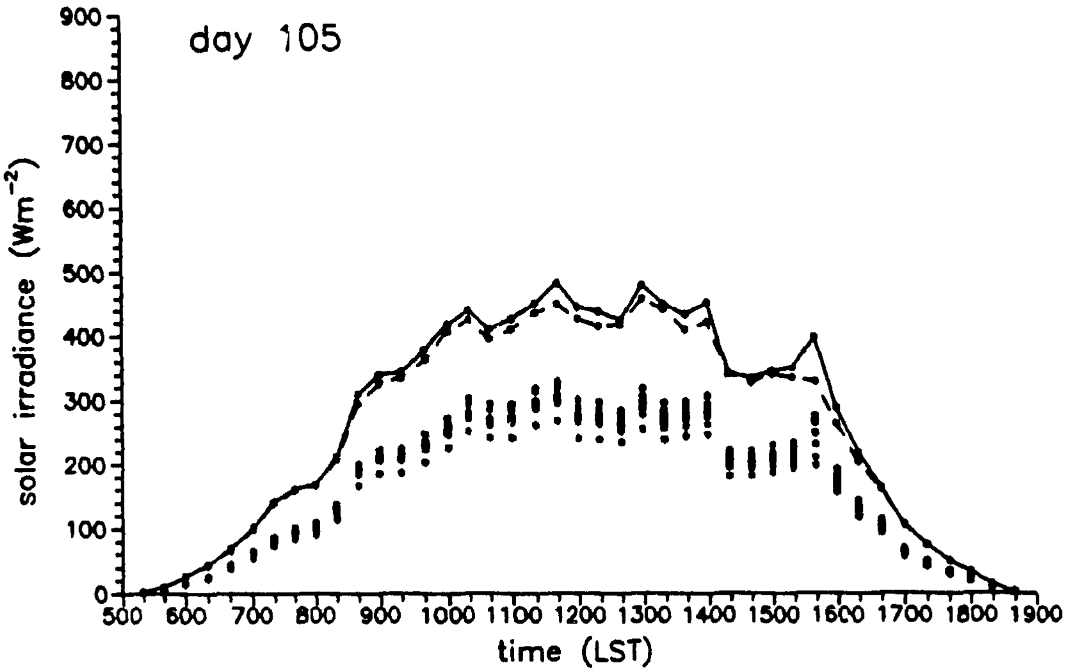
day 105
solar irradiance (Wm^{-2})
0
100
200
300
400
500
600
700
800
900
500 600 700 800 900 1000 1100 1200 1300 1400 1500 1600 1700 1800 1900
time (LST)

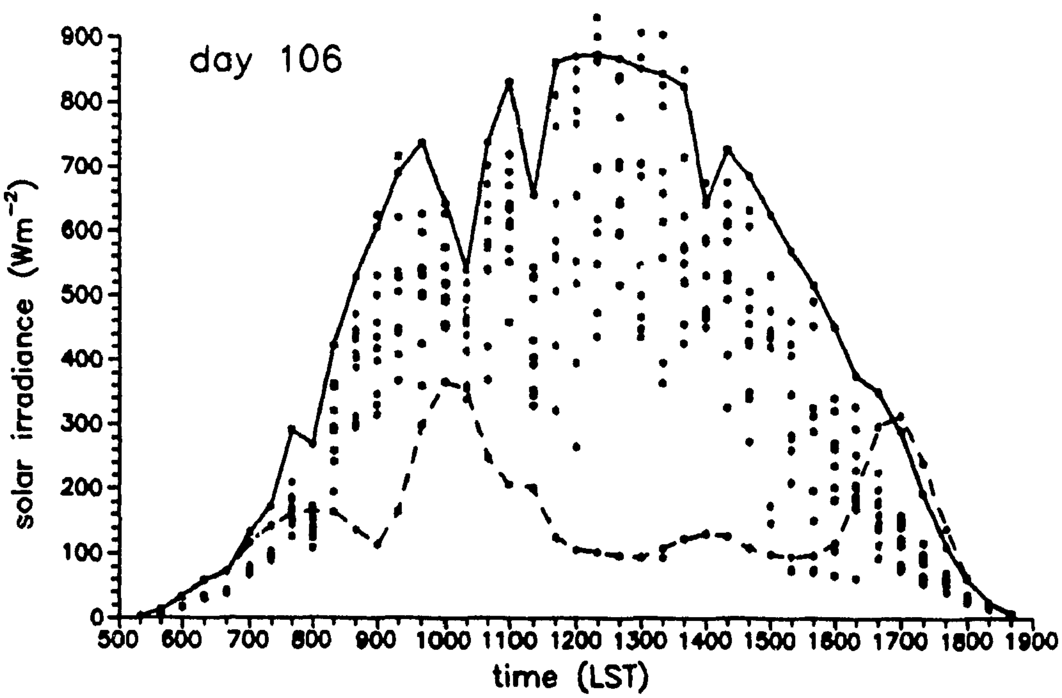
day 106
solar irradiance (Wm^{-2})
0
100
200
300
400
500
600
700
800
900
500 600 700 800 900 1000 1100 1200 1300 1400 1500 1600 1700 1800 1900
time (LST)

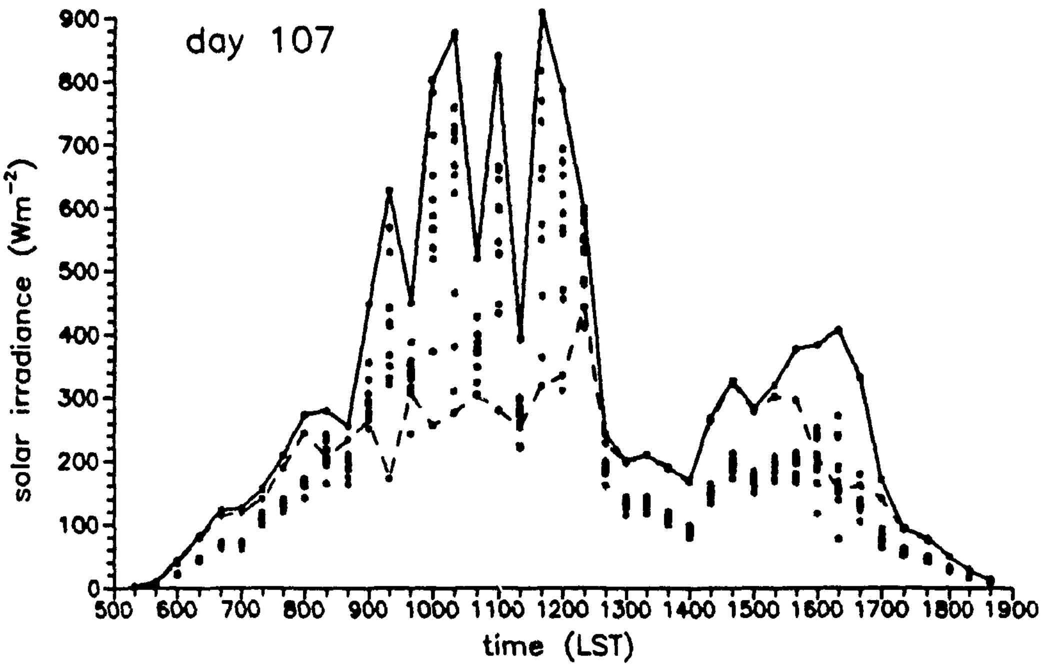

day 107
solar irradiance (Wm^{-2})
time (LST)
0
100
200
300
400
500
600
700
800
900
500
600
700
800
900
1000
1100
1200
1300
1400
1500
1600
1700
1800
1900

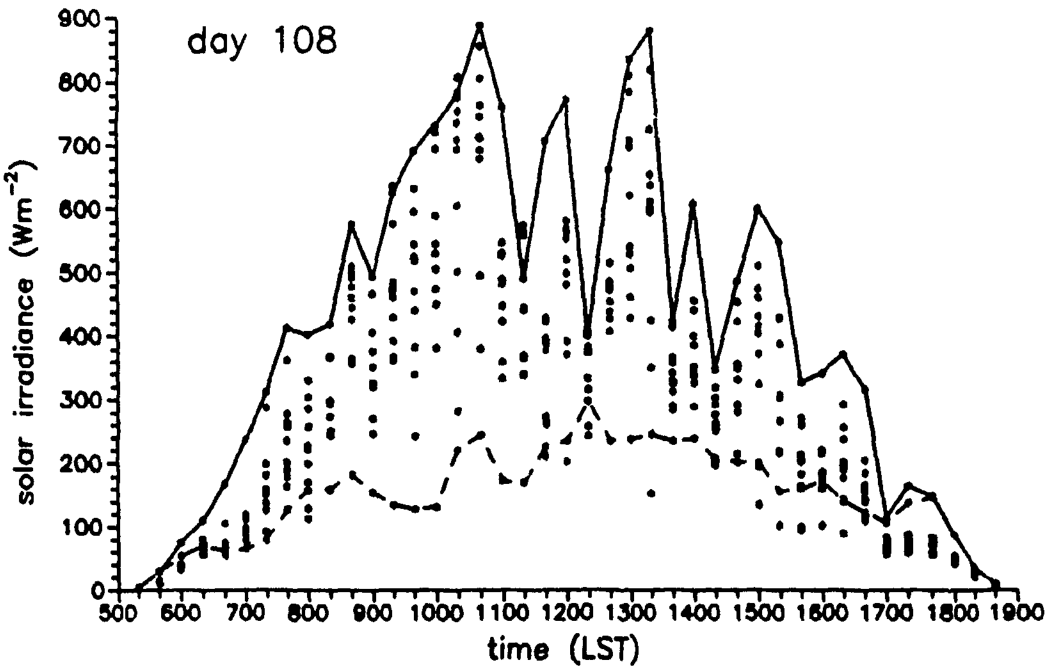

day 108
solar irradiance (Wm^{-2})
time (LST)
0
100
200
300
400
500
600
700
800
900
500
600
700
800
900
1000
1100
1200
1300
1400
1500
1600
1700
1800
1900

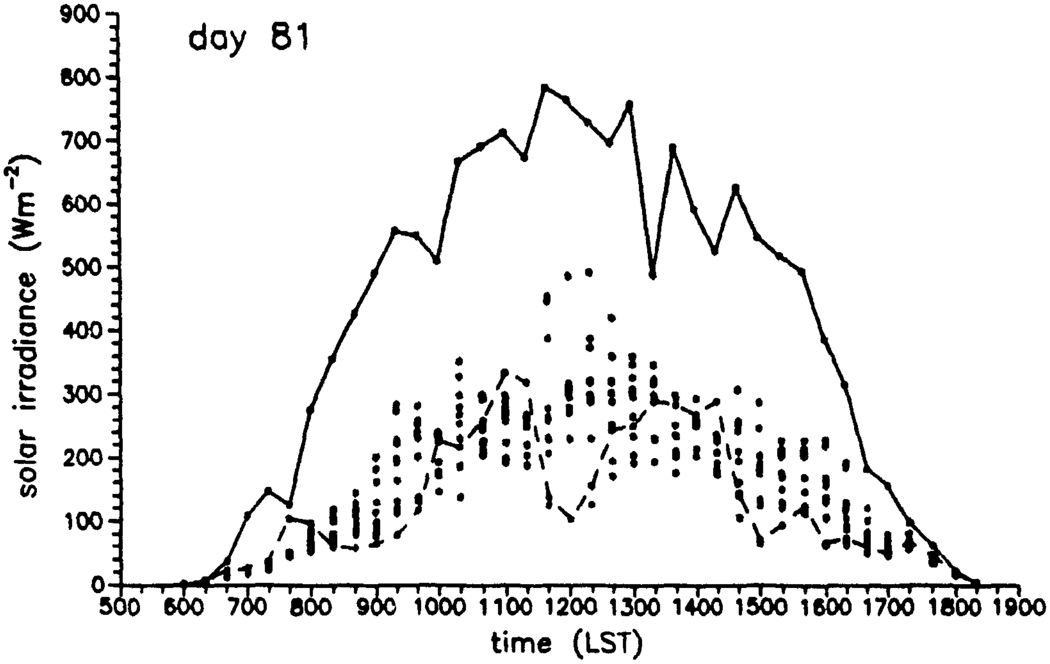
day 81
solar irradiance (Wm^{-2})
time (LST)
0
100
200
300
400
500
600
700
800
900
500 600 700 800 900 1000 1100 1200 1300 1400 1500 1600 1700 1800 1900

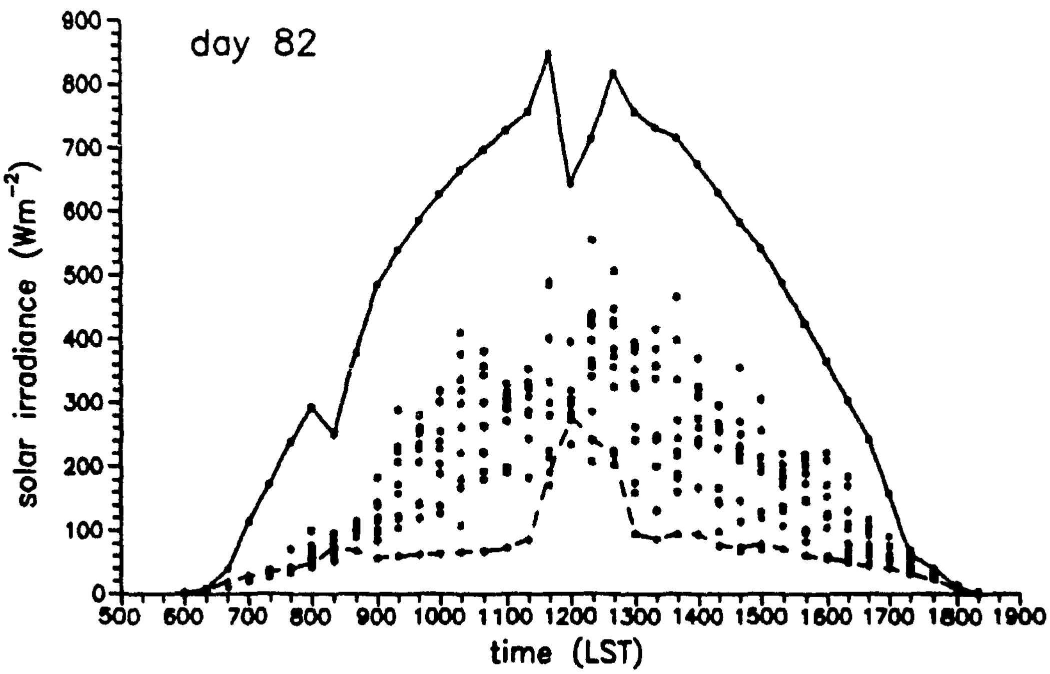
day 82
solar irradiance (Wm^{-2})
time (LST)
0
100
200
300
400
500
600
700
800
900
500 600 700 800 900 1000 1100 1200 1300 1400 1500 1600 1700 1800 1900

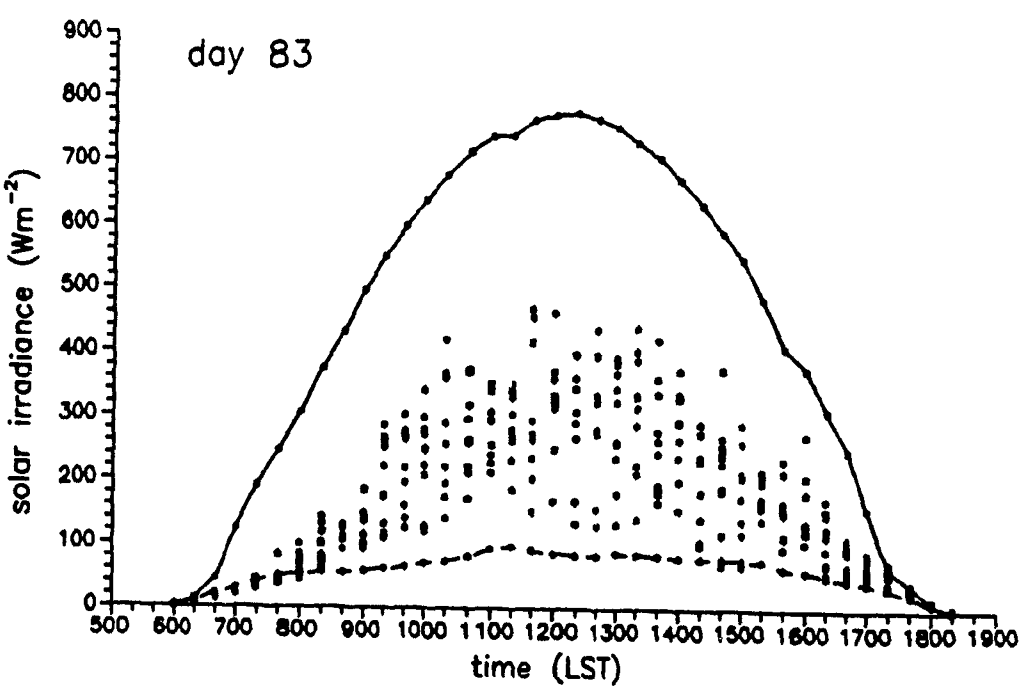

day 83
solar irradiance (Wm^{-2})
900
800
700
600
500
400
300
200
100
0
500 600 700 800 900 1000 1100 1200 1300 1400 1500 1600 1700 1800 1900
time (LST)

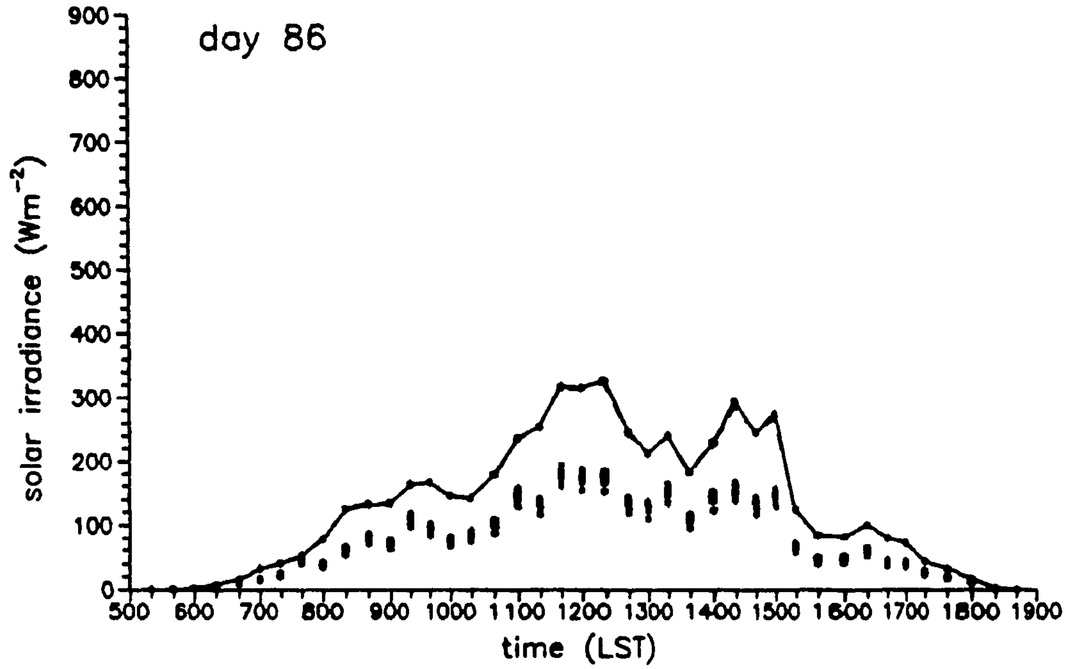
day 86
solar irradiance (Wm^{-2})
time (LST)
0
100
200
300
400
500
600
700
800
900
500
600
700
800
900
1000
1100
1200
1300
1400
1500
1600
1700
1800
1900

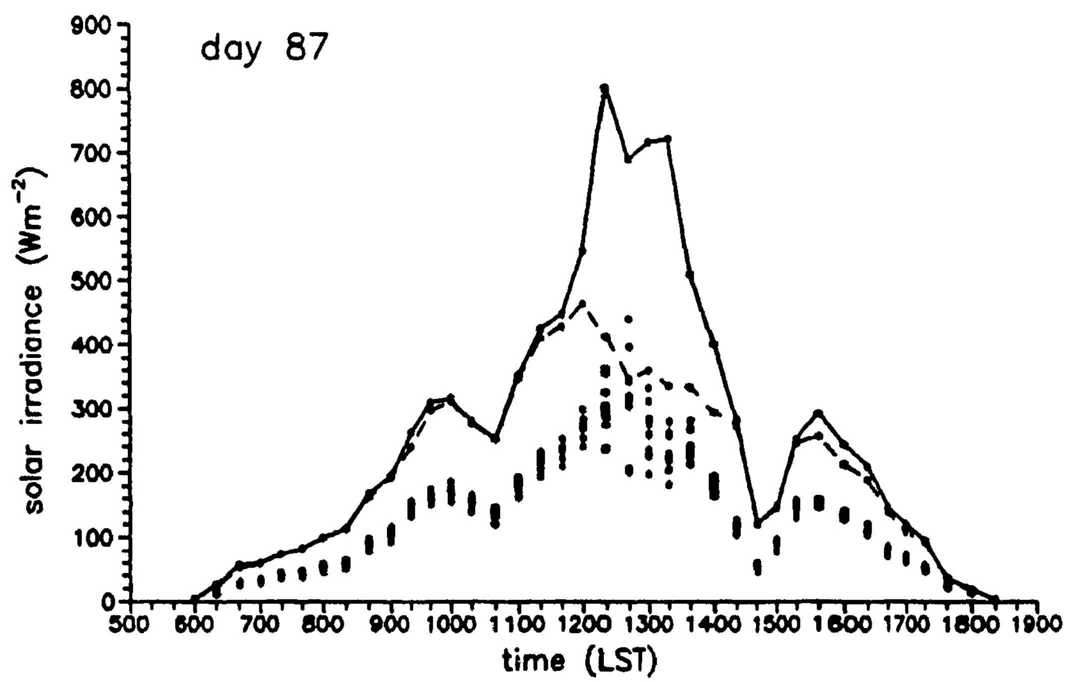
day 87
solar irradiance (Wm^{-2})
time (LST)
0
100
200
300
400
500
600
700
800
900
500
600
700
800
900
1000
1100
1200
1300
1400
1500
1600
1700
1800
1900

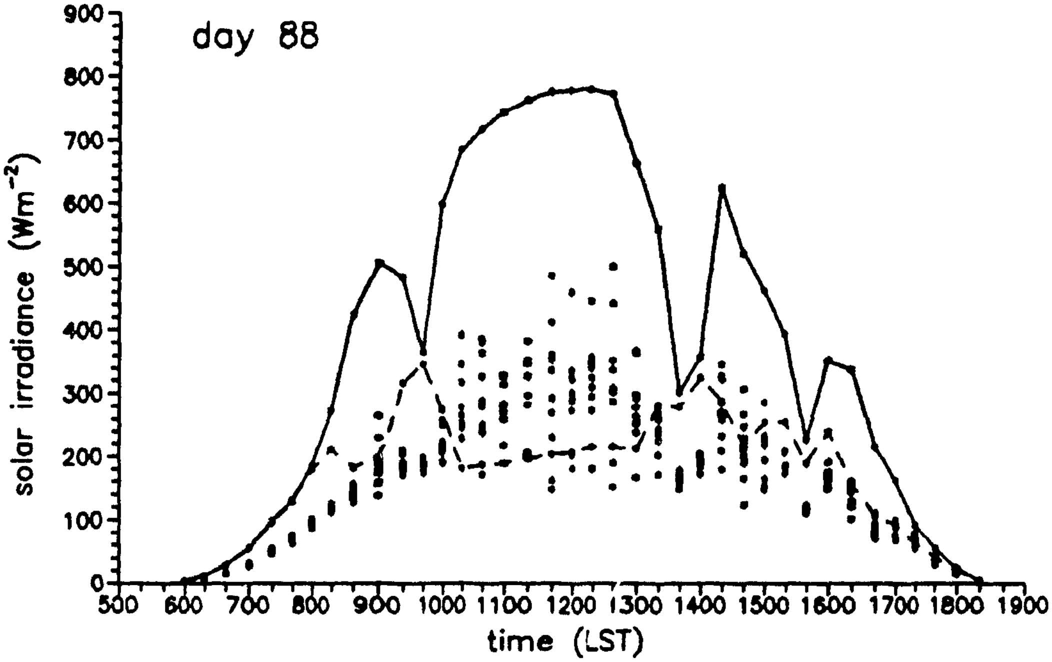
day 88
solar irradiance (Wm^{-2})
time (LST)
0
100
200
300
400
500
600
700
800
900
500
600
700
800
900
1000
1100
1200
1300
1400
1500
1600
1700
1800
1900

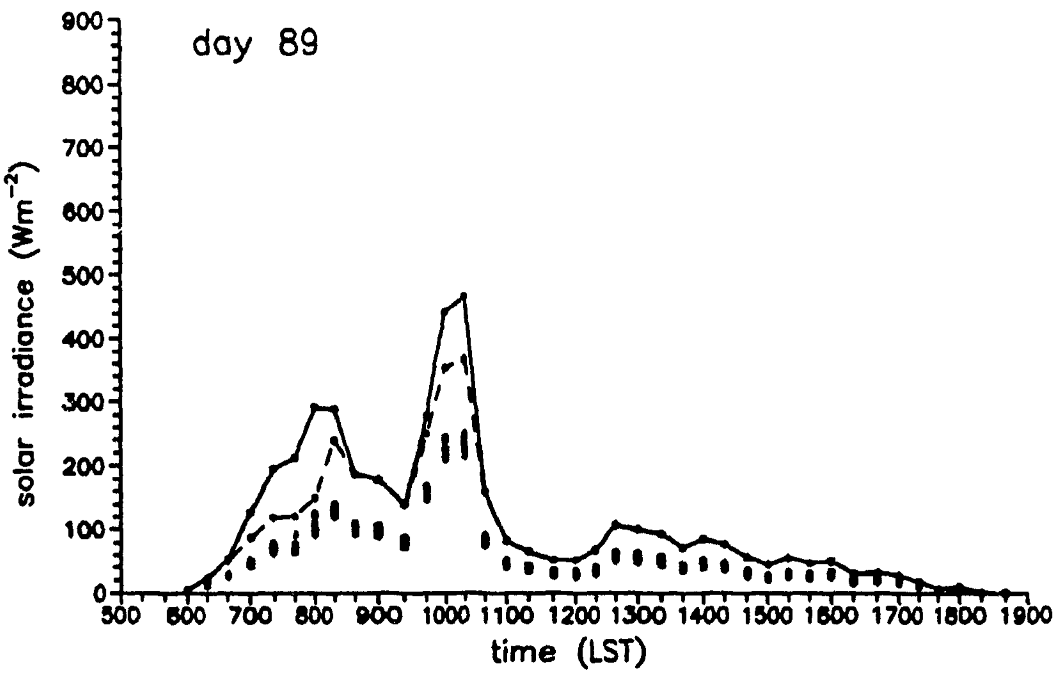
day 89
solar irradiance (Wm^{-2})
time (LST)
0
100
200
300
400
500
600
700
800
900
500
600
700
800
900
1000
1100
1200
1300
1400
1500
1600
1700
1800
1900

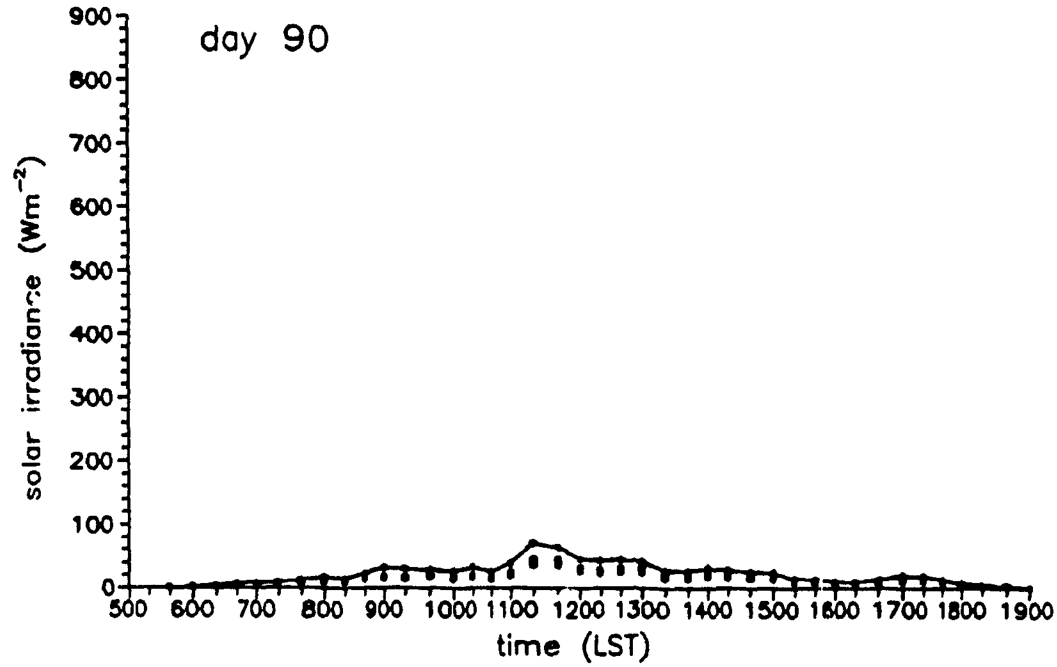
day 90
solar irradiance (Wm^{-2})
0
100
200
300
400
500
600
700
800
900
500 600 700 800 900 1000 1100 1200 1300 1400 1500 1600 1700 1800 1900
time (LST)

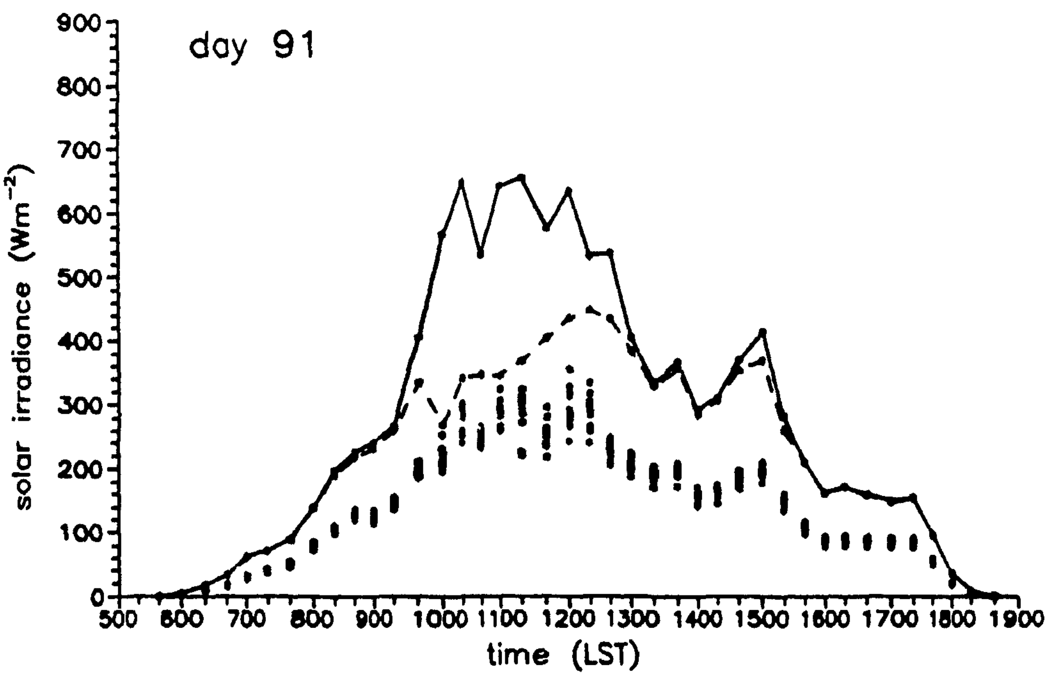
day 91
solar irradiance (Wm^{-2})
0
100
200
300
400
500
600
700
800
900
500 600 700 800 900 1000 1100 1200 1300 1400 1500 1600 1700 1800 1900
time (LST)

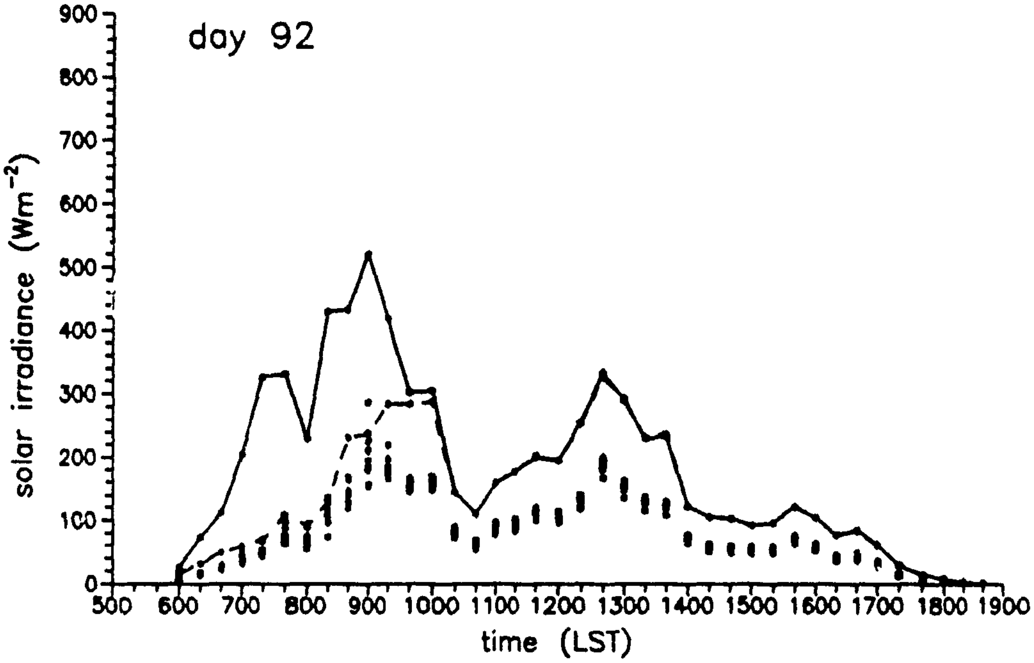
day 92
solar irradiance (Wm^{-2})
time (LST)
0
100
200
300
400
500
600
700
800
900
500
600
700
800
900
1000
1100
1200
1300
1400
1500
1600
1700
1800
1900

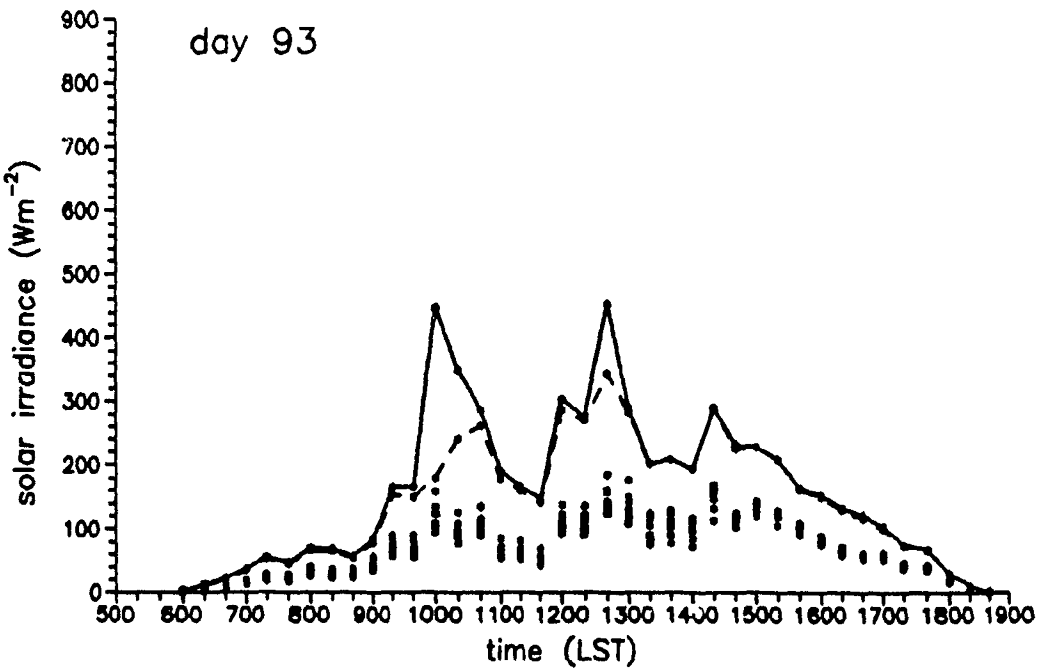
day 93
solar irradiance (Wm^{-2})
time (LST)
0
100
200
300
400
500
600
700
800
900
500
600
700
800
900
1000
1100
1200
1300
1400
1500
1600
1700
1800
1900

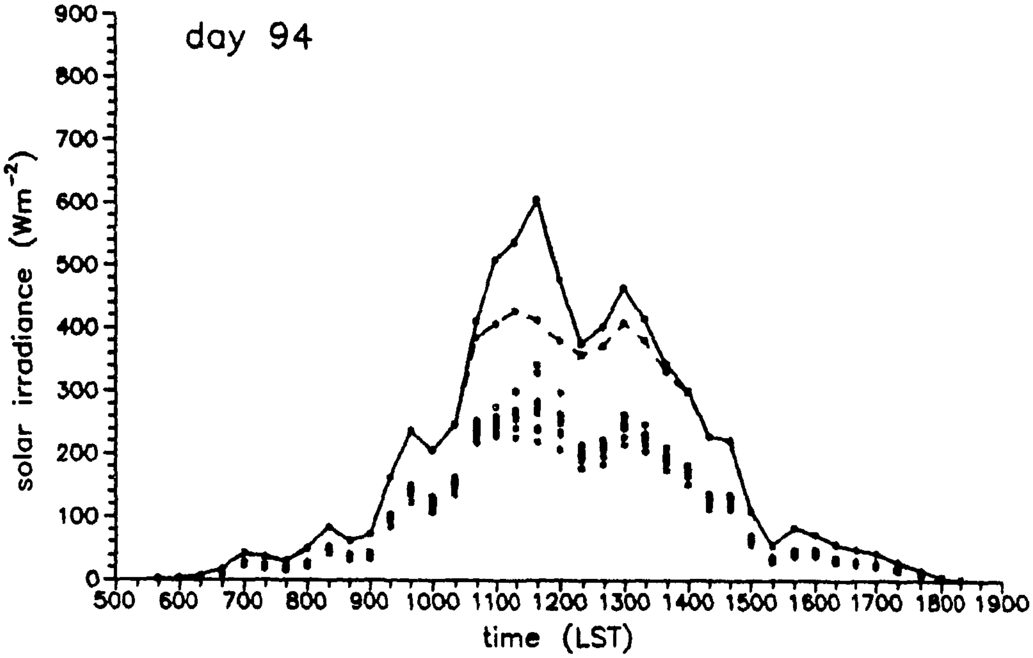
day 94
solar irradiance (Wm^{-2})
900
800
700
600
500
400
300
200
100
0
500 600 700 800 900 1000 1100 1200 1300 1400 1500 1600 1700 1800 1900
time (LST)

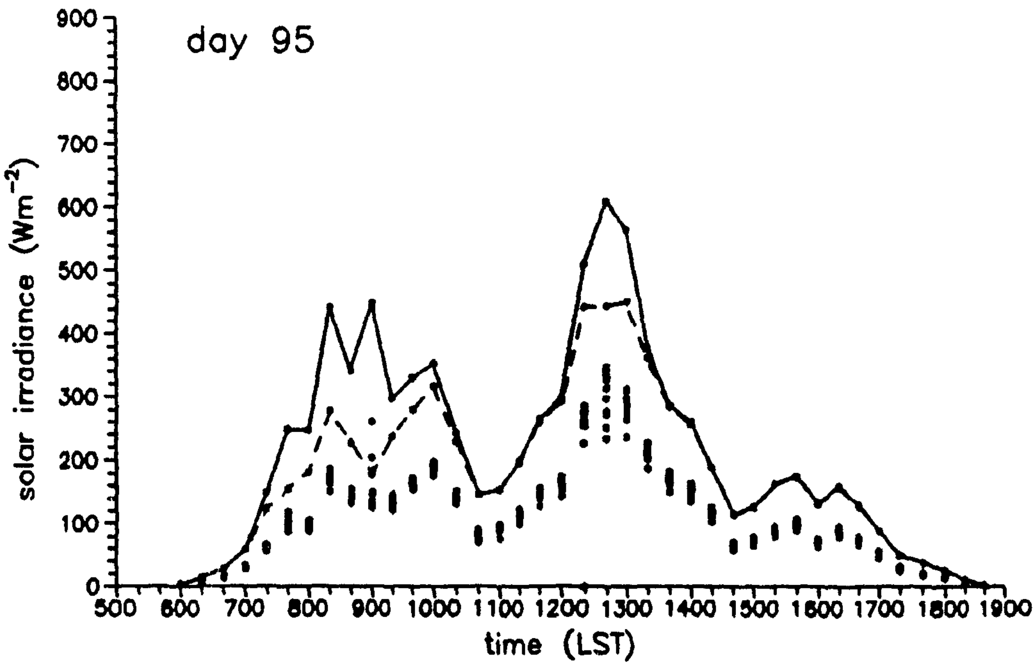
day 95
solar irradiance (Wm^{-2})
900
800
700
600
500
400
300
200
100
0
500 600 700 800 900 1000 1100 1200 1300 1400 1500 1600 1700 1800 1900
time (LST)

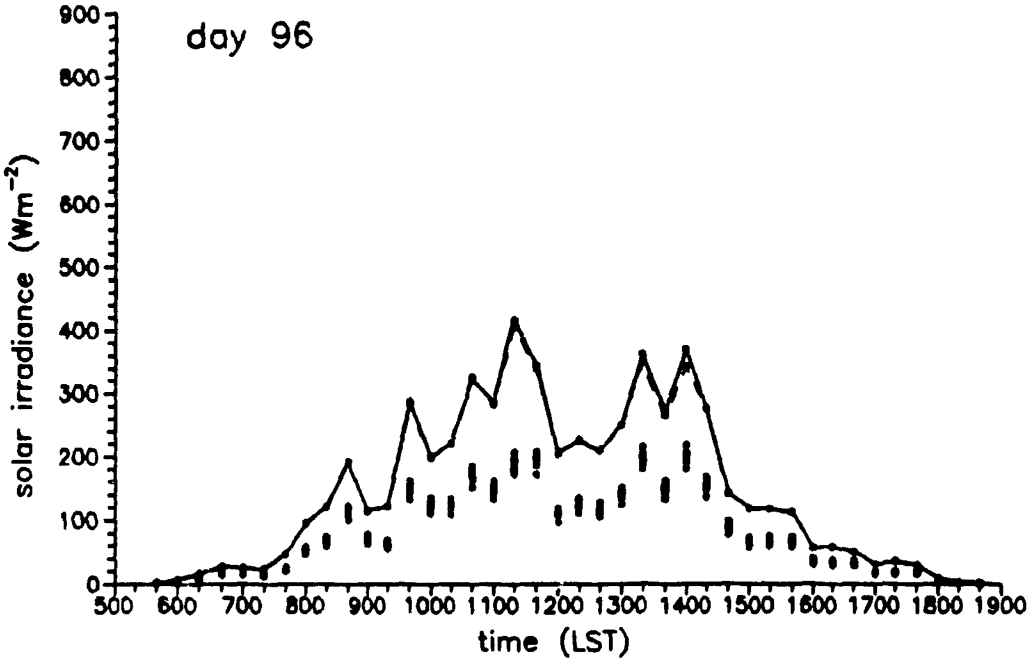
day 96
solar irradiance (Wm⁻²)
time (LST)
0
100
200
300
400
500
600
700
800
900
500
600
700
800
900
1000
1100
1200
1300
1400
1500
1600
1700
1800
1900

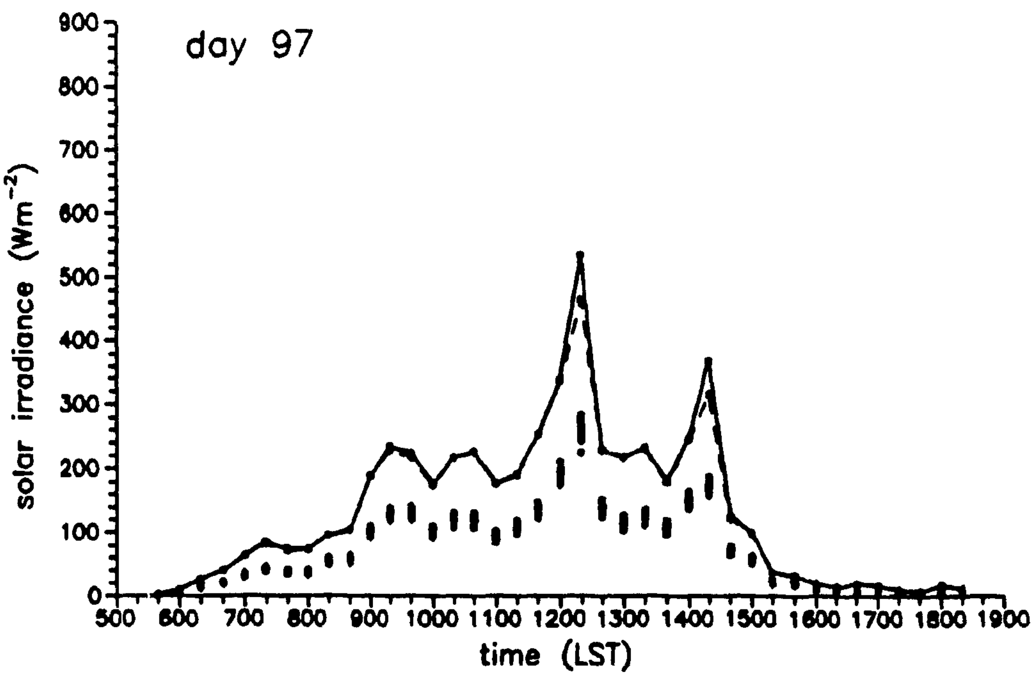
day 97
solar irradiance (Wm⁻²)
time (LST)
0
100
200
300
400
500
600
700
800
900
500
600
700
800
900
1000
1100
1200
1300
1400
1500
1600
1700
1800
1900

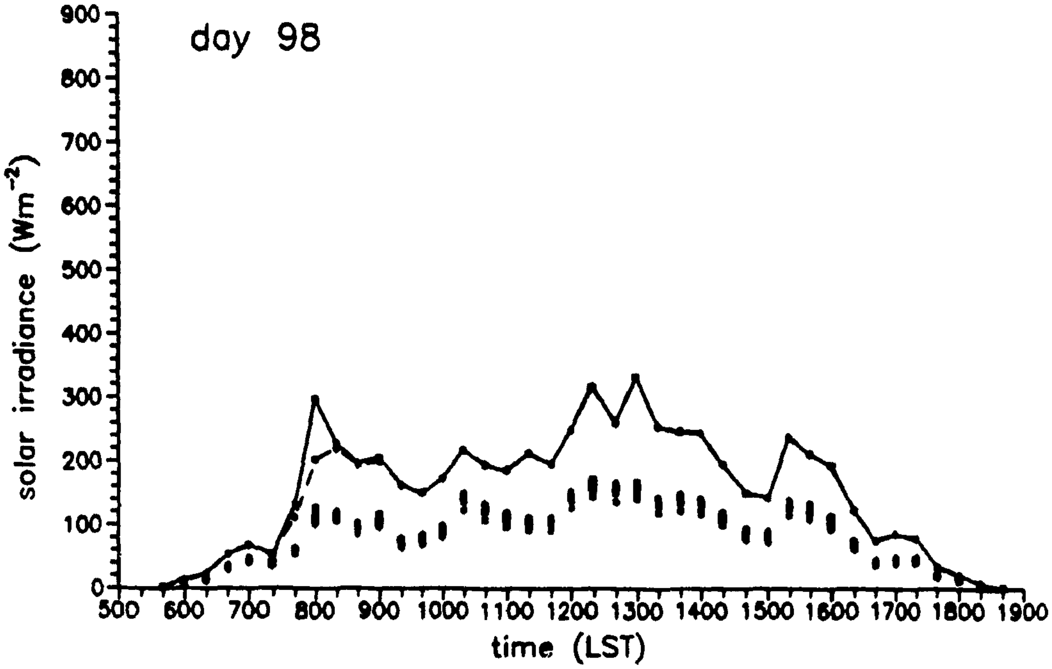
day 98
solar irradiance (Wm^{-2})
900
800
700
600
500
400
300
200
100
0
500 600 700 800 900 1000 1100 1200 1300 1400 1500 1600 1700 1800 1900
time (LST)

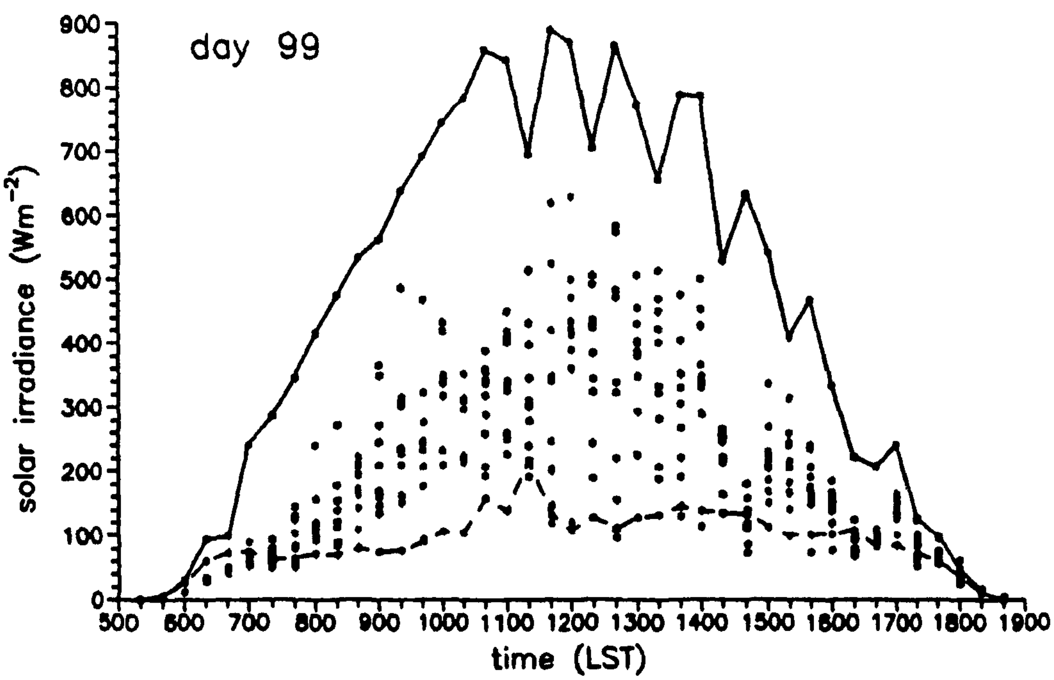
day 99
solar irradiance (Wm^{-2})
900
800
700
600
500
400
300
200
100
0
500 600 700 800 900 1000 1100 1200 1300 1400 1500 1600 1700 1800 1900
time (LST)

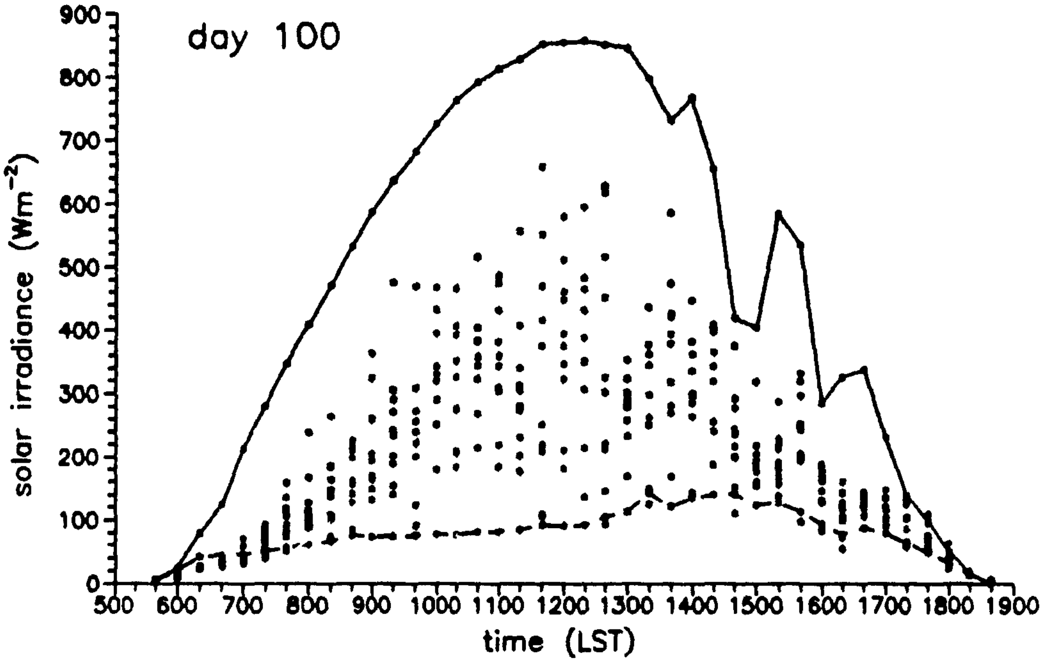
day 100
solar irradiance (Wm^-2)
time (LST)

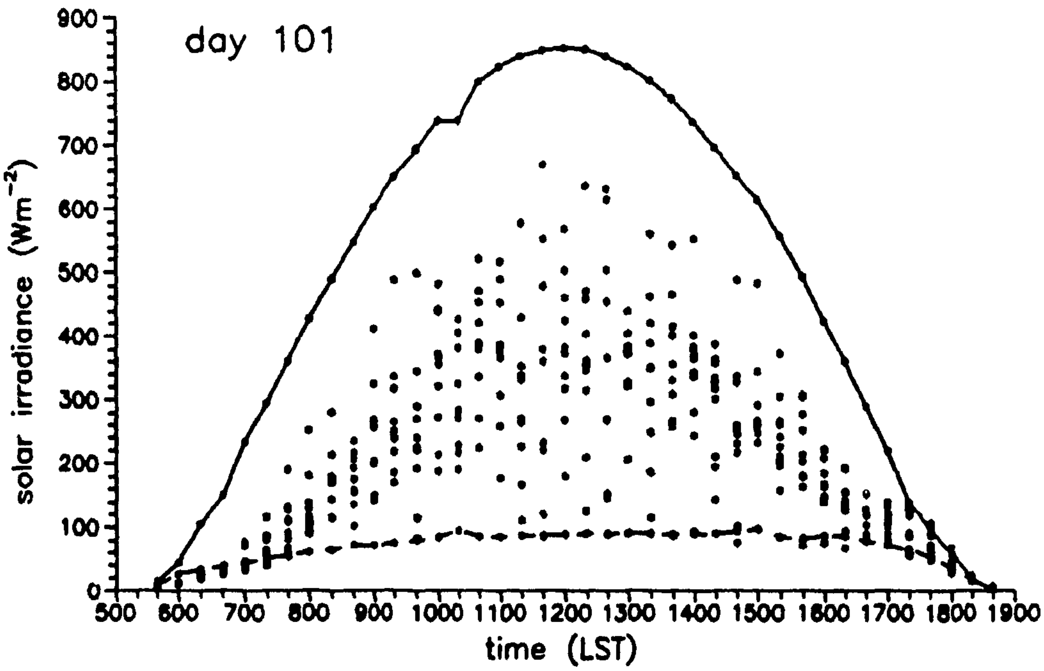
day 101
solar irradiance (Wm^-2)
time (LST)

APPENDIX C

PREDICTED AND OBSERVED SOLAR IRRADIANCE TIME-SERIES

Time-series of predicted and observed solar irradiance values are given for each day of the verification data sets. Graphs are presented first for site 1, then for site 2. Predicted and observed values (20-minute averages of instantaneous values) are shown as solid and dashed lines connecting data points, respectively. Global and diffuse irradiance above the canopy are also shown for reference as dashed and dotted traces without data points. Day numbers are given for the day of the year at the top left of each graph. Missing or shortened traces are due to elimination of some data because of unsatisfactory adjustment of the shadow band. Note that the scale on the axis of the dependent variable (y-axis) is not constant for all days at site 2, specifically for days 90, 92, 93 and 97.

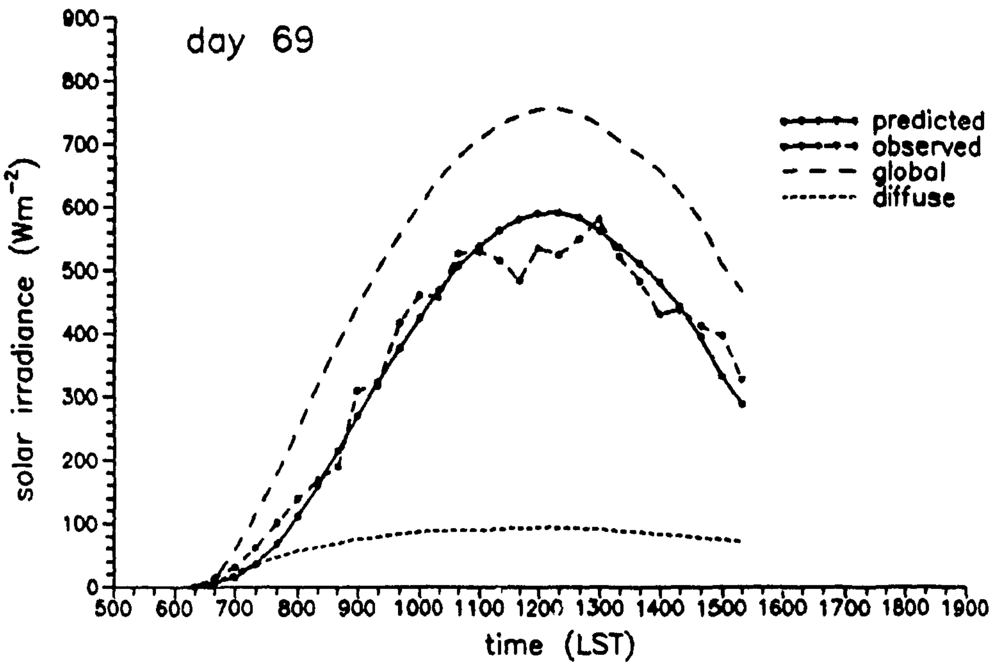
day 69
predicted
observed
global
diffuse
solar irradiance (Wm^{-2})
time (LST)
0
100
200
300
400
500
600
700
800
900
500
600
700
800
900
1000
1100
1200
1300
1400
1500
1600
1700
1800
1900

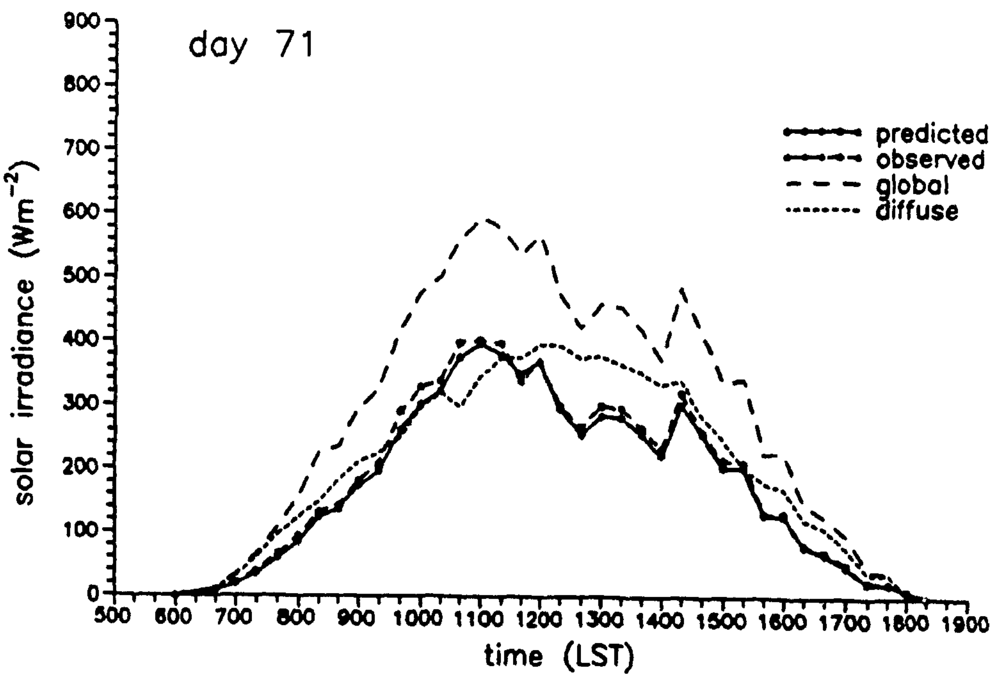
day 71
predicted
observed
global
diffuse
solar irradiance (Wm^{-2})
time (LST)
0
100
200
300
400
500
600
700
800
900
500
600
700
800
900
1000
1100
1200
1300
1400
1500
1600
1700
1800
1900

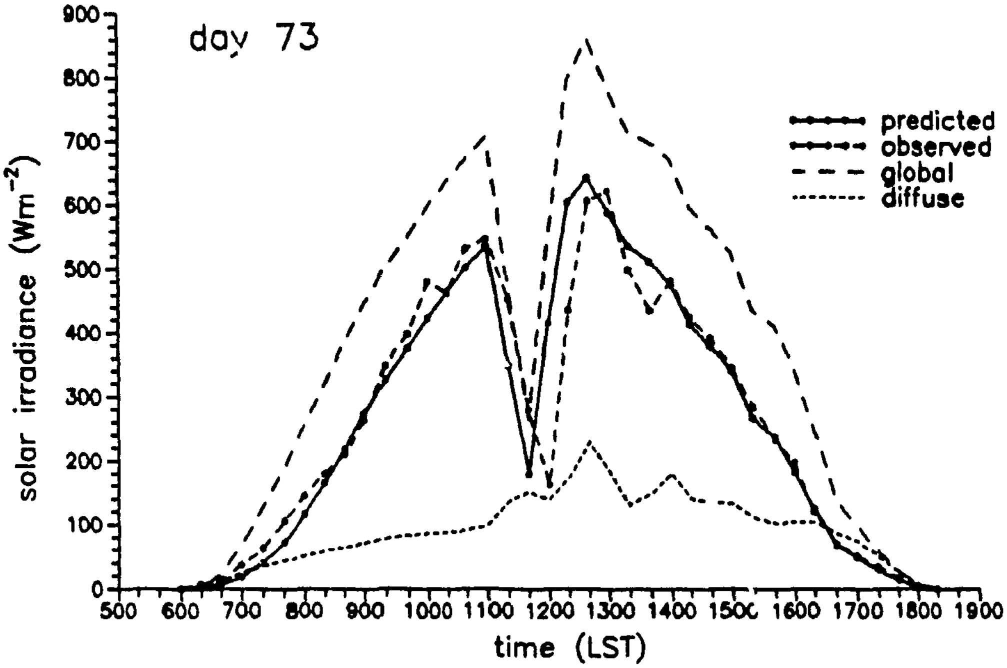
day 73
predicted
observed
global
diffuse
solar irradiance (Wm^{-2})
time (LST)

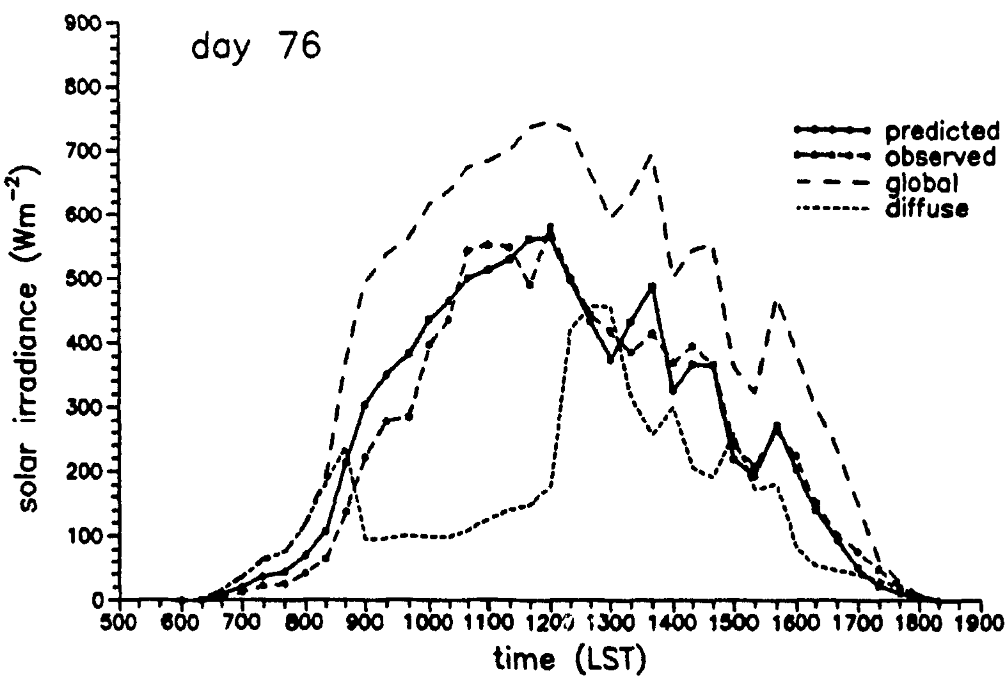
day 76
predicted
observed
global
diffuse
solar irradiance (Wm^{-2})
time (LST)

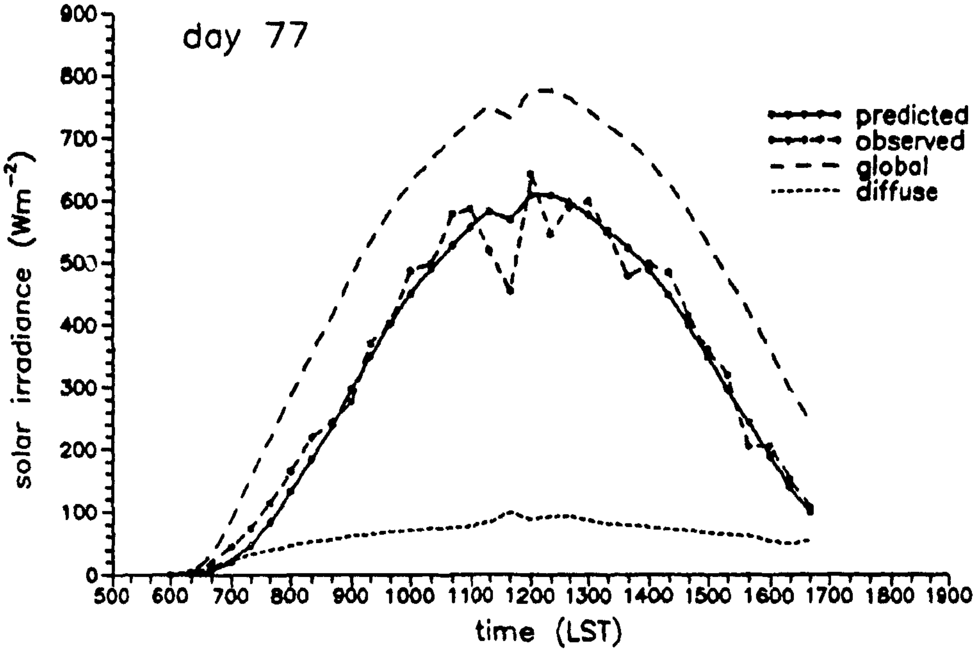
day 77
predicted
observed
global
diffuse
solar irradiance (Wm^{-2})
time (LST)
0
100
200
300
400
500
600
700
800
900
500
600
700
800
900
1000
1100
1200
1300
1400
1500
1600
1700
1800
1900

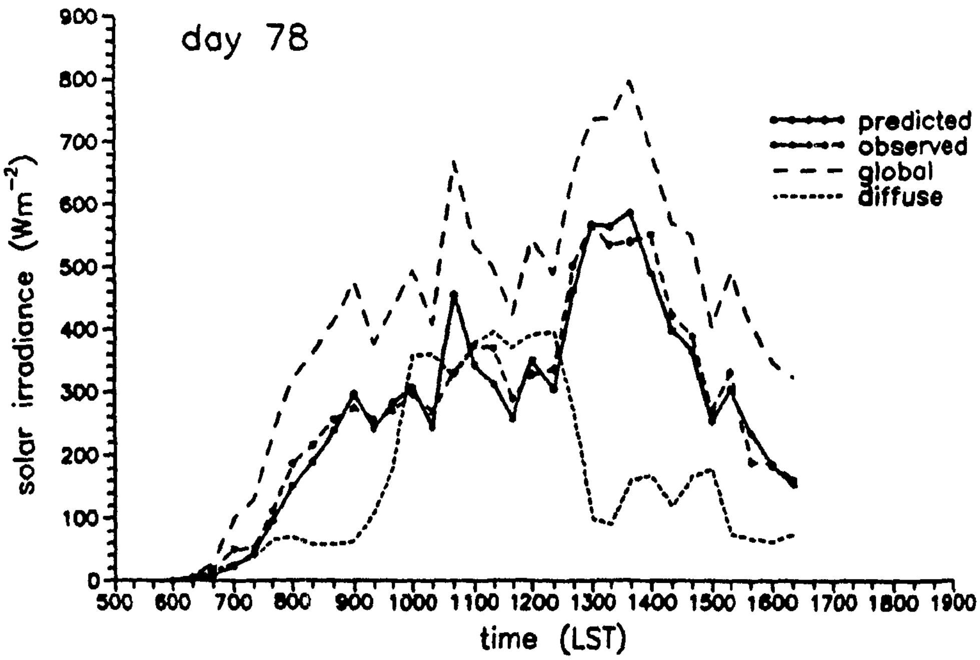
day 78
predicted
observed
global
diffuse
solar irradiance (Wm^{-2})
time (LST)
0
100
200
300
400
500
600
700
800
900
500
600
700
800
900
1000
1100
1200
1300
1400
1500
1600
1700
1800
1900

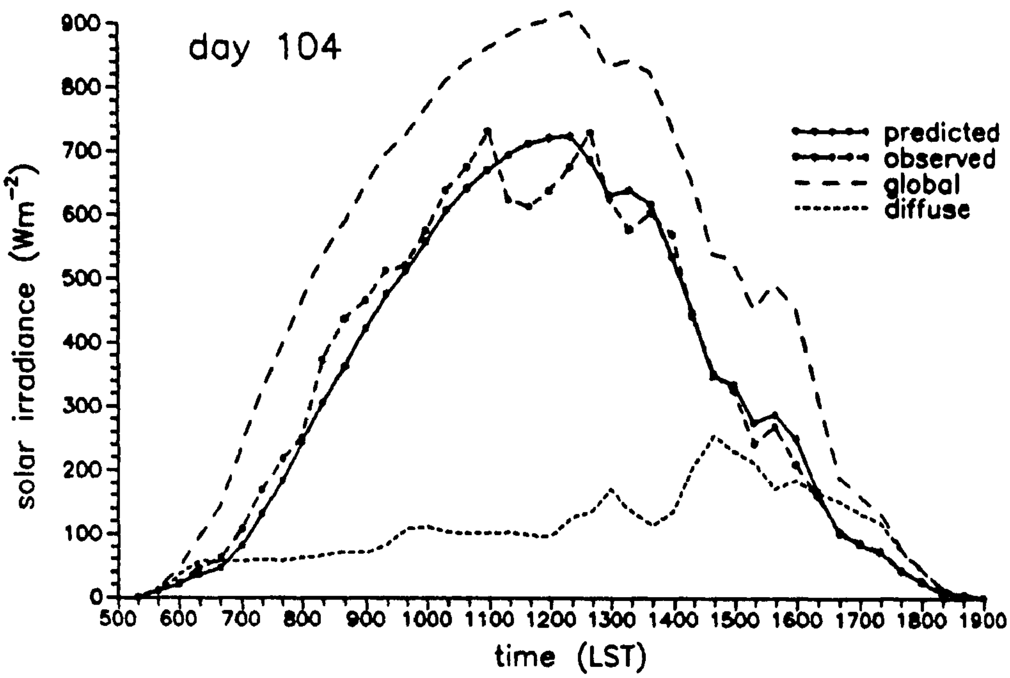
day 104
predicted
observed
global
diffuse
solar irradiance (Wm^-2)
time (LST)
0
100
200
300
400
500
600
700
800
900
500 600 700 800 900 1000 1100 1200 1300 1400 1500 1600 1700 1800 1900

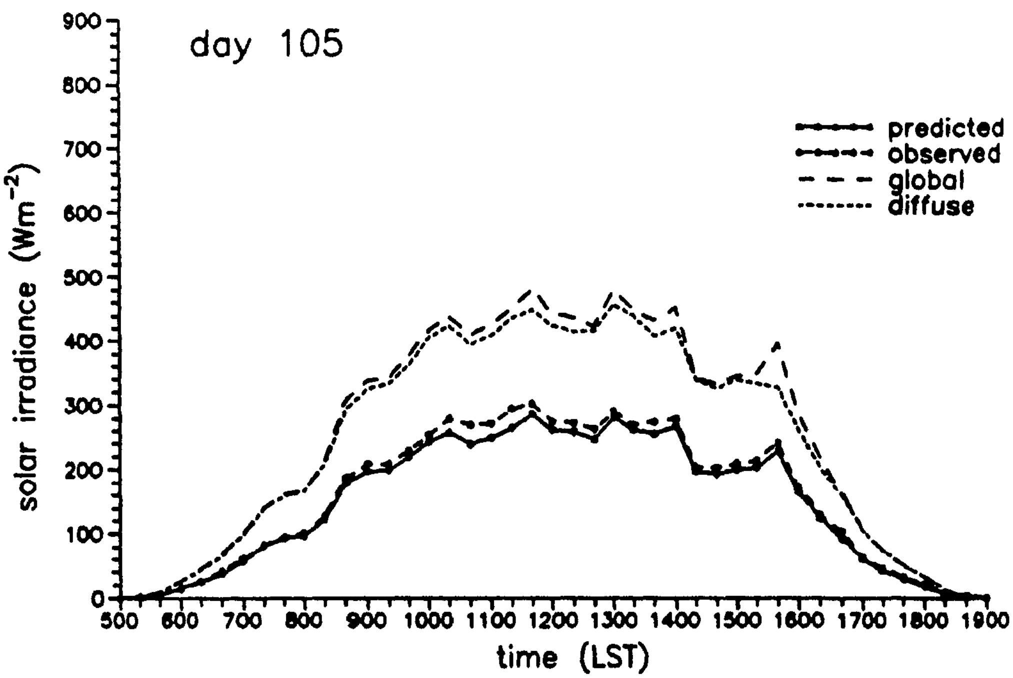
day 105
predicted
observed
global
diffuse
solar irradiance (Wm^-2)
time (LST)
0
100
200
300
400
500
600
700
800
900
500 600 700 800 900 1000 1100 1200 1300 1400 1500 1600 1700 1800 1900

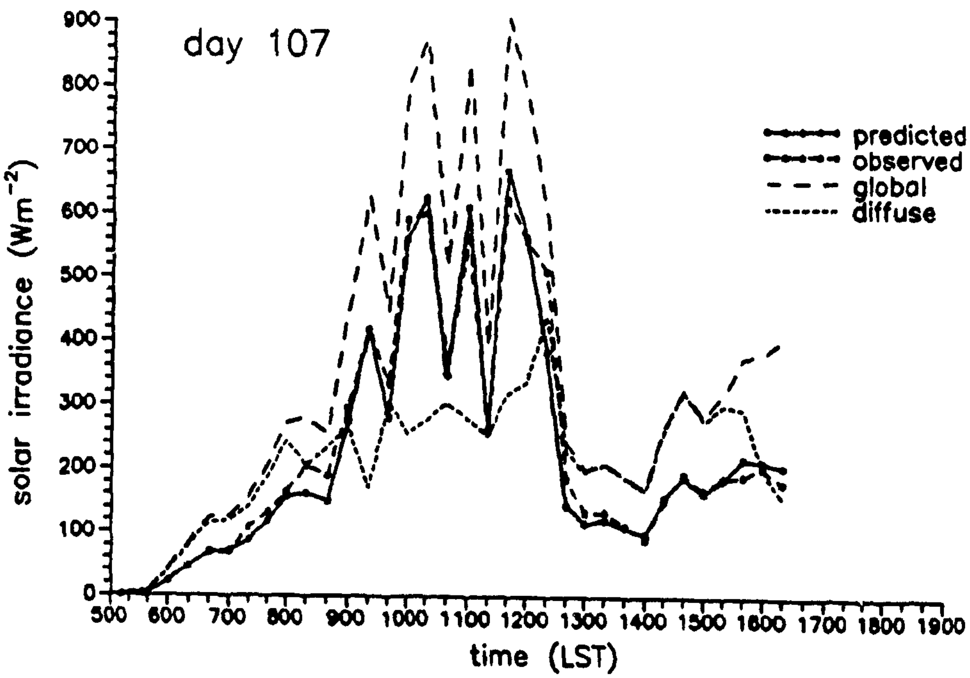
day 107
solar irradiance (Wm^{-2})
time (LST)
predicted
observed
global
diffuse
0
100
200
300
400
500
600
700
800
900
500
600
700
800
900
1000
1100
1200
1300
1400
1500
1600
1700
1800
1900

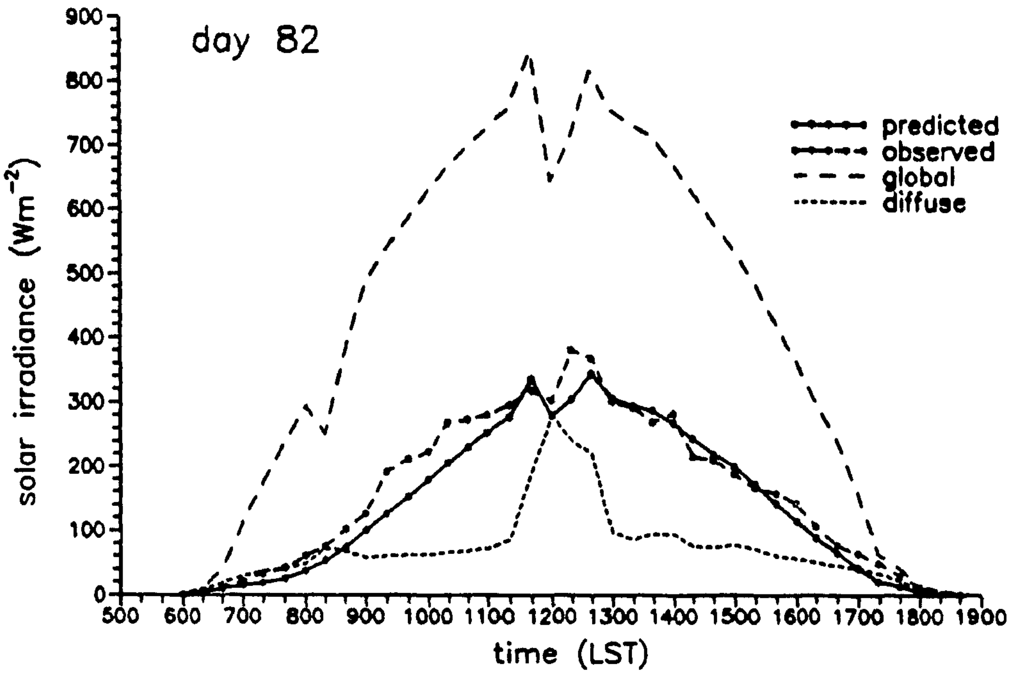

day 82
predicted
observed
global
diffuse
solar irradiance (Wm^{-2})
time (LST)
0
100
200
300
400
500
600
700
800
900
500
600
700
800
900
1000
1100
1200
1300
1400
1500
1600
1700
1800
1900

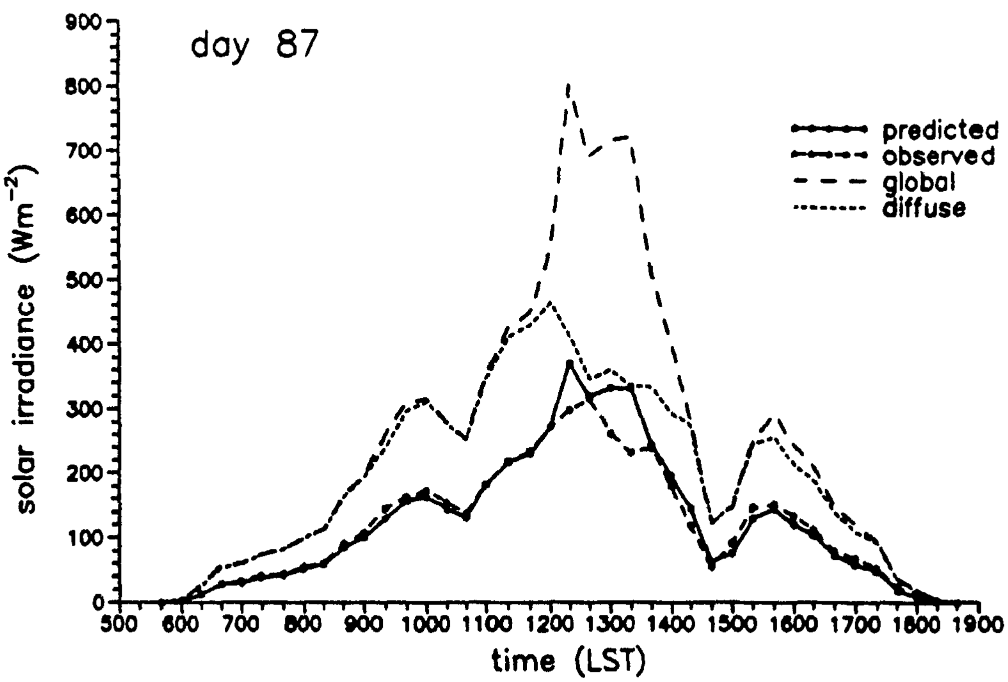

day 87
predicted
observed
global
diffuse
solar irradiance (Wm^{-2})
time (LST)
0
100
200
300
400
500
600
700
800
900
500
600
700
800
900
1000
1100
1200
1300
1400
1500
1600
1700
1800
1900

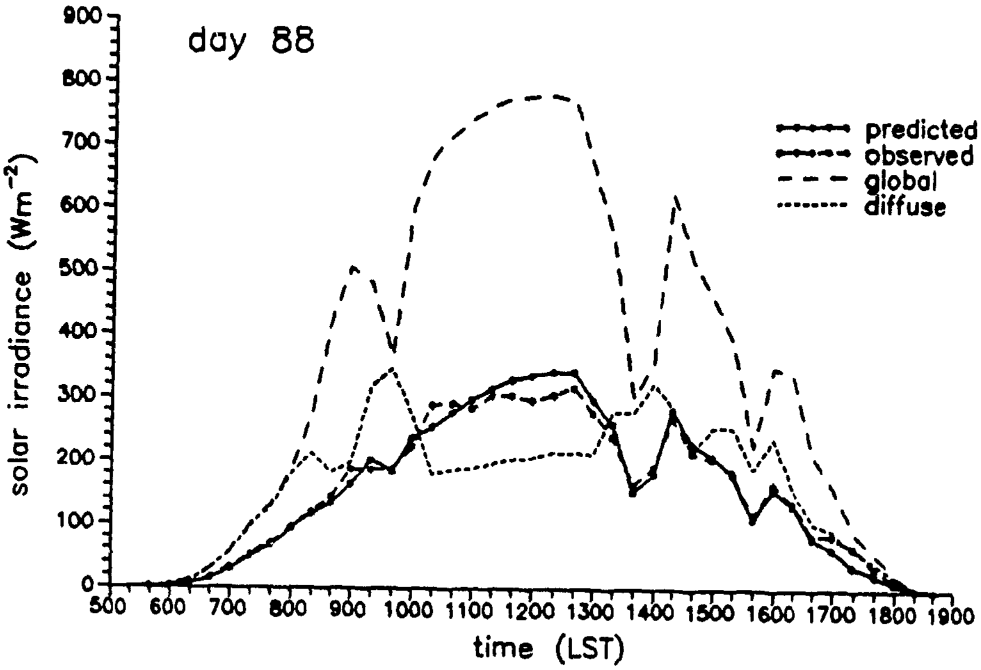
day 88
predicted
observed
global
diffuse
solar irradiance (Wm^{-2})
time (LST)
0
100
200
300
400
500
600
700
800
900
500 600 700 800 900 1000 1100 1200 1300 1400 1500 1600 1700 1800 1900

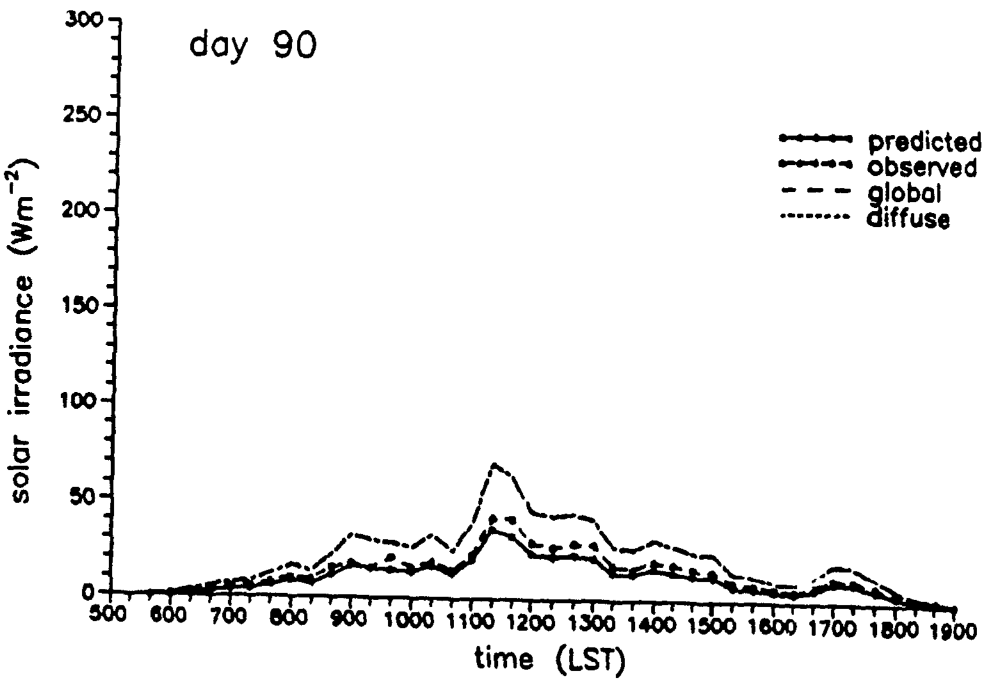
day 90
predicted
observed
global
diffuse
solar irradiance (Wm^{-2})
time (LST)
0
50
100
150
200
250
300
500 600 700 800 900 1000 1100 1200 1300 1400 1500 1600 1700 1800 1900

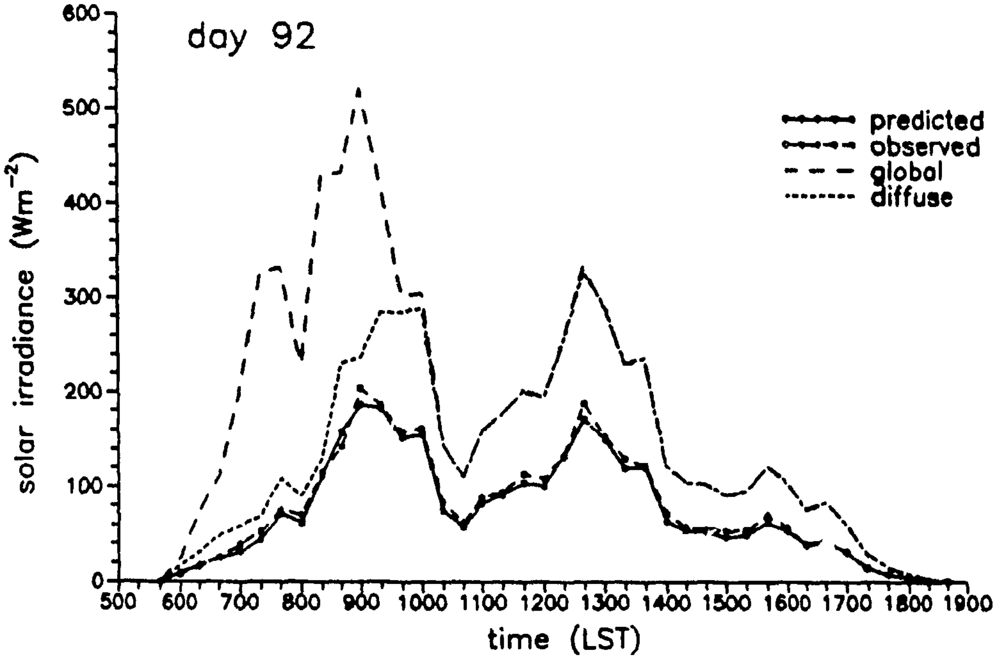
day 92
predicted
observed
global
diffuse
solar irradiance (Wm^{-2})
time (LST)
0
100
200
300
400
500
600
500
600
700
800
900
1000
1100
1200
1300
1400
1500
1600
1700
1800
1900

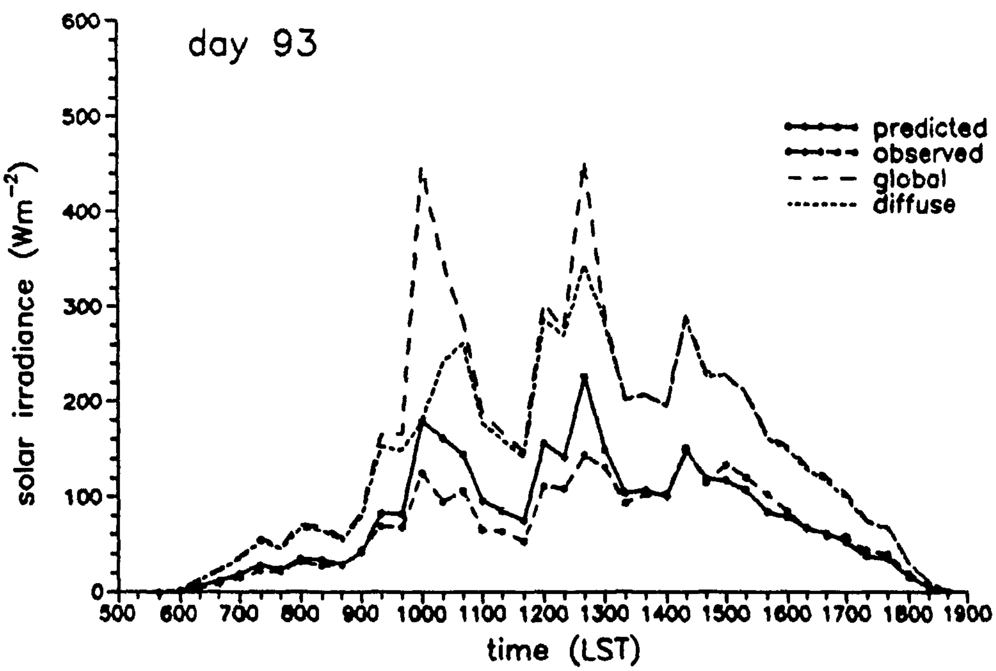
day 93
predicted
observed
global
diffuse
solar irradiance (Wm^{-2})
time (LST)
0
100
200
300
400
500
600
500
600
700
800
900
1000
1100
1200
1300
1400
1500
1600
1700
1800
1900

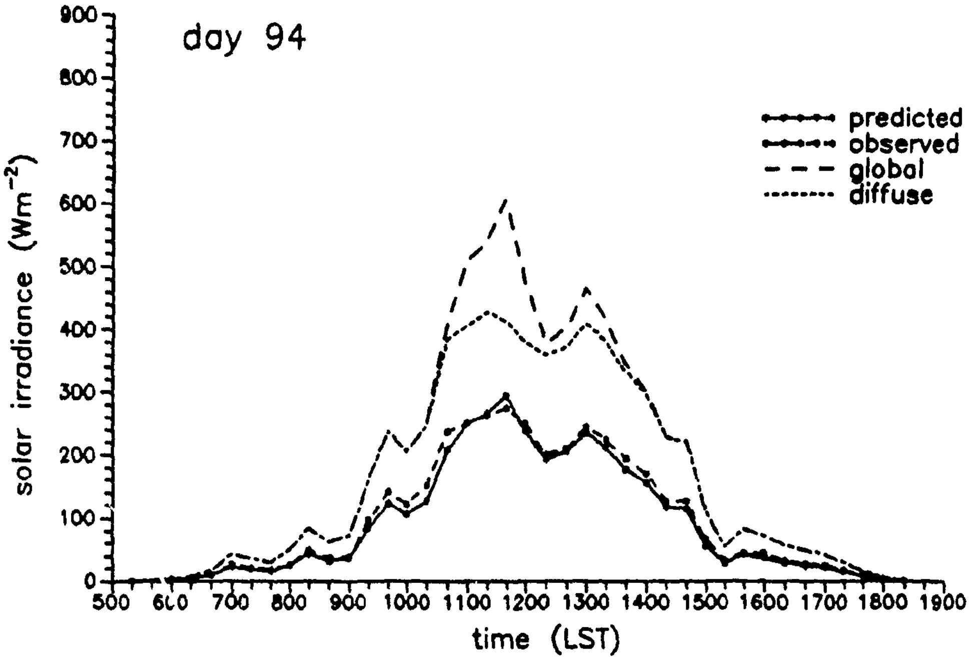
day 94
predicted
observed
global
diffuse
solar irradiance (Wm^{-2})
time (LST)

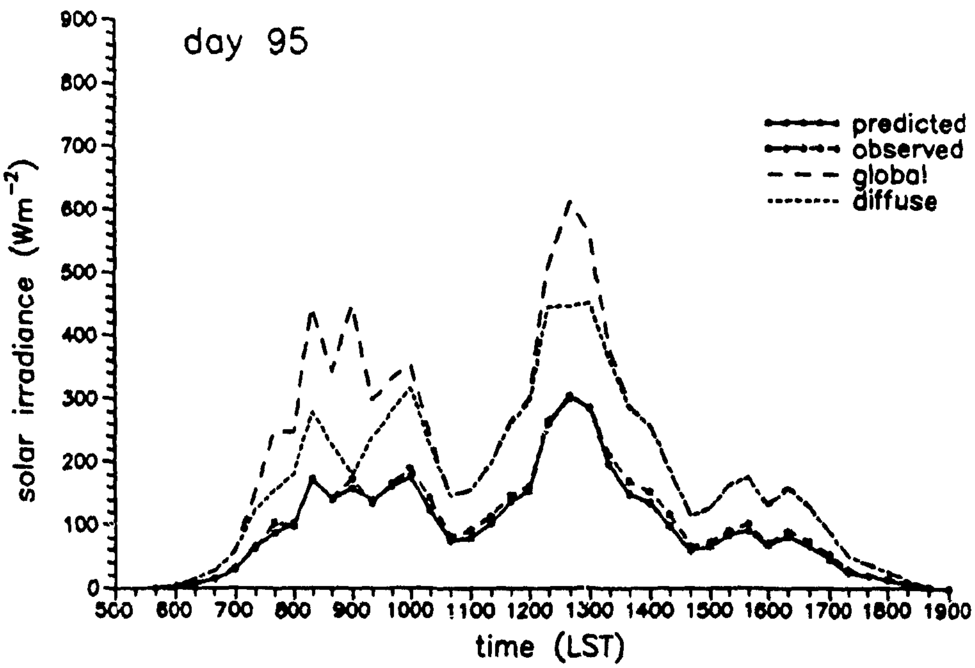
day 95
predicted
observed
global
diffuse
solar irradiance (Wm^{-2})
time (LST)

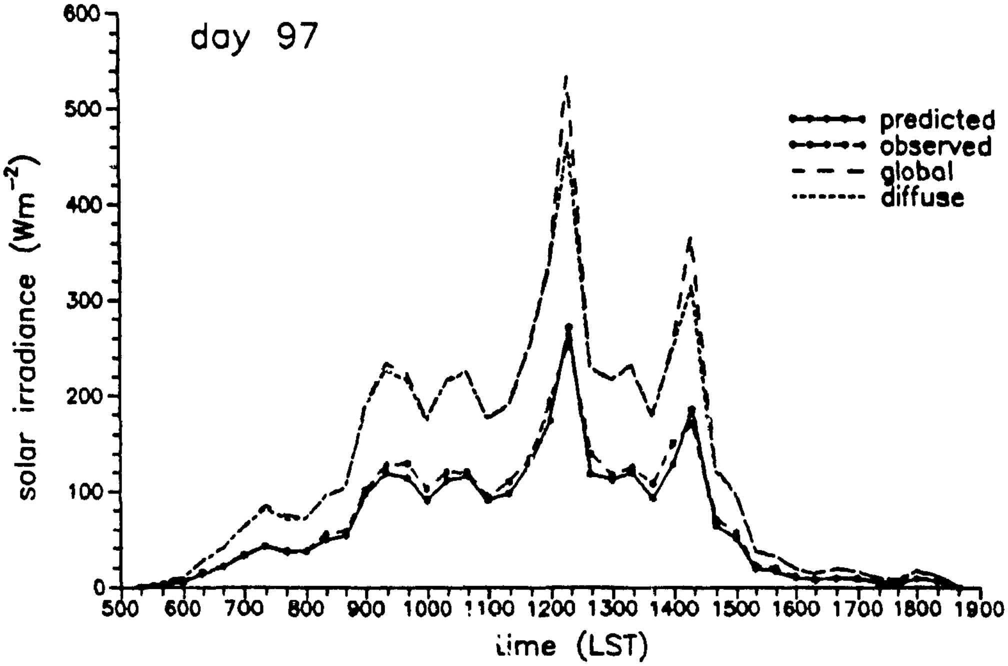
day 97
predicted
observed
global
diffuse
solar irradiance (Wm^{-2})
time (LST)
0
100
200
300
400
500
600
500 600 700 800 900 1000 1100 1200 1300 1400 1500 1600 1700 1800 1900

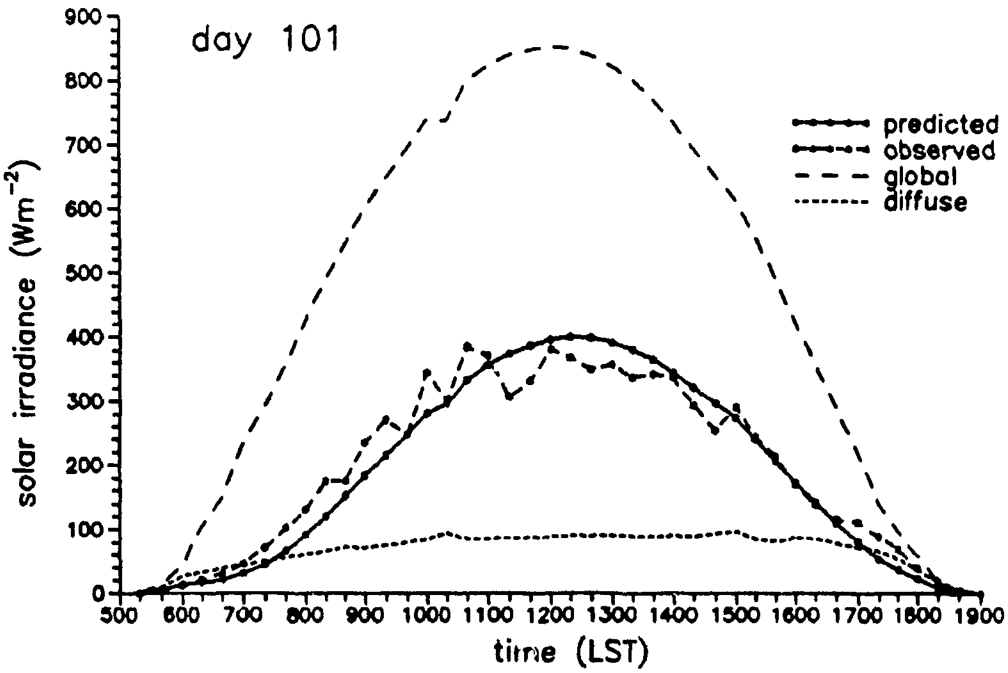
day 101
predicted
observed
global
diffuse
solar irradiance (Wm^{-2})
time (LST)
0
100
200
300
400
500
600
700
800
900
500 600 700 800 900 1000 1100 1200 1300 1400 1500 1600 1700 1800 1900